THE UNIVERSITY OF CHICAGO

MULTISCALE TRAJECTORY ANALYSIS AND SNAPSHOT 3D MICROSCOPY STUDIES ELUCIDATE FUNCTIONAL CONSEQUENCES OF HETEROGENEOUS INSULIN GRANULE TRAFFICKING

A DISSERTATION SUBMITTED TO
THE FACULTY OF THE DIVISION OF THE PHYSICAL SCIENCES
IN CANDIDACY FOR THE DEGREE OF
DOCTOR OF PHILOSOPHY

DEPARTMENT OF CHEMISTRY

BY
HANNAH SUEJUNG YI

CHICAGO, ILLINOIS
DECEMBER 2022

To my friends and family

“I call our world Flatland, not because we call it so,

but to make its nature clearer to you, my happy readers,

who are privileged to live in Space.” – A Square

EDWIN A. ABBOTT, *Flatland: A Romance of Many Dimensions*

TABLE OF CONTENTS

LIST OF FIGURES

LIST OF TABLES

ACKNOWLEDGMENTS

Recently, someone asked me what I'll regret from Chicago. The obvious answer was graduate school. He really meant to ask what I would miss from Chicago, but my answer would not change. The pursuit of my degree has been, at times, arduous. Yet these challenges have been met with the most supportive people. Your care was critical in this process. Without it, I would be lost.

Chris (almost PhD) has been a constant fixture throughout graduate school. I am appreciative of your support at the low times and critique at the careless times. You made sure to instill reason into going to lab when all I wanted to do was go to the Point. Our countless hours relaxing at the Point, biking on the Lake Shore Trail, and napping on the Quad were perfect. Even the late nights in lab were enjoyable when you were down the hall with a promise to stop by Jimmy's on the way home.

The era of COVID-19 was (and still is at the moment of writing this) a global challenge, but the close roommates/friends with whom I sheltered made my world. Lawson, Greta, Tim, and Margaret are equal parts intellectuals and dingbats. Never have I learned so much yet so little after a night of cocktails and conversation at East View Park. I hope our ties will be lifelong. Sorry in advance when I forget to text you back.

I am deeply grateful to my research advisor Professor Norbert Scherer for taking me into the lab which has been my second home for the past 6 years. I was under prepared, yet the quality of mentorship and guidance was instrumental in my growth. The Scherer lab was a motley bunch of the most hard working, thoughtful, and collaborative researchers. My only regret is that I did not aptly pay back the innumerable hours of teaching and training I enjoyed from older researchers– especially from Xiaolei, Matt, and Yuval.

To my other thesis committee members: Thank you Professor Aaron Dinner for the starting image analysis subgroup where I learned a lot from you and the members of the peanut gallery (Steven, Chatipat, Elizabeth, Yuval, Shiqi). Also, thanks Aaron for indefinitely postponing image analysis subgroup after the purpose was lost. Professor Bozhi Tian was a source of support in

the later half of my degree. His enthusiasm and wisdom was instrumental to the pursuit of new collaborative research avenues. I sincerely hope that some of those ideas come into fruition.

I would not be here today without the support of my parents and the rest of my family. My parents, Simon and Tina, showed me how to be diligent and independent growing up. They also know how to have a good time, a valuable skill in graduate school. My brother Justin gave me unconditional support and never made re-explain the Chemistry PhD experience. Thank you to Joann, and her husband and kids, for always being in my life. Your impact cannot be understated. To hold the first PhD in the family is an honor. I have felt the support from my parents, brother, aunts, uncles, and all of my cousins throughout. I've learned so much about kindness, happiness, patience, and strength from you all. Thank you Mom, Dad, and the rest of the family.

CHAPTER 1

INTRODUCTION

The pursuit of today's important issues in Physical and Biophysical Sciences is increasingly complex and interdisciplinary. A modern chemist can specialize in scientific skills ranging from chemical synthesis to biophysical analysis to theory. The common denominator is the desire to understand function at the smallest, most fundamental level. Herein, I present my thesis work on the dynamics of insulin transport in β-cells using a blend of experimental and data analysis techniques with a broad view toward a mojor human health issue– Type 2 diabetes mellitus. The development of new biochemical and optical technologies has rapidly enhanced the field of biophysical dynamics to achieve remarkably rich data. The combination of these technologies, with new statistical models, enables insightful inquiry into understanding *in vivo* insulin transport and its functional relationship to diabetes-related defects.

1.1 Background

1.1.1 Diabetes Mellitus

Diabetes mellitus, commonly known as diabetes, is a group of diseases affecting the body's proper regulation of blood sugar (glucose). The debilitating disease affects one's muscles and often cascades into related complications in high blood pressure and morbidity. Type 2 Diabetes accounts for more than 90% of diabetes mellitus cases; in the United States alone, there are an estimated 30 million people affected (nearly 10% of the U.S. population). The estimated total costs of diagnosed diabetes is $327 billion in the latest assessment in 2017; a 26% increase compared to the $245 billion evaluation in 2012 [1]. Despite being the most prevalent disease affecting the U.S. socially and economically, research on cures remains elusive.

The family of diabetes diseases is traditionally classified into three categories [2, 3]. Type 1 diabetes is a polygenic autoimmune disease in which the body is unable to synthesize insulin.

Type 2 diabetes is a polygenic non-autoimmune disease with complex defects in insulin action and insulin secretion that lead to metabolic derangement. The third classification encompasses the remainder of uncommon forms of diabetes, including monogenic (MODY-type), gestational, and secondary diabetes. The complexity of a diabetes pathogenesis is attributed to the several genetic defects (polygenic character) and varied environmental factors. Thus, the mechanisms leading to diabetes are complex and vary from patient to patient.

Type 2 Diabetes (T2D) is manifest as the interplay of three core defects: (1) defective insulin secretion from pancreatic β-cells; (2) impaired insulin-stimulated glucose production from the liver; and (3) resistance to glucose uptake in skeletal and fatty tissues [4]. Leading historic theories viewed diabetes as a disease primarily concerning insulin resistance [5–7]. Continued genome-wide investigations (GWAS) have identified genes associated with increased risk for T2D [4, 8]. Populations at risk for T2D display inherited abnormalities mostly for impaired insulin secretion, a precursor for β-cell dysfunction [9–12]. By contrast, genetic defects tied to impaired insulin action, and thereby insulin resistance, is less common and tied to mechanisms related to obesity [9, 11]. Environmental and lifestyle factors, namely those leading to obesity, compound on the β-cell dysfunction and insulin resistance, reducing insulin sensitivity in peripheral tissue [13]. The superior prevalence of β-cell related genes that increase the risk for T2D is believed to show that β-cell dysfunction supersedes insulin resistance and impaired insulin action in the pathogenesis of onset diabetes.

1.1.2 The Insulin Transport Problem

β-cells in the islets of Langerhans of the pancreas store, regulate and secrete insulin. Insulin is a highly potent hormone for managing blood glucose levels by facilitating cellular glucose uptake. It also regulates carbohydrate, lipid and protein metabolism [14]. Increased glucose levels in the bloodstream induce bi-phasic secretion: a short ($\sim$10 min) "first-phase" of insulin secretion from β-cells then is followed by a sustained "second-phase" secretion wave (Fig 1.1. In T2D, the first-

phase is nearly abolished and the second-phase is strongly reduced [15]. Insulin is secreted into the bloodstream where it acts on insulin-dependant tissue, principally adipose and muscle tissue, to uptake glucose by the insulin sensitive GLUT4 protein [16]. The inability to properly secrete insulin from β-cells is termed β-cell dysfunction, while the inability to properly induce peripheral tissue uptake is that of impaired insulin action.

The required working precision for β-cell function is vastly higher than that of the insulin dependant tissue. An estimated 10% of insulin stored in β-cells are secreted for each glucose stimulation in the body (i.e. eating a meal) and *in vivo* [18, 19]. This fraction of insulin is responsible for signalling the entire body's muscular and adipose tissue glucose uptake. Thus, relatively small changes in the secretion rate in β-cells can lead to comparatively large changes in insulin detection by tissue. As an example, a change from 10% to 5% insulin secretion from poorly secreting β-cells will lead to a 50% reduction in insulin sensed by the tissue. Furthermore, errors in β-cell function can be compounded by insulin resistance in insulin dependant tissue exacerbate the disease.

Several factors related to defective insulin secretion are contribute to β-cell dysfunction. These include: (i) poor formation or maturation of insulin-containing vesicles; (ii) defective metabolic signalling in the glucose stimulated insulin secretion pathway; and (iii) defective protein machinery related to insulin vesicle fusion to the plasma membrane and secretion out of the β-cell. Overall, β-cell dysfunction can manifest as the inability for intracellular insulin to reach the plasma membrane for secretion.

Intracellular insulin has long been thought of as two pools of insulin-containing vesicles (termed insulin granules) corresponding to the biphasic nature of insulin secretion. These pools are loosely defined in terms of their physical location, but much evidence has been found on functional differences in subsets of insulin-containing vesicles (Fig 1.1b) [20–24]. A small subset ($\sim$ 1-5%) of secretory granules known as the readily releasable pool (RRP) are "pre-docked" at the cellular membrane and contribute to the rapid first phase of insulin secretion [18, 20]. The rest of the granules compose the reserve pool (RP). RP granules are used to replenish the readily releasable pool.

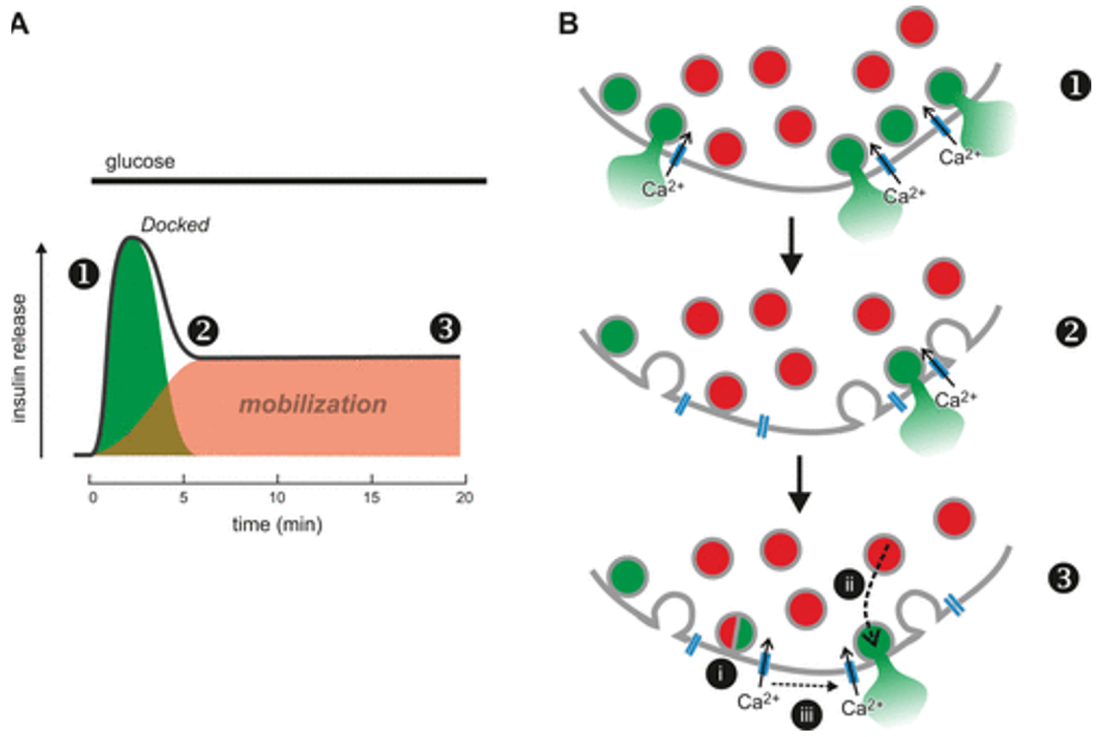

Figure 1.1: **Intracellular insulin granule functional pools leading to biphasic insulin secretion.** (a) Observed biphasic insulin release resulting from glucose stimulation. The rapid first phase is comprised of docked granules (green). The sustained second phase is from granules that are mobilized to the cell periphery (red). (b) The proposed intracellular pools are the readily releasable pool (RRP, green) and the reserve pool (RP, red). (1) Calcium influx triggers the insulin release from RRP granules. (2) The secretion of RRP granules is concerted and the insulin release rate falls after the RRP granules are all secreted and the docking sites are open. (3) RP granules are mobilized to the cell periphery dock sites and contribute to a sustained and steady release of insulin. Adapted from [17]

.

A fraction of the reserve pool is secreted upon glucose stimulation contributing to the sustained, yet slower second phase of insulin secretion [24].

Continuing research has challenged the two functional pool picture which fails to capture the heterogeneity in regulation by and sensitivity to chemical and metabolic stimuli [25–28]. Intracellular calcium, in particular, plays a multifacted role in directing subsets of granules to move faster or recruit granules to the RRP [28, 29]. Still, the mechanism for the recruitment and transport of insulin granules between the two (or more) pools remains unknown.

1.2 Molecular Mechanisms in Insulin Granule Transport

Movement is inherently three-dimensional in biological systems. Dynamic processes from animal migration to intracellular vesicle trafficking exhibit responsive movement to environmental stimuli. These moving targets, whether organelles or organisms, interact with their environment to introduce further modulation to the apparent transport dynamics. For intracellular insulin trafficking, a tightly regulated process necessary to maintain blood glucose levels, the primary manifold is the microtubule network, the moving targets are insulin granules, and the actin network provides nuanced modulations to the microtubule network. Kinesin motors transport insulin granules on the microtubule network, a complex three-dimensional manifold within the β-cells. The dense intracellular environment and multiple motor interactions further complicate the transport of insulin granules. Ultimately, insulin granules formed in the Golgi Apparatus are recruited to the cell surface in order to be secreted upon glucose stimulation (Fig 1.2).

1.2.1 Motor-Cargo Mechanism for Vesicle Trafficking

Insulin granules are densely packed, Golgi-derived vesicles that use the ubiquitous "motor-cargo" mechanism for transport in pancreatic β-cells. Motor proteins, specifically kinesins for insulin transport, associate to the lipid surface of the granule and carry the granules on the complex, microtubule network. Fusion-competent granules are docked to the plasma membrane and become

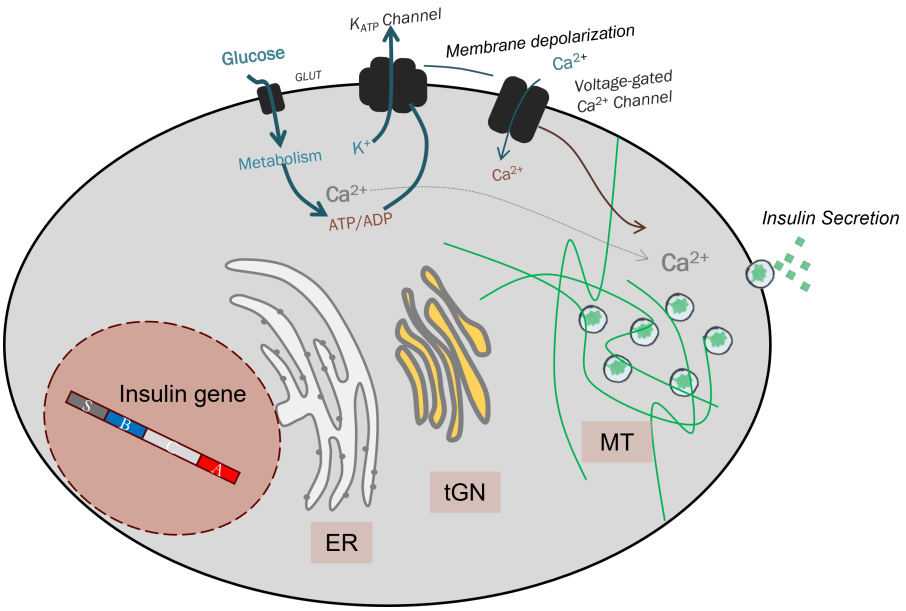

Figure 1.2: **Schematic of a β-cell and the glucose-stimulated insulin secretion signal pathway.** Insulin is a small protein encoded by the insulin gene in β-cells and folded into the small protein in the Endoplasmic Reticulum (ER). Insulin is packaged into dense core vesicles, termed granules, in the trans Golgi Network (tGN). There vesicles are transport on the microtubule (MT) network for eventual glucose stimulated insulin secretion (key proteins in the pathway are shown in black).

primed for secretion upon glucose stimulation.

The role of motor proteins is critical to manifest the glucose-dependent response required for β-cell function. The recruitment of granules to the cell surface is essential for sustained insulin secretion in response to glucose. Motor proteins hydrolyze adenosine triphosphate (ATP) to generate the requisite energy to move the cargo load along a cytoskeletal filament [30]. β-cells sensing a high glucose concentration in the bloodstream will uptake and metabolise the glucose to produce cytosolic ATP, enhancing motor protein activity. Insulin vesicle movement is affected by the glucose-induced increase in cytosolic ATP [31]. Overall, high glucose stimulation in β-cells leads to enhanced motor protein activity that can increase the rate at which insulin granules are recruited to the cell surface.

An emerging paradigm for motor protein-driven transport involves multiple molecular motor proteins associated to each single granule. The resulting granule movement is dependent on the

competing pulls from each individual motor protein's influence. Cargo transport is confined or stalled when the motors associate with different microtubule filaments [32], opposite polarity motors associate with the same microtubule filament [33], or motors display a concerted cycling motion around microtubule junctions [34]. Kinsein-dependant microtubule transport is the dominant mechanism for long-range transport in insulin trafficking [25, 35], so cycling and multi-filament tug-of-war must be considered for this system. Therefore, insulin granule transport is highly dependant on the structure and dynamics of the cytoskeletal filaments.

1.2.2 Microtubule Dynamics

Microtubules (MTs) are fundamental for vital cellular processes such as cell division, structural integrity, and intracellular transport. Monomeric α and β tubulin subunits polymerize into long, stiff microtubule filaments. MTs are dynamic polymers that modulate in length and shape. Tubulin subunits can polymerize to grow the length of a MT or depolymerize to shrink the overall length. Modulations in the shape or degree of bending of these long polymers arise from mechanical and thermal influences– such as the kicking force from motor proteins pulling vesicle loads along the filament, the thermal environment that induces random thermal fluctuations, and pushing or pulling from nearby organelles (e.g. actin network) in the crowded intracellular environment. Further influences from post-translational modifications by microtubule-associated proteins (MAPs) selectively modify MTs and regulate their stiffness and polymerization rate. These factors strongly modulate the microtubule network into a constantly fluctuating and reorganizing scaffold.

The microtubule network contributes to the long-range dynamics of insulin granule transport. The dynamic microtubule network are the primary tracks for intracellular trafficking because kinesin is the dominant motor protein in motor associated to insulin granules [25, 35]. The overall direction of the tracks are determined by the shape and bending of the MT filaments. The relatively large cross sections of MT filaments make them stiff, with a persistence length of 4-8 mm in isolated *in vitro* systems, compared to other cytoskeletal filaments [36]. Despite this, native *in vivo*

intracellular microtubules have a much shorter persistence length ($\sim 20\mu m$) [37, 38], exhibit significant bending [39, 40], and are capable of bearing large compressive loads [41, 42]. The highly bent shape of MTs is also dynamic and short-wavelength buckling fluctuations form in response to actomyosin contractility [42].

The microtubule-associated protein tau regulates the structure and dynamics of the microtubule network in β-cells during glucose stimulated insulin secretion. Tau, a small regulatory protein, binds to the interface between tubulin monomers to stabilize the filament structure from depolymerizing and consequentially promote filament growth [43–45]. Binding and stabilization of tau on microtubule filaments also ridgidifies the filament structure– nearly a 4 fold increase in the flexural rigidity parameter *in vivo* after tau binding [46]. Phosphorylation of tau decreases it's binding affinity to tubulin [47]. Real time imaging in mouse β-cells support a model where high glucose concentration enhances microtubules disassembly near the cell periphery via tau phosphorylation [48]. However, other studies of microtubule networks in β-cells suggest that the high glucose environment increases the overall network density and increases the microtubule nucleation from the Golgi to promote the number of tracks available for insulin granules to reach the cell periphery [49, 50]. In summary, a high glucose environment in β-cells decreases ridgidity of MT filaments by tau phosphorylation, increases the MT growth near the center of the cell, yet reduces the MT density near the surface of the cell.

1.2.3 Actin Dynamics

Actin is a highly dynamic network with adaptive reorganization properties that make it critical for functions such as cell motility, maintenance of cell structure, and contractile motions in tissue. Globular actin (g-actin) subunits polymerize to linear filamentous actin (f-actin) that localizes at the periphery of the cell, and is commonly referred to as the cortex [51]. The cross-sectional area of an f-actin filament is nearly 10 times smaller than that of a microtubule filament; f-actin is also nearly 100 times less resistant to bending [36]. Myosin, actin's companion motor protein, has a

comparable stall force from its ATP-driven motion, and is able to highly influence the structure and dynamics of the floppy actin network. Passive thermal contributions to actin motion and active pulling by myosin motors influence the fluctuating dyanmics in the network [52]. Furthermore, the actomysoin network is highly sensitive to local metabolic changes and is a critical regulator of secretion based on its selective localization at the cell cortex.

Short-range dynamics in motor-driven transport is influenced by fluctuations in the actomyosin network [52]. Insulin granules are larger than the typical pore size of the cortical actin network causing it to act as a viscoelastic fluid rather than a porous material [7, 52, 53]. The actomyosin network acts as an *active mesh material* that drives fluctuations by pushing the insulin granule. Short-range modulation also occurs indirectly by increasing fluctuation dynamics in the microtubules embedded in the finer actin network [42]. Furthermore, tau protein acts as a direct crosslinker between the two cytoskeletal networks [54].

The cortical location of f-actin uniquely positions it as a secretion regulator near the outer membrane of the β-cell. Actin cortex disassembly during glucose stimulated insulin secretion is a well-established process that reduces the gel-like actin network from hindering granule docking to secretion sites [55–57]. More exactly, glucose stimulation increases the phosphorylation of focal adhesion related proteins FAK and paxillin, thereby remodelling and reducing the density of actin at the cortex [58, 59]. This density reduction also reduces the stabilization and density of microtubules near the cortex since the high glucose conditions negatively regulate tau [50].

1.3 Biophysical Analysis of Live-Cell Vesicle Trafficking Dynamics

Data-driven biophysical research is uniquely suited to provide insight into vesicle trafficking. First, advances in biotechnology have vastly enhanced fluorescent labeling in the specificity of labeling, the variety of physio-chemically sensitive probes, and the overall photophysical properties (brightness, stability, etc.) [60]. Fluorescent microscopy methods for studying biological samples with high specificity are able to achieve rapid imaging rates without compromising the field of view,

achieve super-resolution images, and achieve volumetric imaging at camera-limited frame rates [60]. The snapshot volumetric modality, in particular, is suited for 3D tracking of insulin granules [61]. Quantitative image analysis is widely used to study the structure and dynamics of data sets obtained from microscopy. Single particle tracking provides spatio-temporal information of individual granules to resolve heterogeneous dynamics in an ensemble. Lastly, statistical order parameters can describe the stochastic dynamics of monitored granules and even find patterns in seemingly unordered data.

1.3.1 Fluorescent Labeling of Mammalian Cells

Fluorescent protein fusion constructs continue to be the standard for specific labeling of intracellular targets [62]. Detecting only fluorescent probe emission allows for high specificity to only image the target of interest. There are two common approaches to covalently label a target protein inside a cell for fluorescent imaging. The most common and conventional method is the use of intrinsically fluorescent proteins, such as the jellyfish-derived Green Fluorescent Protein (GFP) or those related in structure to GFP [62]. Superior photophysical properties can be achieved by using small cell-permeable fluorescent molecule ligands. In this case, ligands covalently attach to self-labeling enzymes– commonly Halo tags [62, 63], SNAP tags [64], and CLIP tags [65]– that fuse in-frame to the cellular protein target of interest. The size of the genetically fused genes are comparable, around 30-kDa for fluorescent proteins and the self-labeling enzymes, yet the later labeling approach allows incorporating a larger range of small organic dyes [66]. Still, fluorescent protein fusion remains the most common approach.

Fluorescent protein studies to characterize the localization and dynamics are often performed using over-expressed systems using transient transfection. Plasmid-based constructs containing the fluorescent protein and the protein of interest are easily created and introduced into the nucleus of the cell. The fluorescent protein fused with the protein of interest, in this case insulin, is expressed on top of the existing, endogenous protein production. The ease of the experimental workflow has

led to a dependence on such ”over-expressed” systems. However, these systems might not recapitulate endogenous expression and can lead to protein misfolding, false localization, and nonspecific interactions.

Endogenous labelling by homologous recombination with exogenous DNA has been successfully performed for decades by lentiviral transfection with modest success [67], but advances in genome editing have flourished in recent times. Gene editing technologies invented in the 2000s include zinc finger nucleases (ZFNs), transcription activator-like effector nucleases (TALENs), and clustered regularly interspaced short palindromic repeats (CRISPR)/Cas9 [68]. In particular, CRISPR/Cas9 enables efficient, site-specific engineering of genetic mutations in a variety of cell types ranging from prokaryotic to eukaryotic cells [69–71]. The technology used in this thesis for endogenous labeling is CRISPR/Cas9 (Fig 1.3), which leverages a bacterial antiviral immune system mechanism (CRISPRs) to generate a site-specific double-stranded DNA break for the eventual insertion or deletion of genetic material in the genome [72, 73].

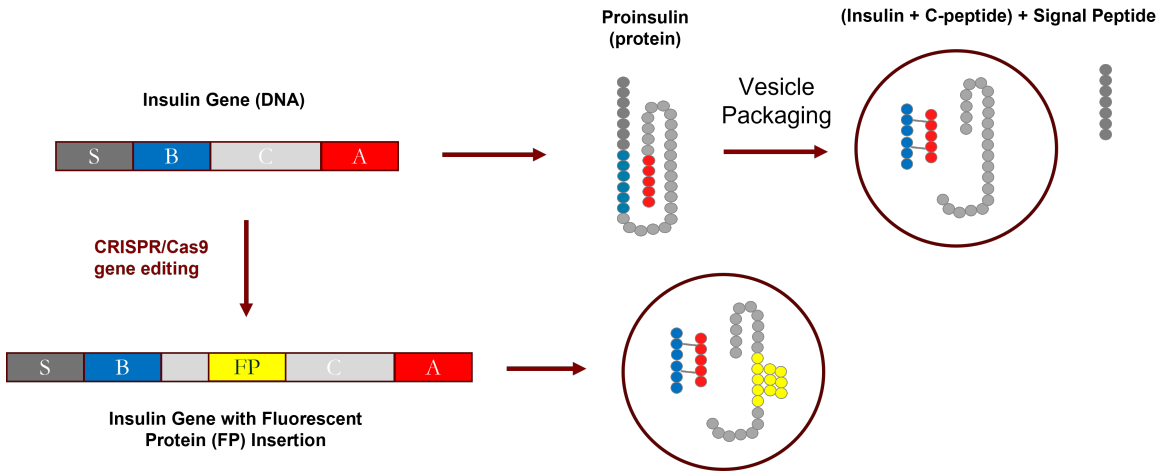

Figure 1.3: **Schematic of the fluorescent protein labeling approach by CRISPR/Cas9.** The fluorescent protein gene is inserted in-frame to the C-peptide gene of insulin for a model cell line. The C-peptide and insulin protein are colocalized in insulin granules allowing for an indirect labelling approach for intracellular insulin in β-cells.

1.3.2 Live-cell Fluorescent Microscopy

The development of the confocal microscope was motivated by the goal of imaging tissues [74]. The optical sectioning capability by way of a small pinhole enables elimination of out-of-focus background light in dense samples at the expense of some detected fluorescence signal [60]. Bright, stable fluorophores are critical for studying cellular dynamics at the 100-200s time-scale. Fast scanning for high frame rate imaging is realized in spinning disk confocal microscopy through the use of a multi-pinhole disk (i.e., a Nipkow scanner) that allows for multiplex laser excitation and emission collection [75, 76]. The spinning disk geometry allows achieving higher frame rates (100+ Hz) suitable for cellular dynamics while maintaining comparable resolution to a conventional single confocal aperture light scanning microscope.

Expanding the dimensionality of digital video microscopy in the axial (or z-axis) direction to achieve volumetric measurements would enable studying transport in 3D vs. the 2D sectioning inherent to confocal microscopy. One challenge in live cell imaging in three dimensions is to sample the volumetric field of view before cellular dynamics changes the system. This is especially pertinent in vesicle trafficking of many particles. A high frame rate will shorten the expected step size of moving targets in subsequent frames and lend to more accurate linking results; see subsection 1.3.3.

Multifocal microscopy is one approach to volumetric imaging without sacrificing scanning time [77]. Conventional 3D scanning approaches to achieve volumetric microscopy require more time for sampling compared to their 2D counterparts. The sampling time for imaging a 3D volume depends on the 2D sampling time and the axial scan rate to create a ”stack” of 2D sections. The series od 2D slices (images) obtained by translating the sample stage or the objective and are combined to create a 3D image [78]. In contrast, snapshot 3D sampling methods bypass the serial axial scanning to achieve volumetric imaging at frame rates limited by the camera speed and the signal integration required to obtain a desired SNR [61, 77, 79, 80].

1.3.3 Single and Multiple Particle Tracking

Particle tracking has yielded many insights into both transport within and material properties of complex fluids [81–83]. The measured dynamics of several hundred (or more) particles provides important information to understand the interactions of the probe particle with complex or intracellular environments. Because of the heterogeneous and stochastic influence of the cytoskeletal-dominated intracellular environment on vesicle trafficking, large sample sizes and long trajectories are critical to resolve complex dynamics. Single-particle measurements allow the study of heterogeneous processes or minor constituent subpopulations that would otherwise be masked in ensemble dynamic measurements.

Localization of particle positions are estimated from distributions of pixel intensities in fluorescence images and linked from one frame to another of a video microscopy movie to form time trajectories of their motion. In general, particle localizations are determined by a statistical analysis of the highest intensity pixels in an image by centroid determination or Gaussian fitting, and the position is refined by higher order symmetry parameters [82, 84]. Linking of N number of particles in subsequent time frames (τ) is determined as the largest likely distance traveled (δ_i) based on the Brownian diffusion model [82]:

$$P(\{\delta_i\}|\tau) = \left(\frac{1}{4\pi D\tau}\right)^N exp\left(-\sum_{i=1}^{N}\frac{\delta_i^2}{4D\tau}\right). \tag{1.1}$$

This linking algorithm minimizes $\sum_{i=1}^{N}\delta_i^2$ and favors shorter times between frames so that the nearest neighbor in adjacent frames is the same particle.

While numerous automated tracking algorithms exist [82, 84, 85], in practice they must be tuned for each experimental condition and the results must be manually reviewed and filtered. This introduces subjective bias and statistical uncertainty to the results. Advances in artificial intelligence for image analysis has grown rapidly to create quantitative image analysis methods that are completely independent from human curation [86–88].

1.3.4 Transport Statistics

The diffusive motion of organelles and other macromolecular structures in cells is anomalous [89]. The intracellular environment is densely packed and heterogeneous, filled with organelle structures and macro-molecular networks, such as cortical actin impart spatially selective influence on transport. The conditions for conventional Brownian diffusion, dilute solution and isotropic noise, are not met in the cell [90]. The anomalous character of insulin granule transport reflects influences of active and confined environments that also make transport highly heterogeneous.

The most widely used quantity to quantify trasnport is the mean squared displacement (MSD) [91]. MSD analysis uses a varying, lag time or Δ, to evaluate the displacement $\delta(\Delta)$. This analysis is averaged through the entire particle position trajectory, r(t) of length T; in the case of the time averaged MSD,

$$MSD(\Delta) = \overline{\delta(\Delta)^2} = \frac{1}{T-\Delta}\int_0^{T-\Delta}[r(t+\Delta) - r(t)]^2 dt. \tag{1.2}$$

The "sliding average" samples the entire trajectory and reports the average displacement for each specific time lag. In cases where an ensemble of N trajectories are measured, the ensemble average MSD,$\mathbf{R}$(t), can be estimated from the time averaged MSD [92]:

$$\langle \mathbf{R}(t)^2 \rangle \simeq \langle \overline{\delta(\Delta)^2} \rangle = \frac{1}{N}\sum_{i=1}^{N} \overline{\delta_i(\Delta)^2}. \tag{1.3}$$

Most cases of intracellular transport dynamics deviate from the linear time dependence or Brownian limit. Many follow the power law form

$$\langle \mathbf{R}(t)^2 \rangle = K_\alpha t^\alpha \tag{1.4}$$

where K_α is the generalized diffusion coefficient and α is the anomalous diffusion exponent. The α parameter distinguishes transport as subdiffusion ($0 < \alpha < 1$), Brownian diffusion ($\alpha \approx 1$), and superdiffusion ($1 < \alpha < 2$) [89, 90, 93, 94].

The MSD is robust with respect to statistical fluctuations and appears easy to interpret making it a powerful tool for studying dynamics. The most prominent intracellular transport is anomalous diffusion characterized by a power-law relationship in the mean squared displacement (MSD) where $\langle \mathbf{R}(\Delta) \rangle \simeq \Delta^{\alpha}$ with $\alpha \neq 1$. This has been observed for intracellular transport with $\alpha = 0.76$ for the time-averaged MSD [95]. Others have reported complex active transport with non-power law MSD with Levy-like behavior [96]. While several processes can exhibit the same α parameter, their other dynamic properties and underlying mechanism can differ [92]. Several order parameters must be assessed to gain an understanding of the physical mechanism of an anomalous process.

1.4 Motivation

Challenges in the study of intracellular insulin granules arise from heterogeneous and stochastic influences on the observed transport in β-cells [95]. Through fluorescence microscopy and single particle tracking, the dynamics of individual granules can be studied individually and as an ensemble to identify characteristic subpopulations of dynamics. Characteristic dynamics observed in intracellular transport, at steady-state and at glucose stimulation, indicate functionally distinct pools that have different mobilization criteria for glucose-stimulated insulin secretion. Elucidation of physical mechanisms underlying biphasic insulin secretion must be inferred from detailed study of intracellular insulin dynamics and the environmental contributions to the transport. Identification of functionally distinct dynamics and their physical mechanisms could provide insight into potential β-cell secretion deficiency and ultimately, mechanisms of β-cell dysfunction defects related to diabetes.

1.5 Structure

This thesis provides a comprehensive analysis of insulin granule transport inspired by earlier research in the Scherer group on the same β-cell system [95, 97–99]. Using CRISPR-cas9 technol-

ogy, the insulin c-peptide is fused with the fluorescent protein mCherry to provide endogenous and full labeling of insulin granules MIN6 β-cells. The development of this line is discussed in Chapter 2 and also in Chapter 3. Endogenous labeling provided a larger data set as well as surprisingly heterogeneous transport over the distribution of the many measured insulin granules that was hidden in the traditional transfection labeling method.

The heterogeneous insulin granule transport is described in detail in Chapter 3 under basal, or non-stimulated, glucose conditions. Remarkably, the highly heterogeneous transport could be objectively separated into five well-characterized and distinct sub-populations based on MSD and other order parameters. The observed transport dynamics are shown to be influenced by the cytoskeletal contributions and also the biogenesis age of the granules. The subdiffusive (subordinated random walk) dynamics that were reported previously in the group in a transfected system [95] are recapitulated in one of the sub-populations found in the CRISPR prepared fully labeled system. Thus, an apparent labeling bias in exogenous labeling of insulin granules hides much of the rich dynamics and motivates the use of full labeling protocols in live cell studies.

Large, local accumulations of granules are also apparent in the fully labeled system. Chapter 4 explores the structure and dynamics of these granule clusters that we term 'scrums'. We determine that scrums act as a dynamic and responsive granule storage system; storage under basal glucose conditions, and large scale granule release during glucose stimulation. A custom developed image analysis method enabled the study of flux dynamics of granules through scrums. The capture and release dynamics are at steady-state, in which the enter and exit rates are the same. The statistical framework for the dynamics provides an interesting model for stochastic counting processes for reaction rate kinetics, conditional probability analysis, and even hidden Markov modeling to understand the storage mechanism.

Interesting new directions include extending research from Chapter 3 and Chapter 4 into three-dimensional, or volumetric, imaging and analysis. Chapter 5 describes the development of a snapshot volumetric microscope [61]. A diffractive optical element (DOE) was designed and fabricated

in a cleanroom on campus that allowed imaging insulin granules in β-cells in a snapshot manner to allow characterizing 3D transport, not just transport in 2D slices by confocal microscopy. We show successful imaging and particle tracking of insulin granules in 3D and find surprising results. A slight anisotropy in the transport favors transport in the XY plane over the axial Z plane. Similar to the new insight from transient labeling to full labeling, we are interested in learning new dynamics and functional interpretations from the added dimension.

Finally, a number of future directions of study, come already initiated, are described in Chapter 6. These include extending studies of intracellular insulin dynamics in 3D grown clusters, termed pseudoislets; volumetric imaging and tracking analysis; and bioelectronic stimulation with voltage response imaging. The first two directions pursue a complete and physiologically relevant picture of insulin granule trafficking. The third direction proposes a new approach for controlled insulin granule secretion. If successful, electric stimulation for insulin secretion could provide an alternate insulin therapy for diabetic patients. These projects have shown promising preliminary results.

Altogether, the studies of insulin granule transport, their storage and release upon cell stimulation, and the altered transport in 3D cell growth conditions (vs. the more common 2D cell monolayer studies) add considerably to our understanding of insulin granule transport in (a mouse model system of) β-cells and implications for treating certain types of Type 2 Diabetes.

REFERENCES

[1] American Diabetes Association. Economic costs of diabetes in the us in 2017. *Diabetes care*, 41(5):917–928, 2018.

[2] Celeste C Thomas and Louis H Philipson. Update on diabetes classification. *Medical Clinics*, 99(1):1–16, 2015.

[3] Yutaka Seino, Kishio Nanjo, Naoko Tajima, Takashi Kadowaki, Atsunori Kashiwagi, Eiichi Araki, Chikako Ito, Nobuya Inagaki, Yasuhiko Iwamoto, Masato Kasuga, et al. Report of the committee on the classification and diagnostic criteria of diabetes mellitus, 2010.

[4] Barbara B Kahn. Type 2 diabetes: when insulin secretion fails to compensate for insulin resistance. *Cell*, 92(5):593–596, 1998.

[5] Ralph A DeFronzo, Rosa Hendler, and Donald Simonson. Insulin resistance is a prominent feature of insulin-dependent diabetes. *Diabetes*, 31(9):795–801, 1982.

[6] Kitt Falk Petersen and Gerald I Shulman. Etiology of insulin resistance. *The American journal of medicine*, 119(5):S10–S16, 2006.

[7] Steven E Shoelson, Jongsoon Lee, Allison B Goldfine, et al. Inflammation and insulin resistance. *The Journal of clinical investigation*, 116(7):1793–1801, 2006.

[8] Frances M Ashcroft and Patrik Rorsman. Diabetes mellitus and the β cell: the last ten years. *Cell*, 148(6):1160–1171, 2012.

[9] JC Florez. Newly identified loci highlight beta cell dysfunction as a key cause of type 2 diabetes: where are the insulin resistance genes? *Diabetologia*, 51(7):1100–1110, 2008.

[10] John R. Petrie, Ewan R. Pearson, and Calum Sutherland. Implications of genome wide association studies for the understanding of type 2 diabetes pathophysiology. *Biochemical Pharmacology*, 81(4):471–477, 2011.

[11] Benjamin F Voight, Laura J Scott, Valgerdur Steinthorsdottir, Andrew P Morris, Christian Dina, Ryan P Welch, Eleftheria Zeggini, Cornelia Huth, Yurii S Aulchenko, Gudmar Thorleifsson, et al. Twelve type 2 diabetes susceptibility loci identified through large-scale association analysis. *Nature genetics*, 42(7):579–589, 2010.

[12] Mark I McCarthy. Genomics, type 2 diabetes, and obesity. *New England Journal of Medicine*, 363(24):2339–2350, 2010.

[13] Mary Elizabeth Patti, Atul J Butte, Sarah Crunkhorn, Kenneth Cusi, Rachele Berria, Sangeeta Kashyap, Yoshinori Miyazaki, Isaac Kohane, Maura Costello, Robert Saccone, et al. Coordinated reduction of genes of oxidative metabolism in humans with insulin resistance and diabetes: Potential role of pgc1 and nrf1. *Proceedings of the National Academy of Sciences*, 100(14):8466–8471, 2003.

[14] Gisela Wilcox. Insulin and insulin resistance. *Clinical biochemist reviews*, 26(2):19, 2005.

[15] John P Hosker, Aram S Rudenski, Melanie A Burnett, David R Matthews, and Robert C Turner. Similar reduction of first-and second-phase b-cell responses at three different glucose levels in type ii diabetes and the effect of gliclazide therapy. *Metabolism*, 38(8):767–772, 1989.

[16] U Smith. Impaired ('diabetic') insulin signaling and action occur in fat cells long before glucose intolerance—is insulin resistance initiated in the adipose tissue? *International journal of obesity*, 26(7):897–904, 2002.

[17] Patrik Rorsman and Frances M Ashcroft. Pancreatic β-cell electrical activity and insulin secretion: of mice and men. *Physiological reviews*, 98(1):117–214, 2018.

[18] Charlotta S Olofsson, Sven O Göpel, Sebastian Barg, Juris Galvanovskis, Xiaosong Ma, Albert Salehi, Patrik Rorsman, and Lena Eliasson. Fast insulin secretion reflects exocytosis of docked granules in mouse pancreatic b-cells. *Pflügers Archiv*, 444(1):43–51, 2002.

[19] Zhuo Fu, Elizabeth R Gilbert, and Dongmin Liu. Regulation of insulin synthesis and secretion and pancreatic beta-cell dysfunction in diabetes. *Current diabetes reviews*, 9(1):25–53, 2013.

[20] Noriko Takahashi, Hiroyasu Hatakeyama, Haruo Okado, Jun Noguchi, Mitsuyo Ohno, and Haruo Kasai. Snare conformational changes that prepare vesicles for exocytosis. *Cell metabolism*, 12(1):19–29, 2010.

[21] Guy A Rutter and Elaine V Hill. Insulin vesicle release: walk, kiss, pause... then run. *Physiology*, 21(3):189–196, 2006.

[22] Troitza K Bratanova-Tochkova, Haiying Cheng, Samira Daniel, Subhadra Gunawardana, Yi-Jia Liu, Jennifer Mulvaney-Musa, Thomas Schermerhorn, Susanne G Straub, Hiroki Yajima, and Geoffrey WG Sharp. Triggering and augmentation mechanisms, granule pools, and biphasic insulin secretion. *Diabetes*, 51(suppl_1):S83–S90, 2002.

[23] Susanne G Straub and Geoffrey WG Sharp. Glucose-stimulated signaling pathways in biphasic insulin secretion. *Diabetes/metabolism research and reviews*, 18(6):451–463, 2002.

[24] Patrik Rorsman and Erik Renström. Insulin granule dynamics in pancreatic beta cells. *Diabetologia*, 46(8):1029–1045, 2003.

[25] Aniko Varadi, Takashi Tsuboi, Linda I Johnson-Cadwell, Victoria J Allan, and Guy A Rutter. Kinesin i and cytoplasmic dynein orchestrate glucose-stimulated insulin-containing vesicle movements in clonal min6 β-cells. *Biochemical and biophysical research communications*, 311(2):272–282, 2003.

[26] Rosita Ivarsson, Stefanie Obermüller, Guy A Rutter, Juris Galvanovskis, and Erik Renström. Temperature-sensitive random insulin granule diffusion is a prerequisite for recruiting granules for release. *Traffic*, 5(10):750–762, 2004.

[27] Aristea E POULI, Evaggelia EMMANOUILIDOU, Chao ZHAO, Christina WASMEIER, John C HUTTON, and Guy A RUTTER. Secretory-granule dynamics visualized in vivo with a phogrin–green fluorescent protein chimaera. *Biochemical Journal*, 333(1):193–199, 1998.

[28] Mingming Hao, Xia Li, Mark A Rizzo, Jonathan V Rocheleau, Benoit M Dawant, and David W Piston. Regulation of two insulin granule populations within the reserve pool by distinct calcium sources. *Journal of cell science*, 118(24):5873–5884, 2005.

[29] June Chunqiu Hou, Le Min, and Jeffrey E Pessin. Insulin granule biogenesis, trafficking and exocytosis. *Vitamins & Hormones*, 80:473–506, 2009.

[30] Nobutaka Hirokawa. Kinesin and dynein superfamily proteins and the mechanism of organelle transport. *Science*, 279(5350):519–526, 1998.

[31] Aniko Varadi, Edward K Ainscow, Victoria J Allan, and Guy A Rutter. Involvement of conventional kinesin in glucose-stimulated secretory granule movements and exocytosis in clonal pancreatic β-cells. *Journal of cell science*, 115(21):4177–4189, 2002.

[32] Jay Newby and Paul C Bressloff. Random intermittent search and the tug-of-war model of motor-driven transport. *Journal of Statistical Mechanics: Theory and Experiment*, 2010(04):P04014, 2010.

[33] Melanie JI Müller, Stefan Klumpp, and Reinhard Lipowsky. Tug-of-war as a cooperative mechanism for bidirectional cargo transport by molecular motors. *Proceedings of the National Academy of Sciences*, 105(12):4609–4614, 2008.

[34] Monika Scholz, Stanislav Burov, Kimberly L Weirich, Björn J Scholz, SM Ali Tabei, Margaret L Gardel, and Aaron R Dinner. Cycling state that can lead to glassy dynamics in intracellular transport. *Physical Review X*, 6(1):011037, 2016.

[35] Yuan X Meng, Glenn W Wilson, Mary C Avery, Crysti H Varden, and Ron Balczon. Suppression of the expression of a pancreatic β-cell form of the kinesin heavy chain by antisense oligonucleotides inhibits insulin secretion from primary cultures of mouse β-cells. *Endocrinology*, 138(5):1979–1987, 1997.

[36] Frederick Gittes, Brian Mickey, Jilda Nettleton, and Jonathon Howard. Flexural rigidity of microtubules and actin filaments measured from thermal fluctuations in shape. *The Journal of cell biology*, 120(4):923–934, 1993.

[37] Carla Pallavicini, Valeria Levi, Diana E Wetzler, Juan F Angiolini, Lorena Benseñor, Marcelo A Despósito, and Luciana Bruno. Lateral motion and bending of microtubules studied with a new single-filament tracking routine in living cells. *Biophysical journal*, 106(12):2625–2635, 2014.

[38] Clifford P Brangwynne, FC MacKintosh, and David A Weitz. Force fluctuations and polymerization dynamics of intracellular microtubules. *Proceedings of the National Academy of Sciences*, 104(41):16128–16133, 2007.

[39] Eric Schulze and Marc Kirschner. New features of microtubule behaviour observed in vivo. *Nature*, 334(6180):356–359, 1988.

[40] Paul J Sammak and Gary G Borisy. Direct observation of microtubule dynamics in living cells. *Nature*, 332(6166):724–726, 1988.

[41] Dimitrije Stamenovic, Srboljub M Mijailovich, Iva Marija Tolic-Nørrelykke, Jianxin Chen, and Ning Wang. Cell prestress. ii. contribution of microtubules. *American Journal of Physiology-Cell Physiology*, 282(3):C617–C624, 2002.

[42] Clifford P Brangwynne, Frederick C MacKintosh, Sanjay Kumar, Nicholas A Geisse, Jennifer Talbot, L Mahadevan, Kevin K Parker, Donald E Ingber, and David A Weitz. Microtubules can bear enhanced compressive loads in living cells because of lateral reinforcement. *The Journal of cell biology*, 173(5):733–741, 2006.

[43] Harindranath Kadavath, Romina V Hofele, Jacek Biernat, Satish Kumar, Katharina Tepper, Henning Urlaub, Eckhard Mandelkow, and Markus Zweckstetter. Tau stabilizes microtubules by binding at the interface between tubulin heterodimers. *Proceedings of the National Academy of Sciences*, 112(24):7501–7506, 2015.

[44] David G Drubin and Marc W Kirschner. Tau protein function in living cells. *The Journal of cell biology*, 103(6):2739–2746, 1986.

[45] Murray D Weingarten, Arthur H Lockwood, Shu-Ying Hwo, and Marc W Kirschner. A protein factor essential for microtubule assembly. *Proceedings of the National Academy of Sciences*, 72(5):1858–1862, 1975.

[46] Harald Felgner, Rainer Frank, Jacek Biernat, Eva-Maria Mandelkow, Eckhard Mandelkow, Beat Ludin, Andrew Matus, and Manfred Schliwa. Domains of neuronal microtubule-associated proteins and flexural rigidity of microtubules. *The Journal of cell biology*, 138(5):1067–1075, 1997.

[47] Glen Lindwall and R David Cole. Phosphorylation affects the ability of tau protein to promote microtubule assembly. *Journal of Biological Chemistry*, 259(8):5301–5305, 1984.

[48] Kung-Hsien Ho, Xiaodun Yang, Anna B Osipovich, Over Cabrera, Mansuo L Hayashi, Mark A Magnuson, Guoqiang Gu, and Irina Kaverina. Glucose regulates microtubule disassembly and the dose of insulin secretion via tau phosphorylation. *Diabetes*, 69(9):1936–1947, 2020.

[49] Aoife T Heaslip, Shane R Nelson, Andrew T Lombardo, Samantha Beck Previs, Jessica Armstrong, and David M Warshaw. Cytoskeletal dependence of insulin granule movement dynamics in ins-1 beta-cells in response to glucose. *PloS one*, 9(10):e109082, 2014.

[50] Xiaodong Zhu, Ruiying Hu, Marcela Brissova, Roland W Stein, Alvin C Powers, Guoqiang Gu, and Irina Kaverina. Microtubules negatively regulate insulin secretion in pancreatic β cells. *Developmental cell*, 34(6):656–668, 2015.

[51] Roberto Dominguez and Kenneth C Holmes. Actin structure and function. *Annual review of biophysics*, 40:169, 2011.

[52] Nikta Fakhri, Alok D Wessel, Charlotte Willms, Matteo Pasquali, Dieter R Klopfenstein, Frederick C MacKintosh, and Christoph F Schmidt. High-resolution mapping of intracellular fluctuations using carbon nanotubes. *Science*, 344(6187):1031–1035, 2014.

[53] Eugene A Katrukha, Marina Mikhaylova, Hugo X van Brakel, Paul M van Bergen En Henegouwen, Anna Akhmanova, Casper C Hoogenraad, and Lukas C Kapitein. Probing cytoskeletal modulation of passive and active intracellular dynamics using nanobody-functionalized quantum dots. *Nature communications*, 8(1):1–8, 2017.

[54] Renu Mohan and Annie John. Microtubule-associated proteins as direct crosslinkers of actin filaments and microtubules. *IUBMB life*, 67(6):395–403, 2015.

[55] GUODONG Li, E Rungger-Brändle, I Just, Jean-Christophe Jonas, K Aktories, and CB Wollheim. Effect of disruption of actin filaments by clostridium botulinum c2 toxin on insulin secretion in hit-t15 cells and pancreatic islets. *Molecular biology of the cell*, 5(11):1199–1213, 1994.

[56] Debbie C Thurmond, Carmen Gonelle-Gispert, Megumi Furukawa, Philippe A Halban, and Jeffrey E Pessin. Glucose-stimulated insulin secretion is coupled to the interaction of actin with the t-snare (target membrane soluble n-ethylmaleimide-sensitive factor attachment protein receptor protein) complex. *Molecular endocrinology*, 17(4):732–742, 2003.

[57] Zhanxiang Wang and Debbie C Thurmond. Mechanisms of biphasic insulin-granule exocytosis–roles of the cytoskeleton, small gtpases and snare proteins. *Journal of cell science*, 122(7):893–903, 2009.

[58] Dieter Rondas, Alejandra Tomas, and Philippe A Halban. Focal adhesion remodeling is crucial for glucose-stimulated insulin secretion and involves activation of focal adhesion kinase and paxillin. *Diabetes*, 60(4):1146–1157, 2011.

[59] Dieter Rondas, Alejandra Tomas, Martinho Soto-Ribeiro, Bernhard Wehrle-Haller, and Philippe A Halban. Novel mechanistic link between focal adhesion remodeling and glucose-stimulated insulin secretion. *Journal of Biological Chemistry*, 287(4):2423–2436, 2012.

[60] James Pawley. *Handbook of biological confocal microscopy*, volume 236. Springer Science & Business Media, 2006.

[61] Xiaolei Wang, Hannah Yi, Itay Gdor, Mark Hereld, and Norbert F Scherer. Nanoscale resolution 3d snapshot particle tracking by multifocal microscopy. *Nano letters*, 19(10):6781–6787, 2019.

[62] Richard N Day and Michael W Davidson. The fluorescent protein palette: tools for cellular imaging. *Chemical Society Reviews*, 38(10):2887–2921, 2009.

[63] Georgyi V Los and Keith Wood. The halotag™. In *High Content Screening*, pages 195–208. Springer, 2007.

[64] Arnaud Gautier, Alexandre Juillerat, Christian Heinis, Ivan Reis Corrêa Jr, Maik Kindermann, Florent Beaufils, and Kai Johnsson. An engineered protein tag for multiprotein labeling in living cells. *Chemistry & biology*, 15(2):128–136, 2008.

[65] Alexandre Juillerat, Thomas Gronemeyer, Antje Keppler, Susanne Gendreizig, Horst Pick, Horst Vogel, and Kai Johnsson. Directed evolution of o6-alkylguanine-dna alkyltransferase for efficient labeling of fusion proteins with small molecules in vivo. *Chemistry & biology*, 10(4):313–317, 2003.

[66] Georgeta Crivat and Justin W Taraska. Imaging proteins inside cells with fluorescent tags. *Trends in biotechnology*, 30(1):8–16, 2012.

[67] Mario R Capecchi. Altering the genome by homologous recombination. *Science*, 244(4910):1288–1292, 1989.

[68] Thomas Gaj, Charles A Gersbach, and Carlos F Barbas III. Zfn, talen, and crispr/cas-based methods for genome engineering. *Trends in biotechnology*, 31(7):397–405, 2013.

[69] FAFA Ran, Patrick D Hsu, Jason Wright, Vineeta Agarwala, David A Scott, and Feng Zhang. Genome engineering using the crispr-cas9 system. *Nature protocols*, 8(11):2281–2308, 2013.

[70] Luhan Yang, Joyce L Yang, Susan Byrne, Joshua Pan, and George M Church. Crispr/cas9-directed genome editing of cultured cells. *Current protocols in molecular biology*, 107(1):31–1, 2014.

[71] Martin Jinek, Alexandra East, Aaron Cheng, Steven Lin, Enbo Ma, and Jennifer Doudna. Rna-programmed genome editing in human cells. *elife*, 2:e00471, 2013.

[72] Martin Jinek, Krzysztof Chylinski, Ines Fonfara, Michael Hauer, Jennifer A Doudna, and Emmanuelle Charpentier. A programmable dual-rna–guided dna endonuclease in adaptive bacterial immunity. *science*, 337(6096):816–821, 2012.

[73] Le Cong, F Ann Ran, David Cox, Shuailiang Lin, Robert Barretto, Naomi Habib, Patrick D Hsu, Xuebing Wu, Wenyan Jiang, Luciano A Marraffini, et al. Multiplex genome engineering using crispr/cas systems. *Science*, 339(6121):819–823, 2013.

[74] M Petran, M Hadravsky, J Benes, and A Boyde. In vivo microscopy using the tandem scanning microscope a. *Annals of the New York Academy of Sciences*, 483(1):440–447, 1986.

[75] GS Kino and GQ Xiao. Real-time scanning optical microscopes, 1990.

[76] GS Kino. Intermediate optics in nipkow disk microscopes. In *Handbook of biological confocal microscopy*, pages 155–165. Springer, 1995.

[77] Jörg Bewersdorf, Rainer Pick, and Stefan W Hell. Multifocal multiphoton microscopy. *Optics letters*, 23(9):655–657, 1998.

[78] David R Sandison, Rebecca M Williams, K Sam Wells, James Strickler, and Watt W Webb. Quantitative fluorescence confocal laser scanning microscopy (clsm). In *Handbook of biological confocal microscopy*, pages 39–53. Springer, 1995.

[79] Sara Abrahamsson, Jiji Chen, Bassam Hajj, Sjoerd Stallinga, Alexander Y Katsov, Jan Wisniewski, Gaku Mizuguchi, Pierre Soule, Florian Mueller, Claire Dugast Darzacq, et al. Fast multicolor 3d imaging using aberration-corrected multifocus microscopy. *Nature methods*, 10(1):60–63, 2013.

[80] Kuan He, Zihao Wang, Xiang Huang, Xiaolei Wang, Seunghwan Yoo, Pablo Ruiz, Itay Gdor, Alan Selewa, Nicola J Ferrier, Norbert Scherer, et al. Computational multifocal microscopy. *Biomedical Optics Express*, 9(12):6477–6496, 2018.

[81] Stanislav Burov, SM Ali Tabei, Toan Huynh, Michael P Murrell, Louis H Philipson, Stuart A Rice, Margaret L Gardel, Norbert F Scherer, and Aaron R Dinner. Distribution of directional change as a signature of complex dynamics. *Proceedings of the National Academy of Sciences*, 110(49):19689–19694, 2013.

[82] John C Crocker and David G Grier. Methods of digital video microscopy for colloidal studies. *Journal of colloid and interface science*, 179(1):298–310, 1996.

[83] Denis Wirtz et al. Particle-tracking microrheology of living cells: principles and applications. *Annual review of biophysics*, 38(1):301–326, 2009.

[84] Ivo F Sbalzarini and Petros Koumoutsakos. Feature point tracking and trajectory analysis for video imaging in cell biology. *Journal of structural biology*, 151(2):182–195, 2005.

[85] Jean-Yves Tinevez, Nick Perry, Johannes Schindelin, Genevieve M Hoopes, Gregory D Reynolds, Emmanuel Laplantine, Sebastian Y Bednarek, Spencer L Shorte, and Kevin W Eliceiri. Trackmate: An open and extensible platform for single-particle tracking. *Methods*, 115:80–90, 2017.

[86] Jay M Newby, Alison M Schaefer, Phoebe T Lee, M Gregory Forest, and Samuel K Lai. Convolutional neural networks automate detection for tracking of submicron-scale particles in 2d and 3d. *Proceedings of the National Academy of Sciences*, 115(36):9026–9031, 2018.

[87] Rhodri S Wilson, Lei Yang, Alison Dun, Annya M Smyth, Rory R Duncan, Colin Rickman, and Weiping Lu. Automated single particle detection and tracking for large microscopy datasets. *Royal Society open science*, 3(5):160225, 2016.

[88] Joseph Redmon and Ali Farhadi. Yolo9000: better, faster, stronger. In *Proceedings of the IEEE conference on computer vision and pattern recognition*, pages 7263–7271, 2017.

[89] Ralf Metzler and Joseph Klafter. The random walk's guide to anomalous diffusion: a fractional dynamics approach. *Physics reports*, 339(1):1–77, 2000.

[90] Felix Höfling and Thomas Franosch. Anomalous transport in the crowded world of biological cells. *Reports on Progress in Physics*, 76(4):046602, 2013.

[91] Albert Einstein et al. On the electrodynamics of moving bodies. *Annalen der physik*, 17(10):891–921, 1905.

[92] R Metzler, J-H Jeon, and AG Cherstvy. Non-brownian diffusion in lipid membranes: Experiments and simulations. *Biochimica et Biophysica Acta (BBA)-Biomembranes*, 1858(10):2451–2467, 2016.

[93] Carlo Manzo and Maria F Garcia-Parajo. A review of progress in single particle tracking: from methods to biophysical insights. *Reports on progress in physics*, 78(12):124601, 2015.

[94] Yasmine Meroz and Igor M Sokolov. A toolbox for determining subdiffusive mechanisms. *Physics Reports*, 573:1–29, 2015.

[95] SM Ali Tabei, Stanislav Burov, Hee Y Kim, Andrey Kuznetsov, Toan Huynh, Justin Jureller, Louis H Philipson, Aaron R Dinner, and Norbert F Scherer. Intracellular transport of insulin granules is a subordinated random walk. *Proceedings of the National Academy of Sciences*, 110(13):4911–4916, 2013.

[96] Kejia Chen, Bo Wang, and Steve Granick. Memoryless self-reinforcing directionality in endosomal active transport within living cells. *Nature Materials*, 14(6):589–593, 2015.

[97] Toan Huynh. *THE BIOLOGY AND PHYSICS OF INSULIN GRANULE TRANSPORT, AND DIGITAL CHEMISTRY FOR DIAGNOSTICS*. PhD thesis, University of Chicago, 2014.

[98] Hee Young (Amy) Kim. *QUANTIFYING GRANULE TRANSPORT AND CONTROLLING CALCIUM OSCILLATIONS IN INSULIN SECRETING BETA CELLS*. PhD thesis, University of Chicago, 2010.

[99] Justin Jureller. *NONLINEAR AND CORRELATION MICROSCOPIES FOR DYNAMICS AND FUNCTION IN HETEROGENEOUS SYSTEMS*. PhD thesis, University of Chicago, 2006.

CHAPTER 2

EXPERIMENTAL METHODS

2.1 Fluorescent Microscopy

2.1.1 Wide-field Microscopy

The inverted microscope (Nikon Eclipse Ti) is housed in a temperature controlled and acoustically damped enclosure. A solid-state LED light source (Lumencor, Spectral X light engine) with highly stable output was coupled to the microscope with a liquid light guide. The excitation light was bandpass filtered (Semrock FF01-578/21-25) with a maximum power of 515 mW in the range of 568–589 nm used for wide-field illumination. Samples were mounted on a mechanical stage (Ludl 99S106-N2K-LE2, MAC5000 controller). Fluorescence emission collected by the objective (Nikon 60× 1.27 NA CFI Plan Apo water immersion, MRD07650) was separated from the excitation light by a dichroic mirror (Semrock, FF596-Di01-25 × 36) and bandpass filter (Semrock, FF02-641/75-25).

The wide-field system is used as the base for the multifocal microscope. The right port of the microscope is used to conventional wide-field microscopy and the image is recorded with a sCMOS camera (Teledyne Photometrics, Prime BSI). The left port extends to the 4-f relay lens system described in Section 2.1.3.

2.1.2 Confocal Microscopy

The microscope used for live cell imaging is an inverted microscope body (Nikon Ti), spinning disk confocal scanner (Yokogawa CSW1), 100x oil objective (Nikon, PlanApo) and EMCCD detector (iXON 888). The mCherry fluorescence is excited using a 561 nm laser diode (Spectra-Physics, Excelsior One) and emission is filtered at 610 nm (Chroma). Cells are maintained at 37 ^{o}C using a home-built microscope camber and heating element. Meanwhile, CO_2 is buffered from the HEPES

reagent in the imaging solution. Total time for imaging sessions is under 30 min, which is an empirical guideline such that the HEPES regent is not used up.

Microscopy image stacks are recorded at 10 Hz frame rate for 2000 frames; a total image acquisition time of 200 s. Imaging sessions are <30 min per sample and multiple image stacks are recorded per sample. Image stacks are saved as unsigned 16-bit TIFF files and subsequently analyzed using ImageJ and MATLAB.

2.1.3 Multifocal Microscopy

A custom-built MFM was developed as an extension to a commercial (Nikon Eclipse Ti) inverted microscope [1]. The microscope is housed in a temperature controlled and acoustically damped enclosure. A solid-state LED light source (Lumencor, Spectral X light engine) with highly stable output was coupled to the microscope with a liquid light guide. The excitation light was bandpass filtered (Semrock FF01-578/21-25) with a maximum power of 515 mW in the range of 568–589 nm used for wide-field illumination. Samples were mounted on a mechanical stage (Ludl 99S106-N2K-LE2, MAC5000 controller). Fluorescence emission collected by the objective (Nikon 60× 1.27 NA CFI Plan Apo water immersion, MRD07650) was separated from the excitation light by a dichroic mirror (Semrock, FF596-Di01-25 × 36) and bandpass filter (Semrock, FF02-641/75-25). An in-house fabricated metal-on-glass field stop was placed at the primary image plane, which crops the image plane to 2 mm^2 (or 33 μm^2 sample field of view) for MFM. The field stop consisted of a 200 nm Cr layer with a 2 mm square clear region deposited on a circular 25.4 mm diameter by 1 mm thick fused silica substrate (Thorlabs WG41010). A 4-f lens system relayed the image from the primary image plane to a second image plane on the detector (Andor iXon 888 EMCCD). The first lens (f = 200 mm, Thorlabs AC508-200-A) matched the focal length of the tube lens (Nikon, f = 200 mm) and generated the secondary pupil (Fourier) plane where the MFM diffractive optical element (DOE) was placed. Figure 1 shows the binary patterned DOE fabricated for the present study, which has a unit cell period of 56 μm and design focal shift, Δz, of 600 nm

(see Supporting Information for details). The second lens (f = 400 mm, Thorlabs AC508-400-A) focused the fluorescence emission from the DOE onto the EMCCD detector. A second narrower bandpass filter (Semrock, FF01-620/14-25) was placed after the DOE to narrow the bandwidth of the emission light to mitigate chromatic aberration.

Diffractive optical element fabrication

The DOE for multifocal microscopy (MFM) was designed to create a 3x3 array of sub-images (tiles) that have a focal shift of 600 nm [1, 2]. The binary patterned DOE fabricated for the present study has a unit cell period of 56 μm and design focal shift, Δz, of 600nm. Our DOE is designed for a (fluorescence) wavelength of 610nm with emission light distributed evenly and efficiently (67%) among the nine tiles. We fabricated the DOE in-house on a 5 mm thick 25mm diameter UV fused silica substrate (WG41050, Thorlabs). The fused silica window was cleaned with acetone, isopropyl alcohol and distilled water, then spin-coated with a 1.5 μm thick layer of AZ1512 photoresist (Shipley). A laser writer (Heidelberg MLA150) exposed the desired pattern at 0.5 μm pixel resolution in the photoresist (405 nm laser at a dose of 150 mJ/cm^2). The photoresist was developed in AZ-300 MIF developer (Integrated Micro Materials) for 20 s. The window with the pattern written in photoresist was etched in a reactive ion etcher (RIE, Oxford Instruments). The glass substrate was etched to a depth of 680nm for the design wavelength of 610nm using Ar gas (25 standard cubic centimeters per minute (sccm)) and CHF_3 (25 sccm), and 200 W RF power for about 28 min. The photoresist remaining after etching was stripped with acetone in an ultrasonic bath. The etching depth and surface roughness of the DOE were measured with contact profilometry (Bruker Dektak XT-S profilometer). All fabrication steps were completed at the Pritzker Nanofabrication Facility and the Searle Cleanroom Facility at the University of Chicago.

2.2 Cell Culture and Biological Preparation

2.2.1 Cell Growth and Maintenance

Low Passage MIN6 sublines were grown single cells of the "wild-type" MIN6 culture kindly gifted from Dr. Louis Philipson at The University of Chicago. A MIN6 subline transduced via CRISPR-Cas9 technology to insert the mCherry gene into the C-peptide sequence. The resultant cells are cultured in high glucose DMEM (Gibco, 11965092) supplemented with 10% Serum Plus-II (MilliporeSigma, 14009C) and 200 uL/mL Penicillin/Streptavidin (Gibco, 15140122). Cells are incubated in 5.0% CO_2 at 37.5 ^oC with high humidity. Media is replaced every 2-3 days. Cell cultures are passaged at 90% confluence using Versene (Gibco, 15040066) and Trypsin (Gibco, 25200056) at manufacturer's recommended protocol.

Cells used in this thesis were passage 5-20. From the trypsin-ized cell mixture from cell passage, a small aliquot 100-500 μL is placed on a glass bottom imaging dish (Matek, P35G-1.5-10-C) then allowed to sit for 6 h or until the cells to adhere to the glass bottom. Cells are then fed with 2 mL of growth media and allowed to incubate overnight. Growth media is replaced with 28 mM glucose in Krebs-Ringer Buffer (KRB, 132 mM NaCl, 4.7 mM KCl, 2.5 mM $CaCl_2$, 1.2 mM $MgSO_4$, 1.2 mM KH_2PO_4, 2 mM $NaHCO_3$, pH 7.4) with 10mM HEPES. Cells are incubated for 30 min in buffer before imaging on the confocal microscope.

2.2.2 CRISPR editing

The insulin-GFP guideRNA (gRNA) was designed using a previously characterized insulin-GFP plasmid, where the GFP is integrated immediately downstream and in-frame with the insulin C-peptide sequence [3]. The in-frame, C-peptide insertion is mandatory as traditional C and N terminus insertions of fluorescent proteins are associated with misfolded insulin, poor granule formation, and cell toxicity [4, 5]. The C-peptide is an attractive target for fluorescent protein fusion because it co-localized with insulin in granules at equimolar concentrations [6]. Furthermore, the C-peptide

is a common analytic handle for detecting stimulated secretion levels because of its higher stability in extracellular space compared to insulin [7].

Insulin-mCherry construct was designed similarly by aligning the mCherry sequence to the original insulin-GFP construct so that the mCherry sequence would also be downstream and in-frame with the C-peptide. Homology arms extending beyond the gene encoding region were designed to flank the gRNA to localize it to the genomic site of insulin-2. A CRISPR plasmid was generated using the Optimized CRISPR design tool to identify an appropriate cut site near the insulin-2 gene. The gRNA sequence was then incorporated into a plasmid that contained Cas9 protein. Previously described MIN6 sublines that are highly, moderately, and nonresponsive to glucose stimulation were transduced at low passage with the CRISPR plasmids. The resulting fluorescent cells were isolated through three rounds of flow cytometry to generate a mostly pure population of MIN6 cells expressing mCherry-Ins2.

2.2.3 Glucose Stimulation

Replace normal growth medium with starvation growth medium (dilute 4.5g/L glucose DMEM in (-)glucose DMEM supplemented with FBS and PS to 2-2.8mM (36-50 mg/dL, 0.36-0.5g/L) glucose) overnight. Replace starvation media with 28mM glucose in KRB with HEPES and incubate for 30 min before imaging.

For imaging low to high glucose dynamics, replace normal growth medium with starvation medium as above. Replace starvation media with 2.8 mM glucose + 25.2 mM mannitol in KRB with HEPES and incubate for 30 min before imaging. After imaging the low glucose dynamics, carefully remove the low glucose KRB with a pipet. Slowly add high glucose KRB (28mM glucose 0mM mannitol in KRB with HEPES) to the imaging dish. These steps are done with minimal disturbance to the dish or stage so the the field of view does not change during manipulation. The change in glucose content in KRB will affect the osmotic pressure of the cell and can elicit signalling that is not related to glucose stimulated response.

2.3 Image Processing

2.3.1 Single Particle Tracking

Single particle tracking is carried out in two steps: particle localization and trajectory linking. The 'raw' trajectory list is obtained from the MOSAIC plug-in from ImageJ[8] which allows for quick parameter adjustment (radius, cutoff, percent) and subsequent image verification. The percent allowed parameter is chosen to accept more false positives, such that the number of false negatives is minimized. The particle localizations at the given radius size has a small particle localization bias towards the center of the 'metapixel'. The SPIFF algorithm is used to remove the localization bias from the XY coordinates [9, 10].

Large groupings of particles are observed in addition to the singular granules. Two particle radii are used for particle localization to capture the singular particles (5 px radius) and large clusters (15 px radius). Singular particle localizations with coincident time frame and position as the large cluster localizations are removed from the singular granules list. The list of singular granules containing X position, Y position, and time frame is then linked into trajectory lists containing X position, Y position, time frame, and trajectory ID. The Crocker-Grier linking algorithm is used which minimizes the distance traveled between all the particles in two consecutive frames[11].

False positive and false negatives from particle tracking are assumed to be present within the trajectory list. The presence of false positives is large since the particle localization parameters are chosen to minimize the number of false negatives. The resultant trajectories for false positives are short in time length (>5 time frames). Trajectories that are shorter than 15 time frames are removed from the trajectory list.

2.3.2 Scrum Flux

Granule enter or exit events are identified as the time when a granule trajectory crosses a pre-defined interaction radius centered at the scrum. The number of detected events scales linearly with

the interaction radius because the perimeter of the interaction circle ($2\pi r$) also increases linearly with radius (r). So, the total size of the detection circle is increased with larger radius thus allowing for more possible detected events. A detection annulus is defined to reduce the number of granule trajectories that are tested for interaction radius crossing. The number of candidate trajectories is far smaller than the total number of granule trajectories; typically 10-30 potentially interacting granule trajectories out of nearly 200,000 total granule trajectories.

To calculate enter and exits events through a scrum with a specified interaction radius, r_2, all candidate trajectories ($R'_g(x, y, t, id)$) are first identified from the list of all granule trajectories ($R_g(x, y, t, id)$) for a scrum trajectory ($R_s(x, y, t, id)$) as

$$R'_g = R_s + r_2 \leq R_g \leq R_s + r_1 \tag{2.1}$$

where r_2, the outer radius of the annulus is always 1.5 px + r_1. Note that all granule trajectories (every granule id) are analyzed for each single scrum trajectory (per scrum id). The width of the detection ring (1.5 px) was chosen from the distribution of step sizes for granule trajectories. The 1.5 px annulus width is sufficiently large enough to capture > 90% of trajectory steps based on the experimentally derived step size distribution of all analyzed trajectories.

REFERENCES

[1] Xiaolei Wang, Xiang Huang, Itay Gdor, Matthew Daddysman, Hannah Yi, Alan Selewa, Theresa Haunold, Mark Hereld, and Norbert F Scherer. Snapshot 3d tracking of insulin granules in live cells. In *Three-Dimensional and Multidimensional Microscopy: Image Acquisition and Processing XXV*, volume 10499, pages 33–39. SPIE, 2018.

[2] Sara Abrahamsson, Jiji Chen, Bassam Hajj, Sjoerd Stallinga, Alexander Y Katsov, Jan Wisniewski, Gaku Mizuguchi, Pierre Soule, Florian Mueller, Claire Dugast Darzacq, et al. Fast multicolor 3d imaging using aberration-corrected multifocus microscopy. *Nature methods*, 10(1):60–63, 2013.

[3] Sindhu Rajan, Stefani C Eames, Soo-Young Park, Christine Labno, Graeme I Bell, Victoria E Prince, and Louis H Philipson. In vitro processing and secretion of mutant insulin proteins that cause permanent neonatal diabetes. *American Journal of Physiology-Endocrinology and Metabolism*, 298(3):E403–E410, 2010.

[4] Aristea E POULI, Evaggelia EMMANOUILIDOU, Chao ZHAO, Christina WASMEIER, John C HUTTON, and Guy A RUTTER. Secretory-granule dynamics visualized in vivo with a phogrin–green fluorescent protein chimaera. *Biochemical Journal*, 333(1):193–199, 1998.

[5] Simon Watkins, Xuehui Geng, Lehong Li, Glenn Papworth, Paul D Robbins, and Peter Drain. Imaging secretory vesicles by fluorescent protein insertion in propeptide rather than mature secreted peptide. *Traffic*, 3(7):461–471, 2002.

[6] Michael Weiss, Donald F Steiner, and Louis H Philipson. Insulin biosynthesis, secretion, structure, and structure-activity relationships. 2015.

[7] Gina LC Yosten and Grant R Kolar. The physiology of proinsulin c-peptide: unanswered questions and a proposed model. *Physiology*, 30(4):327–332, 2015.

[8] Ivo F Sbalzarini and Petros Koumoutsakos. Feature point tracking and trajectory analysis for video imaging in cell biology. *Journal of structural biology*, 151(2):182–195, 2005.

[9] Yuval Yifat, Nishant Sule, Yihan Lin, and Norbert F Scherer. Analysis and correction of errors in nanoscale particle tracking using the single-pixel interior filling function (spiff) algorithm. *Scientific reports*, 7(1):1–10, 2017.

[10] Stanislav Burov, Patrick Figliozzi, Binhua Lin, Stuart A Rice, Norbert F Scherer, and Aaron R Dinner. Single-pixel interior filling function approach for detecting and correcting errors in particle tracking. *Proceedings of the National Academy of Sciences*, 114(2):221–226, 2017.

[11] John C Crocker and David G Grier. Methods of digital video microscopy for colloidal studies. *Journal of colloid and interface science*, 179(1):298–310, 1996.

CHAPTER 3

SPATIAL-DEPENDENT CYTOSKELETON MORPHOLOGY AND INSULIN GRANULE AGE CAUSE THEIR HETEROGENEOUS TRANSPORT IN A MODEL BETA-CELL SYSTEM

3.1 Abstract

Intracellular transport of insulin granules is a highly heterogeneous process that is difficult to be described by a general model. To better understand how this heterogeneity is affected by different intracellular factors, here we constructed a MIN6 cell line constantly expressing mCherry fused insulin granules, and did single particle tracking of the granule transport at different time stages, different spatial regimes, and different cytoskeletal environments. Based on Mean Squared Displacement (MSD), angle distribution, step size distribution, and other metrics, we identified 5 distinct populations of transport traces. Each population has a unique signature of characters and illustrates the strong heterogeneity of insulin granule transport. We show the distribution of the 5 populations has a strong dependence on the time stage of insulin granules. The 5 populations also characterize the function of local microtubule and actin networks at different spatial regions in the transport process. Our results provide robust metrics to clarify the heterogeneity of the dynamics of granule transport and show a comprehensive picture of how different time-spatial dependent intracellular factors contribute to this heterogeneity.

3.2 Introduction

Life at the intracellular scale is inherently stochastic. Intracellular trafficking of cargo (i.e., vesicles with macromolecular contents) is one example of a complex process that defies simple general descriptions. Despite the seemingly random movement of vesicle cargo, cells carry out extraordinarily coordinated metabolic processes using biomolecules transported in vesicles to survive

and thrive. The complexity of motor protein mediated cargo transport is influenced by the organelle dense intracellular environment[1, 2], fluctuating cytoskeletal polymers[3–5], and the cell's metabolic state[6]. As this paper will show, connections between transport and cellular function can be established through comprehensive single "particle" measurements, tracking, and analysis.

Secretory vesicles inherent to synaptic secretion of neurotransmitters [7, 8] and separately in glucose stimulated insulin secretion[9] have long been hypothesized to exist in distinct "pools" segregated by function (readily releasable vs reserve) associated with stimulated secretion. Indicators to infer the functional pool of a secretory vesicle are essential for understanding vesicle secretion dynamics at steady-state and after stimulation. Young, or newly synthesized, vesicles are functionally distinct as priority in the rapid first phase of stimulated secretion[7, 10]. Notably, young vesicles are further distinguished by their characteristic motion (experimentally quantified by trajectories) of confined transport localized near the membrane of the cell. This is evidence that characteristic motion in intracellular trafficking can be identifiers of functional roles of vesicles.

Many types of intracellular motion have been quantified beyond this specific example to elucidate the interplay between cargo transport and its many influencing factors. Measurements using small quantum dot probes elucidate diffusive transport [4], while larger carbon nanotube probes reveal driven even cyclic transport [3]. Systematic in vitro measurements in varying probe diameters and actin pore sizes reveal that transport transitions from diffusive to continuous time random walks (CTRW) to fractional Brownian motion (fBm) with increasing probe size for a given actin mesh density[11]. Even "subordinated" random walk statistics, a hierarchical combination of CTRW and fBm, is found in live cells[12, 13]. Finally, single vs. multi-motored system reveal unexpected cyclic motion and temporal traps[14]. Clearly the transport that occurs depends on many factors, some that are intrinsic, and others - such as the choice of probe - are extrinsic, so measuring biologically relevant dynamics should ideally be done with probes that are "native" to the cellular system.

Kinesin motor proteins on the microtubule tracks using the motor-cargo mechanism mediate

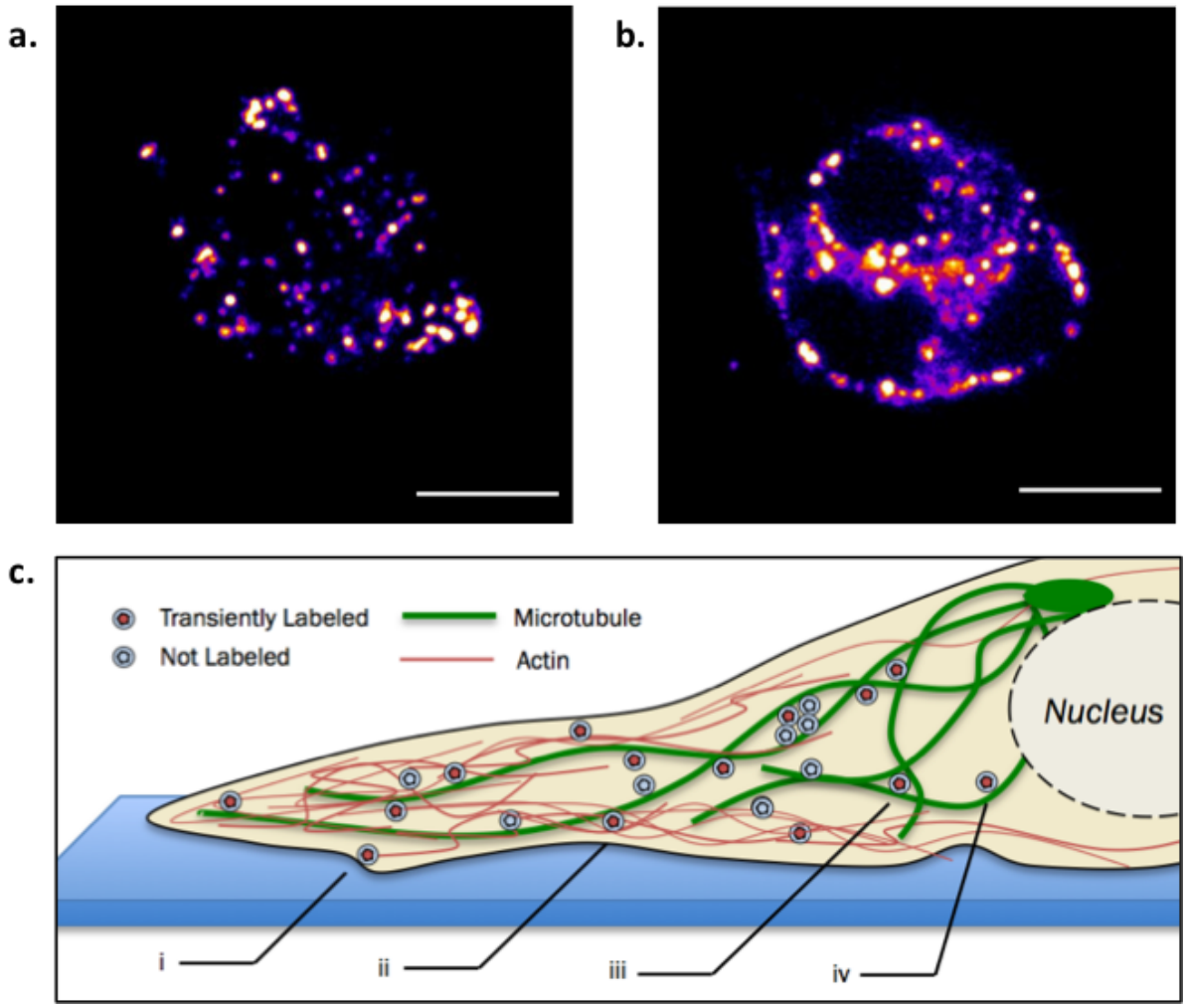

Figure 3.1: **CRISPR labeled insulin granules with mCherry in MIN6 model β-cell line.** Live cell imaging of fluorescently labeled insulin granules at (a) the bottom imaging plane, near the coverslip, and (b) in the middle of the monolayer grown cell cluster, about 4 um away from the coverslip. The schematic in (c) illustrates the differing cytoskeletal environments in the two imaging planes above in (a) and (b). While microtubule networks (green lines) are evenly dispersed within the intracellular space, actin networks (red lines) are densely concentrated near the plasma membrane, and consequently near the coverslip. The highly heterogeneous intracellular space contributes to varied granule transport characteristics: (i) docked (ii) dense actin environment (iii) microtubule traps and (iv) unhindered. Additional biases in labeling studies arise from the use of transiently transfected fluorescent probes for insulin granules (red circles) which selectively tag newly packaged vesicles and leave older, unlabeled granules (gray circles) undetected. Scale: 10um

insulin granule transport. Dynamics of intracellular vesicle transport is complex and influenced by multiple factors in the heterogeneous and crowded intracellular environment. As more motors are associated to a vesicle, spatially confining effects increase by way of multi-motor mechanisms such as tug-of-war[15] or cycling dynamics[14]. Local environmental effects further influence granule transport, particularly in actin dense regions that can act as an active influence and also a hindrance to vesicle transport. The composition of the intracellular landscape changes when comparing a planar cross-section near the coverslip (Figure 3.1a) or the middle of the cell (Figure 3.1b). Imaging planes near the coverslip yield higher signal to noise in imaging but the environment is dense in actin, which is an active mesh network modulated by myosin motor interactions with the filaments. The resulting insulin granule dynamics near the coverslip have influence from actin dynamics. Granule dynamics near the middle of the cell only have cytoskeletal influence from the microtubule network although the out-of-focus fluorescence yield poorer imaging conditions.

Single particle tracking is a powerful tool for studying intracellular transport, providing rich statistical data for analysis and deduction of the aforementioned complex and stochastic dynamics[16]. Centroid localization of sufficiently bright single particle "probes" allow obtaining reliable trajectories that are ideally of sufficient length, spanning decades in duration[17, 18]. Many such trajectories distributed throughout the cellular volume must also be obtained for adequate sampling of behaviors. Reliable fluorescence-based imaging is required to yield minimal photobleaching and high signal-to-noise so to maximize particle detection and tracking over time. Fluorescent protein fusion by transient transfection has long been used to tag intracellular targets for live cell imaging. This approach leads to age biases insulin granule sampling since only granules packaged after plasmid introduction are labeled and imaged. Pioneering work in genomic editing allows for alternative tagging methods, particularly with CRISPR technology, to create transgenic lines that overcome the sampling bias[19]. Using this, we study insulin granule transport by single particle tracking in MIN6 cells that constitutively express mCherry labelled insulin.

In this chapter, we show that the highly heterogeneous ensemble of insulin granule traces is

categorized into five populations with characteristic time-scaled behavior. We developed a stable cell line that constitutively expresses mCherry labelled insulin to sample the entire granule population that also resulted in brighter targets with negligible photobleaching at our imaging parameters. The populations are distinguished by their TA-MSD, angle correlation, and age. By measuring two z-planes, the bottom (Figure 3.1a) and the middle (Figure 3.1b), we probe the contribution of actin in vesicle trafficking by drug disruption. While microtubule disruption are confirm the expected result that kinesin-based vesicle transport is microtubule mediated, we also find surprising and seemingly conflicting results in the contribution of actin within insulin transport.

3.3 Constitutive expression of mCherry labeled insulin allows for reliable imaging for dynamic studies

The insulin-GFP guideRNA (gRNA) was designed using a previously characterized insulin-GFP plasmid, where the GFP is integrated immediately downstream and in-frame with the insulin C-peptide sequence [20]. The in-frame, C-peptide insertion is mandatory as traditional C and N terminus insertions of fluorescent proteins are associated with misfolded insulin, poor granule formation, and cell toxicity [21, 22]. The C-peptide is an attractive target for fluorescent protein fusion because it co-localized with insulin in granules at equimolar concentrations [23]. Furthermore, the C-peptide is a common analytic handle for detecting stimulated secretion levels because of its higher stability in extracellular space compared to insulin [24].

Insulin-mCherry construct was designed similarly by aligning the mCherry sequence to the original insulin-GFP construct so that the mCherry sequence would also be downstream and in-frame with the C-peptide. Homology arms extending beyond the gene encoding region were designed to flank the gRNA to localize it to the genomic site of insulin-2. A CRISPR plasmid was generated using the Optimized CRISPR design tool to identify an appropriate cut site near the insulin-2 gene. The gRNA sequence was then incorporated into a plasmid that contained Cas9 protein. Previously described MIN6 sublines that are highly, moderately, and nonresponsive to

glucose stimulation were transduced at low passage with the CRISPR plasmids. The resulting fluorescent cells were isolated through three rounds of flow cytometry to generate a mostly pure population of MIN6 cells expressing mCherry-Ins2.

The resultant stably expressing cell lines show superior brightness and photostability. The genomic incorporation of the fluorescent protein construct leads to full labeling of insulin granules. Minimal photobleaching during live cell imaging due to the high density of fluorophores per granule leads to longer trajectories from single particle tracking analysis. In addition to superior imaging properties (see 3.1), the CRISPR labeled cell lines exhibit more trackable insulin granules per cell (60 granules/cell) compared to transient transfection labeled cells (~20 granules/cell) (i.e. Figure 3.5).

3.4 Multi-scale time metrics to probe complex and diverse transport

The trajectories obtained from single particle tracking contained diverse dynamics ranging from confined transport to driven motion (Figure 3.2a). In many cases, we observed complex transport patterns with run-pause motion (Levy-like). These complex trajectories are challenging to characterize because of the two state dynamics (active and confined states) that are apparent at larger time scales, and self-similarly at smaller time scales (Figure 3.2b). In addition to analyzing these complex trajectories, metrics used for trajectory analysis required the ability to also describe the dynamics of confined, diffusive, and driven motion.

Transport metrics are assessed at multiple lag times to diagnose transport characteristics for local and overall trajectory motion. A lag time (Δ) is a sliding analysis window to assess transport metrics and is most commonly used in calculating mean squared displacement (MSD). Multiple scales of lag times allows sensitivity to local behavior at short lag times and overall behavior at long lag times. In cases of confined trajectories (Figure 3.2c), the sub-sampled trajectories at short lag times resolve the confined behavior with sharp turning angles while the resultant trajectories at long lag times identify the overall small displacement. Similarly for run-pause trajectories (Figure

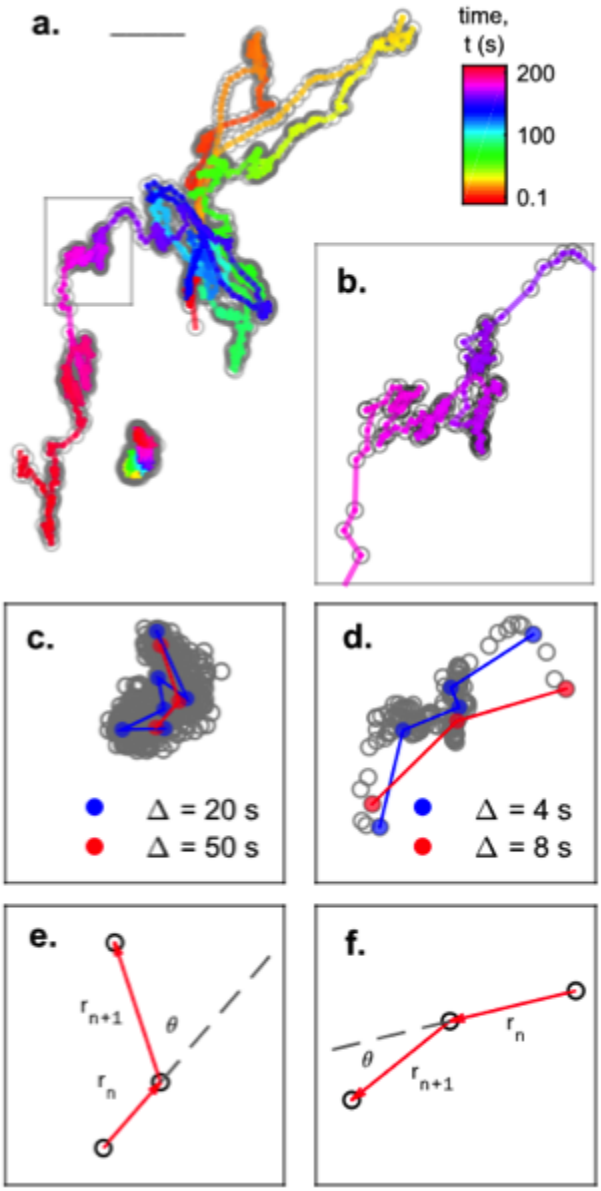

Figure 3.2: **Analysis of transport based on lag time.**(a) Intracellular transport is highly heterogeneous at the trajectory level that can be separated into populations as shown by two sample trajectories of comparable length. Scale: 1μm. (b) In complex modes of transport like run-pause, transport is heterogeneous in the sub-trajectory level that shows a zoom from the gray box in Figure 3.2a. (c&d) Distinct features can be extracted by using specific lag times for analysis. Trajectories subsampled at short lagtimes, blue, detect confined behavior while those at long lag times, red, show the overall direction of transport. (e&f) Their corresponding step size, r, and turning angle, θ, are used to describe the subsampled trajectory's motion as shown in the coordinate system illustrated from the long lag time subtrajectories obtained from Figure 3.2c-d.

3.2d), shorter lag times extract confined characteristics from the pause regions shown by the sharp turning traces and longer lag times show the direction and displacement of the run regions. This multi-scale lag time approach affords a single analysis method to analyze a diverse ensemble for insulin granule transport dynamics ranging from complex run-pause motion to anomalous diffusion and even immobilized motion.

Direction and displacement are the two fundamental coordinates to characterize motion. To analyze the motion at multiple lag times, the Euclidian distance (r) of each vector from the lag time selection and turning angle (θ) from subsequent vectors is computed (Figure 3.2e-f). The average Euclidian distances at a given time lag (Δ) is the ubiquitous mean squared displacement (MSD). The average turning angles at a given lag time (θ) is more novel and this turning angle analysis is an excellent reporter for confined vs directed motion[25].

3.5 Heterogeneous dynamics in insulin granule transport is separated into 5 transport populations

The heterogeneity shown in the ensemble of singular granules using metrics described above is clustered into five characteristic transport classes: immobile, nearly immobile, run-pause, superdiffusive and subdiffusive (Figure 3.3a). Transport populations have a distinct EA-MSD with varying α scaling and short vs long lag time behavior (Figure 3.3b). The TA-MSD for each individual granule trajectory is sorted based on its scaling exponent, α, and power-law behavior as a function of time lag (Figure 3.3c-g). Two parameters of each TA-MSD are used for separation. Transport modes following power-law statistics are the most commonly observed populations (Figure 3.3h). Anomalous behavior is attributed to crowding in the intracellular environment, particularly from the influence cytoskeletal structures[2, 26, 27].

After separation into populations, the constituent time-averaged MSDs align with the overall ensemble-averaged MSDs which suggests that while each population is unique, populations are well-defined in their characteristics. Three transport populations are governed by power-law

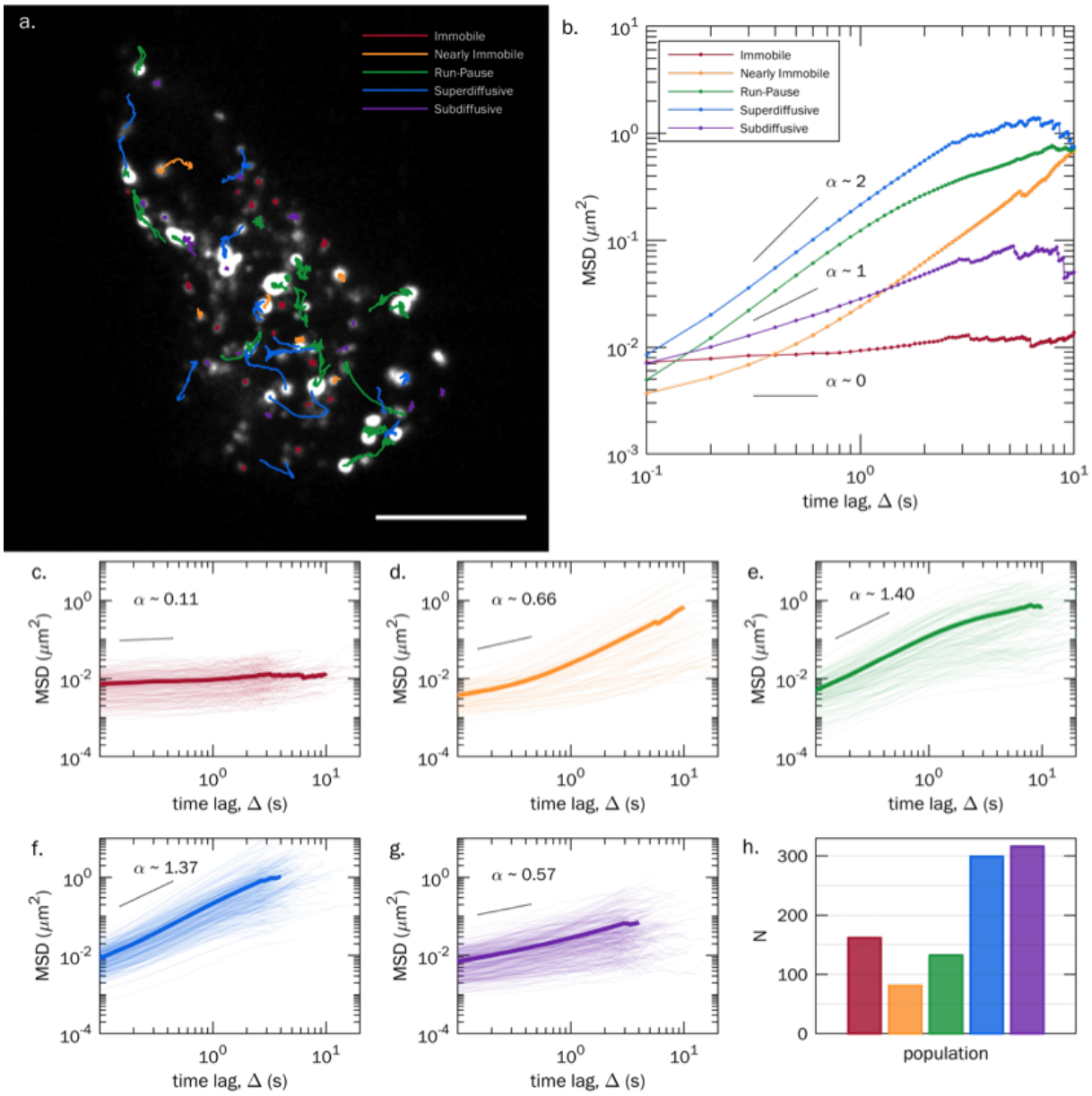

Figure 3.3: **Highly heterogeneous granule dynamics are clustered into five distinct transport populations.**(a) Single particle tracking of insulin granules displays heterogeneous transport. Individual tracks are separated into five distinct transport populations based on their time averaged mean squared displacement (TA-MSD) and the resulting ensemble averaged mean squared displacement (EA-MSD) of each population is unique. Not all trajectories are shown. (b) EA-MSD of five populations. Points are data of analyzed time lags and are connected by lines segments. EA-MSDs are the same in b compared to c-g thick lines. (c-g) TA-MSD of individual traces in each population compared to the EA-MSD plotted with a thicker line. Note that the last 25% of points are truncated from each plot to remove noisy and statistically insignificant traces. Colors of TA-MSD plots are consistent to Figure 3.3a-b. The number of traces in each population used to construct c-d is shown (h).

statistics. These are classified as immobile ($\alpha \approx 0$), subdiffusive ($0 < \alpha < 1$), and superdiffuisve ($1 < \alpha < 2$). Two populations follow behaviors that are not well defined by power-law statistics. Nearly immobile trajectories look immobile at short time scales, or small lag time, but have a small overall movement at longer lag times. Levy-like, run-pause motion is observed within a population of granules.

Many studies have also identified characteristic trajectory traces in insulin transport and their biological implications related to glucose dependence[5, 28]. Different from these methods and those commonly used by others in transport analysis, we classify transport populations based on the full trajectory rather than sub-trajectory motion. The use of longer trajectories and averaging over lag times allows for statistically significant analysis. Further, the utilization of full trajectories allows for the isolation or complex trajectory motions, namely the run-pause or Levy-like transport. Recently, Levy walk dynamics have been observed in other intracellular transport cargoes, including endosomal and neurotransmitter transport [29, 30].

3.6 Further characterization of populations

The unique traces in the turning angle analysis confirm the distinct behavior of each population which is classified by parameters from MSD analysis. Turning angles are computed at several lag times (Δ) similar to MSD for displacement (r). The distribution of turning angles at a characteristic Δ is plotted rather than the mean value to report the most likely turning angle. Comparison of π peaks to 0 and 2π peaks report the likeliness of confined (π) vs directed (0 or 2π) at the analyzed lag time. Note that the turning angles at 0 and 2π are equivalent in polar coordinates. Turning angles near π are characteristic of confined motion as confined particles turn sharply away physical or energetic barriers that restrict a particle's motion [14, 25].

Sharp peaks at π are dominant in the immobile (Figure 3.4a), nearly immobile (Figure 3.4b), and subdiffusive (Figure 3.4e), although the behavior of the distribution of turning angles are unique at changing lag time. Turning angles near 0 and 2π are characteristic of directed motion and

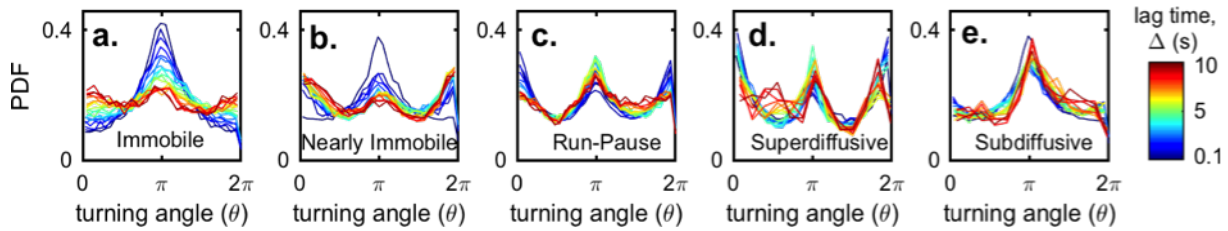

Figure 3.4: **Unique Angle Signatures.**Immobile motion (a) is dominated by confined motion at short lag times that relaxes to isotropic turning angles at longer lag times. Nearly immobile motion (b) is similar to immobile angle PDF at short lag times but the overall persistent motion is resolved at long lag times with 0 and 2π peaks. Run-Pause motion (c) is invariant through all measured lag time scales with sharp π as well as 0 and 2π peaks. Superdiffusive motion (d) is mostly dominated by persistent motion with strong 0 and 2π peaks at short lag time that somewhat relaxes at longer lag times. Subdiffusive motion (e) is consistently confined with a strong π peak at all lag time scales evaluated.

these traces are dominant in run-pause (Figure 3.4c) and superdiffusive (Figure 3.4d) populations. Notably, the magnitude of the π peak compared to the 0 and 2π peaks are similar because of the comparable contribution of run and pause components.

The evolving distribution of turning angles as a function of lag time highlights the unique characteristics of each transport population. Power-law type transport such as superdiffusive and subdiffusive transport show unchanging distributions of turning angles over different lag times because of the self-similar nature of the transport. For immobile transport and nearly immobile transport, the short lag time behaviors are comparable and exhibit at sharp π peak. At long lag times, the turning angle distribution of the immobile population relaxes to isotropic turning angles shown by the uniform distribution because the granules show little to no overall displacement. These lag-time dependent distribution traces coupled with the magnitude of the confined and directed peaks further highlight the unique transport characteristics of each population beyond their MSD scaling.

A corollary to the directional turning angle distribution is the distance analysis from the step size distribution. Anomalous, yet Brownian motion has been observed in many biological systems with Brownian α scaling in MSD with non-Gaussian step size distributions [26]. Furthermore, the non-Gaussian step distributions follow a scaling with exponential, tails proportional to $\Delta \sim 0.5$. Evidence of this lag time dependent scaling goes beyond Brownian systems. Experimental obser-

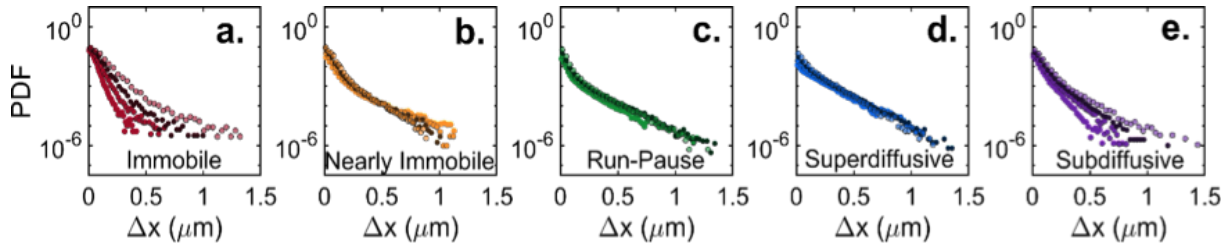

Figure 3.5: **Scaling Collapse of Step Size Probability.** Displacement probability from several hundreds of trajectories separated into populations based on MSD: (a) immobile, (b) nearly immobile, (c) run-pause, (d) superdiffusive, and (e) subdiffusive. The displacement, or step size, probability is calculated for 4 lag times (Δ = 0.1 s, 0.5 s, 1.0 s, 2.0 s) and plotted as P(x,Δ) / $\Delta^{1/2}$. This master curve that is obtained from normalizing by $\Delta^{1/2}$ is observed in (b-d). All distributions are exponential decays in the tails at long step distance in the semi-log plots.

vation in an anomalously diffusing system with motion $\alpha < 1$ in a crowded environment suggests a broader range of transport cases described by this phenomenon [31]. Broadly, observation of a scaling collapse suggests that the ensemble is undergoing the same transport mechanism because the distribution is averaged over all trajectories in the ensemble and averaged over all time step samples within a given trajectory. The convergence at different time lags implies that the motion analyzed is self-similar at different time scales.

Shown in this heterogeneous MIN6 system, this step distribution scaling holds for several transport populations in Figure 3.5 b-d. We interpret this scaling collapse as evidence that the ensembles analyzed are undergoing the same type of self-similar motion given the convergence of the distributions after sampling over all over trajectories and time. Conversely, the subdiffusive population Figure 3.5e is likely a mixture of several subdiffusive mechanisms given the lack of convergence. Notably the step probability of the immobile population in Figure 3.5a was identical for every lag time before applying a scaling correction. The displacement in the immobile population is comparable, or smaller, than the pixel size of the camera. This lack of resolution is not sufficient to show the true step distribution which could follow the scaling relationship at finer Δx step sizes.

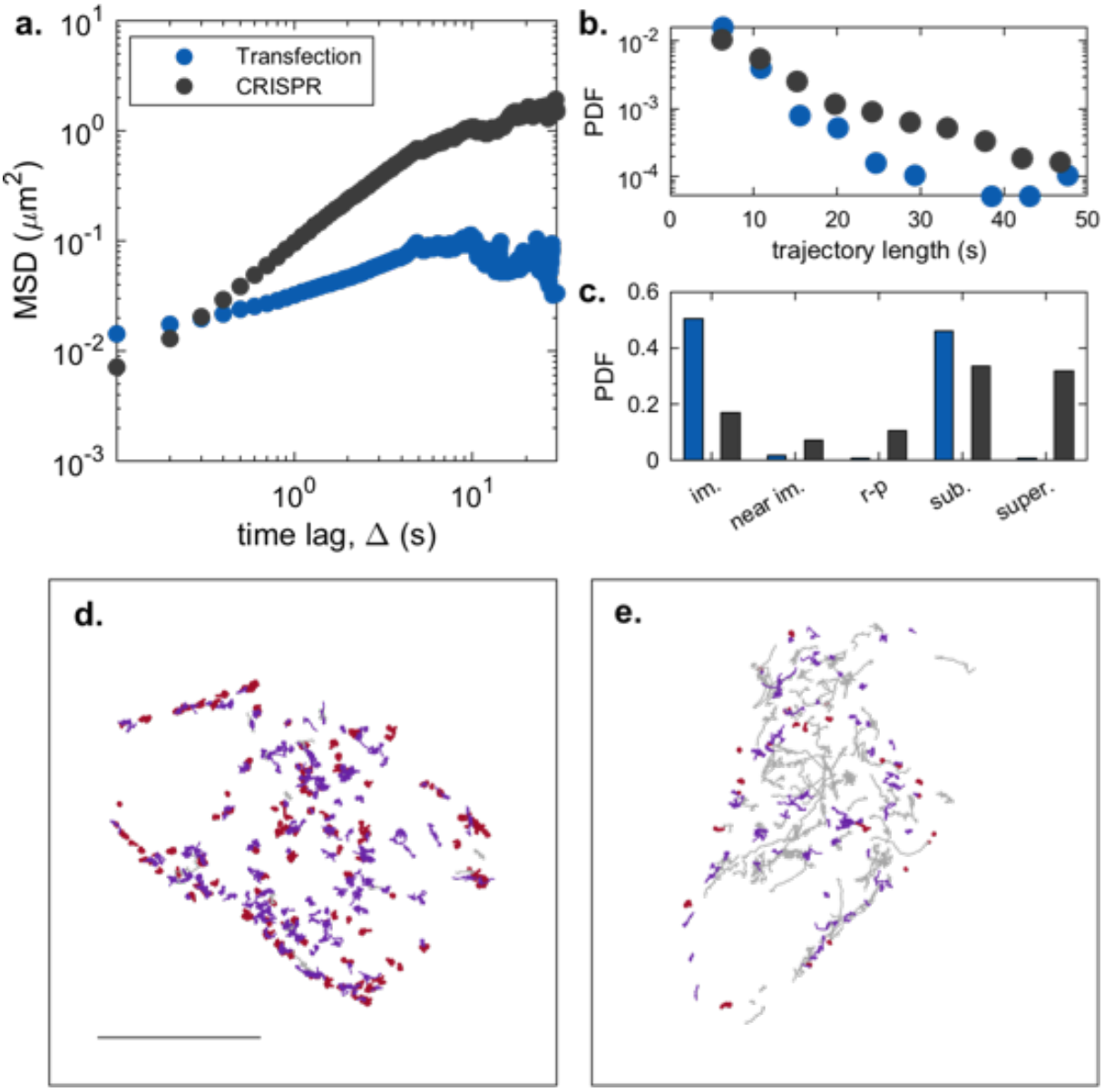

Figure 3.6: **Age-Dependent Transport Populations.** Cells transfected and incubated for 24h (a, blue) are considerably more subdiffusive than constitutively labeled cells with CRISPR (a, gray) through EA-MSD analysis. The trajectory length distributions (b) are consistent for both trials to eliminate trajectory length biases. Constitutive labeling by CRISPR-cas9 observed all transport populations while transfection labeling favors immobile and subdiffusive populations (c). The results are visualized for a transfection-labeled 2-cell cluster (d) and a CPISPR-labeled 2-cell cluster (e). Scale: 10 μm

3.7 Age-dependence on granule dynamics

The transport populations are further distinguished by their age dependence through comparison of selectively labeled 'young' granules by transient transfection to the complete ensemble of granules from the CRISPR line in MIN6 cells. In transiently transfected cells, the age of fluorescently labeled granules is bounded to the time when the fluorescent protein construct is added. The 'age' of a fluorescent protein expressing granule from transfection ranges from brand new to the time since construct addition. We choose the 24 h mark for imaging transfection labeled granules because it is comparable to the estimated half-life of insulin granules (~22-30 h) [32, 33]. From the ensemble analysis, transiently labeled insulin granules show strong subdiffusive character compared to constitutively labeled insulin granules via CRISPR (Figure 3.6a).

Several biological and sampling factors influence the observed intracellular transport of secretory vesicles. Increasing cell cluster size and cluster dimensionality enhance cell-to-cell contact which increases gap junctions and cooperatively among cells and influence subsequent secretion dynamics [34, 35]. Our study is limited to 2-cell clusters grown in monolayers to mitigate potential cluster-size influence on transport. Cell-to-cell heterogeneity is a critical influence on biological function and variability. Previous experiments implying significant heterogeneity in the wild-type MIN6 population at modest passage number motivated subline single sorting into homogeneous MIN6 sublines [36]. The same subline is used for both labeling schemes to conserve phenotypic homogeneity and the underlying granule transport. The range of granule trajectory lengths is much smaller in transient transfection trajectories than that of constitutive trajectories; their average trajectory length being 11.8s and 16.6s, respectively. To remove potential biases from trajectory length dependence on transport, only CRISPR-labeled trajectories with a comparable length distribution to transfection-labeled trajectories were used for analysis (5-50 s trajectories) (Figure 3.6b).

Transport in transiently transfected cells is dominated by immobile and subdiffusive motion (Figure 3.6c). Thus, young granules (>24h old) are overwhelmingly dominated by confined trans-

port mechanisms. The same measurement and trajectory sampling for constitutively labeled cells, which captures transport of granules of all ages, samples all populations. Our result of age dependence in granules aligns with other reports other secretory vesicles [7]. Newly developed granules are shown to have priority mobilization and secretion in first-phase release from glucose stimulation [28]. Actin facilitates the first phase of glucose stimulated insulin secretion in MIN6 cells through filamentous actin (f-actin) remodeling and assisting in t-SNARE docking of the readily releasable pool [37, 38, 38]. Priority secretion of the 'readily releasable' pool of secretory vesicles has been correlated to young vesicle age and confined motion near the plasma membrane, or 'docking', through studies using fluorescent timer proteins[7, 32].

3.8 Microtubule dynamics are influenced by active actin fluctuations

We explored the influence of actin on microtubule fluctuations and subsequent insulin granule dynamics by analyzing the confined and diffusive-like fractions of insulin granules after microtubule disruption. Thin two-dimensional sectioning in the x-y plane from confocal measurement minimizes phototoxicity and background, yet limits the z-axis information from the cell. As a result, live-cell confocal measurements probe actin rich or poor cytoskeletal environments depending the focal plane relative to the coverslip. Data acquisition of an imaging plane near the bottom on the cell captures an actin and microtubule dense region while that of an imaging plane in the middle of the cell is primarily microtubule rich with residual actin at the cortex.

Treatment with nocodazole causes tubulin monomers to depolymerize from microtubule structures, and this phenomenon is used therapeutically to inhibit mitosis of cancerous cells. At critical doping, nocodazole-mediated tubulin monomers reorganize to dense crystalline bundles termed paracrystals [39]. At mild doping conditions comparable to conditions used in this experiment, microtubules bundle into clusters without ordered packing. We labelled microtubules to monitor the microtubule depolymerization and subsequent clustering to confirm the grouping of microtubules. After comparison to literature images, we conclude that the structures are not paracrystals. Mi-

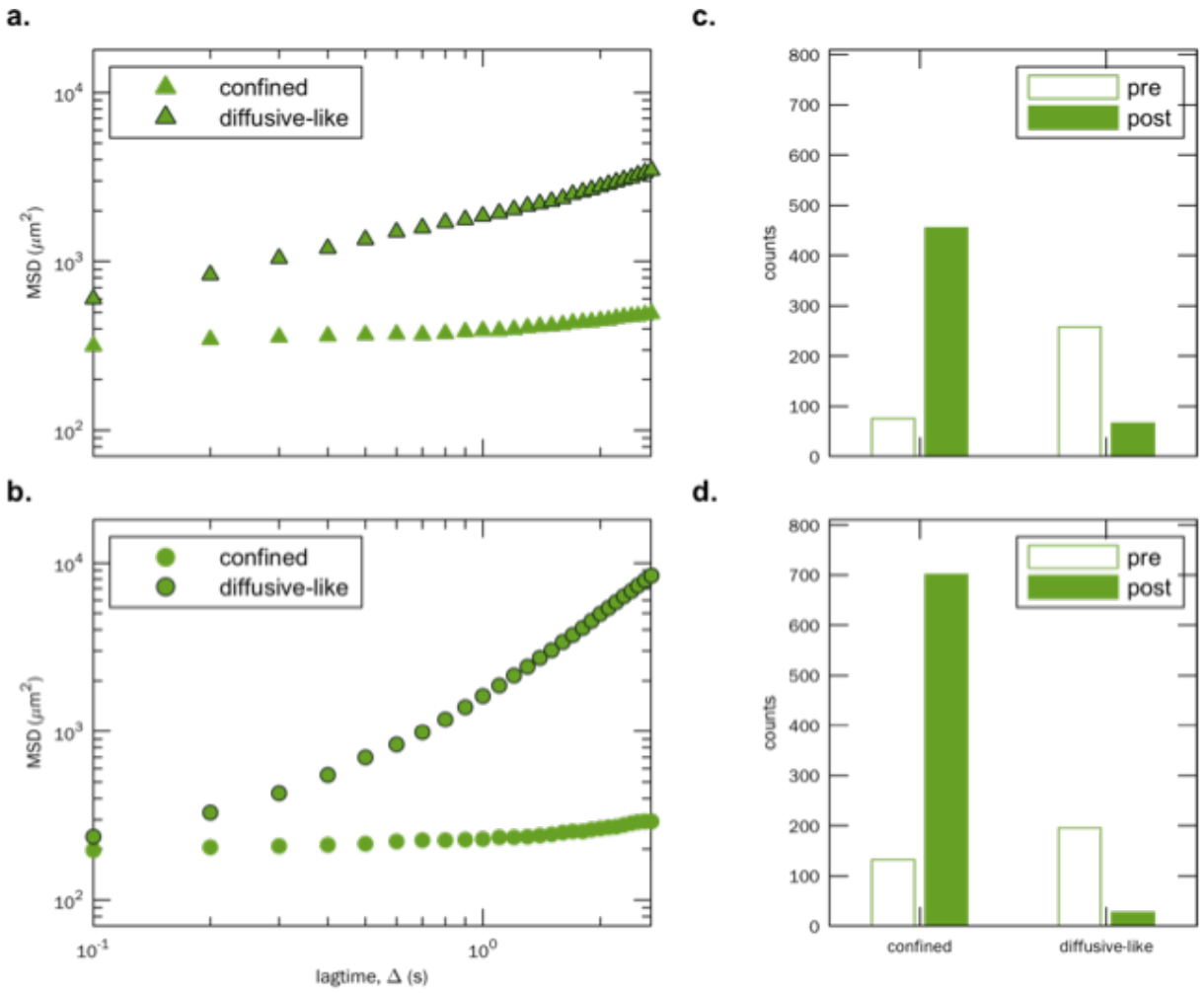

Figure 3.7: **Modulation of microtubule dynamics by fluctuations in the actin network.** EA-MSDs for post-stimulation dynamics of the two groups is analyzed for (a) middle imaging plane and (b) bottom imaging plane. Granule dynamics after microtubule disruption is analyzed by separating the two broad groups: confined movement (immobile and nearly immobile) and diffusive-like movement (run-pause, superdiffusive, and subdiffusive). The number of granules of each group is counted before stimulation (open bars) and after stimulation (solid bars) for the (c) middle and (d) bottom imaging planes.

crotubule clusters near the actin rich environments is influenced by the inherently active medium. Tracking insulin granules in this preparation acts as a second-hand reporter of microtubule cluster dynamics as the insulin granule targets are associated to the microtubule cluster through the kinesin motors. Separation of insulin trajectories based on transport characteristics allows for separation of granule fractions based on cytoskeletal association.

'Confined' and 'diffusive-like' classifications were grouped based on the five transport populations. The confined fraction is the immobile and nearly immobile populations, which the diffusive-like fraction includes the run-pause, subdiffusive, and superdiffusive classes. This simplified classification allows for better comparison in dynamics. The confined fraction contains granules that are primarily actin embedded, docked, or immobilized in other mechanisms and the insulin transport is comparable in the microtubule dominated middle imaging plane (Figure 3.7a) and actin influenced bottom imaging plane (Figure 3.7b). Conversely, actin facilitated fluctuations influence insulin transport of the diffusive-like fraction of the bottom-imaging plane (Figure 3.7b) at longer lag times, despite comparable α scaling at shorter lag times as the middle imaging plane (Figure 3.6a).

The enhanced transport from the higher α at long lag times in the actin rich environment suggests that actin promotes fluctuations of the microtubules and their associated insulin granules. The same trend is seen in the insulin transport control measurements (SI), as the actin rich bottom imaging plane (open circles) displays a higher α scaling compared to the actin deficient middle imaging plane (open triangles). Microtubule filaments are embedded in the actin network in actin rich environments, wherein the actin acts as a porous gel for the microtubule filaments at this size scale [4]. The relatively small flexural rigidity in actin filaments ($\sim 7x10^{-23} nm^2$) [40] coupled with the overwhelmingly larger kicking force at actin-associated myosin motors ($\sim 5pN$) [41] contribute to the highly dynamic nature of the actin network. Further complex mechanisms such as actin bundling and multi-headed motor dynamics also contribute to the active nature of actin [42, 43]. Fluctuations in the microtubule filaments in this actin regime are dominated by the influence of

actin to promote active transport dynamics.

The imaging plane study and actin disruption study show contradicting influences of actin on microtubule and insulin dynamics. In Figure 3.7, actin rich regions (open circles) show enhanced insulin transport compared to actin deficient regions (open triangles). Yet, when comparing the actin rich region before (open circles) to after (closed circles) actin depolymerization, actin is implied to inhibit transport. The differing transport influence could be due to the competing contributions of the acto-myosin network that can both act as an actively fluctuating medium as well as a gel-like mesh material.

3.9 Actin contributes to axial transport biases as an active medium to enhance transport near the membrane

The actin network is an active mesh material that introduces spatial heterogeneity in the cell. This manifests in imaging as an axial bias in actin contribution, where imaging planes closer to the coverslip afford an increasing density of actin. Granule transport in the actin rich imaging plane (near the cover glass) becomes more superdiffusive after dissolution of the network using Cytochalasin D (Figure 3.8a, circles) indicated by the increase slope, or α, in the red circles. In contrast, transport in the middle imaging plane with minimal actin density remains unchanged after actin disruption (Figure 3.8a, triangles), thus implying that actin network suppresses granule transport.

Looking into the constituent populations that were averaged together in Figure 3.8a, the main contributor to the enhanced transport after removing the actin network is from the enhanced nature of the populations. The relative population fractions suggest that the removal of actin should inhibit movement because the relative fraction of the subdiffusive population after actin disruption is significantly increased while the corresponding fraction of superdiffusive population is decreased (Figure 3.8b). A common hypothesis is that actin acts as an active medium, through the contractile modulations caused by myosin motors, and consequently moves the microtubule filaments that are carrying vesicles. While this phenomenon is proven to influence microtubule fluctuations,

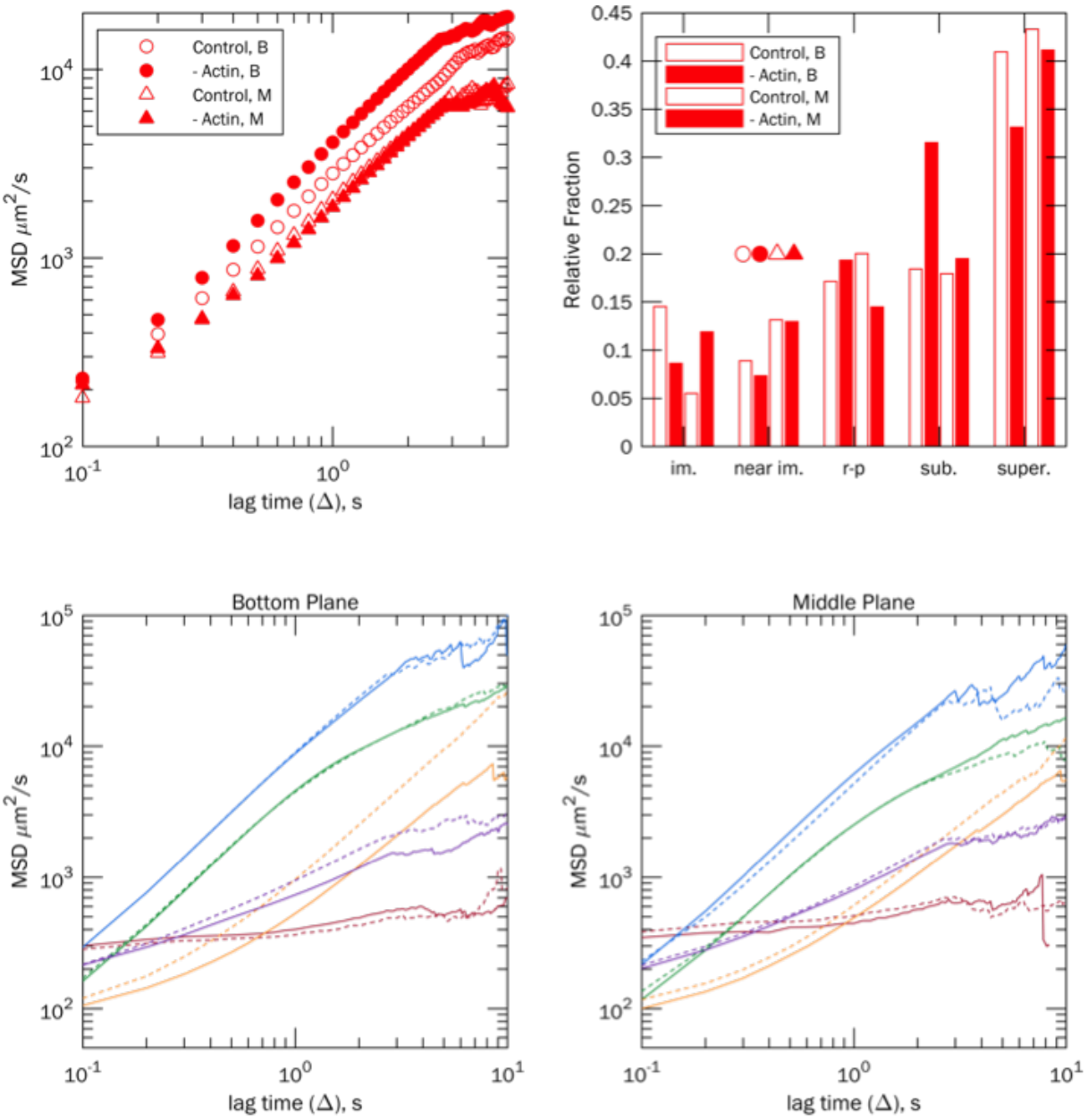

Figure 3.8: **Actin influence granule transport.**(a) Using the actin disruption drug Cytochalasin D, the resulting transport of insulin is measured at the bottom of the cell (circles) and the middle of the cell (triangles). After drug addition, no change is observed in the middle (closed triangle) but a shift to more superdiffusive behavior is observed in the bottom of the cell (closed circle). (b) Relative fraction of each population (c) EA-MSD for each population before (solid) and after (dashed) drug addition at the actin rich bottom imaging plane (d) EA-MSD for each population before (solid) and after (dashed) drug addition at the actin deficient middle imaging plane.

this contradicts the behavior seen in Figure 3.8a. Comparing the EA-MSDs of each population before and after actin treatment, the post-treatment enhancement is seen in the nearly immobile and subdiffusive populations (Figure 3.8c). Similar to the results in Figure 3.8a, the dynamics observed before and after actin treatment are unchanged in the middle imaging plane (Figure 3.8d).

3.10 Discussion and Conclusion

Intracellular vesicle trafficking is a complex process with several competing factors, both extrinsic and intrinsic, that influence transport. Such factors lead to highly varied transport characteristics ranging from confined to driven motion of cargo. We present a multi-scale lag time approach to systematically and uniformly analyze a diverse range of trajectories. The application of this method towards studying insulin granule trafficking shows that there are populations of granules that are classified by their motion. These unique populations are further distinguished by age and interaction to the cytoskeletal environment.

We demonstrate the multi-faceted role of actin, both as a mesh medium and as an active medium, in intracellular dynamics of insulin transport. Actin-mediated granule docking has been implicated as a major event in first phase insulin secretion. Thus, actin dynamics are important for understanding insulin trafficking and subsequent secretion dynamics. Recent results on the role of actin on kinesin-mediated vesicle trafficking report conflicting results on microtubule fluctuations and subsequent trafficking. Previously, transport of kinesin functionalized carbon nanotube probes suggested that actin acts as an active network that promotes fluctuations in the embedded microtubules [3]. The observation of 'freezing' of microtubule filaments after deactivation of the actin network confirm the spatial correlation between the microtubule network and actin fluctuations [44]. As a result, subsequent modulating force from actin enhances transverse 'stirring' in kinesin-based transport. More recently, a similar study used functionalized quantum dots to mitigate potential transport artifacts from the spatial anisotropy and large size of nanotubes.

Our measurement of transport directly measures a native structure for kinesin-based transport

by labeling secretory vesicles. For reference, insulin granules are ~300 nm in diameter, about 10 times larger than that of a typical quantum dot and comparable to the length of nanotubes used in the mentioned. Much conflict in the controversial role of actin lies in the length scale of the measured probe and actin configuration. While the influence of myosin motors creates active forces in actin, filamentous actin found intracellularly is a dense mesh-like material which can also contribute to viscous forces that hinder movement of targets embedded. Importantly, the influence of actin depends on the comparatively length scales of the probe and the actin pore size to determine whether the probe is embedded or mostly unaware of actin. We show that under steady-state conditions, actin acts as a hindrance to transport at the time and size scale of vesicle cargo transport.

In addition to extrinsic environmental contributors, intrinsic factors namely vesicle age largely determines a vesicle's movement. Older granules are more likely to transport actively while younger granules are more stationary. The functional implications of different transport populations, and thereby maturity level, provide fascinating insight in the priority of eventual secretion dynamics. Functional 'pools' of insulin granules have long been hypothesized based on the characteristic biphasic stimulated secretion response. The first phase of insulin secretion is attributed to a 'readily releasable' pools of insulin granules that are primed and docked near at the plasma membrane. The consequent transport trace aligns with the immobilized transport population observed in this study that is shown to be young compared to the more dynamic granules. Not only does granule age affect the transport characteristics, but it also is a determining factor in the prioritization of newly synthesized granules as readily secreted.

REFERENCES

[1] Gernot Guigas and Matthias Weiss. Sampling the cell with anomalous diffusion—the discovery of slowness. *Biophysical journal*, 94(1):90–94, 2008.

[2] Daniel S Banks and Cécile Fradin. Anomalous diffusion of proteins due to molecular crowding. *Biophysical journal*, 89(5):2960–2971, 2005.

[3] Nikta Fakhri, Alok D Wessel, Charlotte Willms, Matteo Pasquali, Dieter R Klopfenstein, Frederick C MacKintosh, and Christoph F Schmidt. High-resolution mapping of intracellular fluctuations using carbon nanotubes. *Science*, 344(6187):1031–1035, 2014.

[4] Eugene A Katrukha, Marina Mikhaylova, Hugo X van Brakel, Paul M van Bergen En Henegouwen, Anna Akhmanova, Casper C Hoogenraad, and Lukas C Kapitein. Probing cytoskeletal modulation of passive and active intracellular dynamics using nanobody-functionalized quantum dots. *Nature communications*, 8(1):1–8, 2017.

[5] Aoife T Heaslip, Shane R Nelson, Andrew T Lombardo, Samantha Beck Previs, Jessica Armstrong, and David M Warshaw. Cytoskeletal dependence of insulin granule movement dynamics in ins-1 beta-cells in response to glucose. *PloS one*, 9(10):e109082, 2014.

[6] Mingming Hao, Xia Li, Mark A Rizzo, Jonathan V Rocheleau, Benoit M Dawant, and David W Piston. Regulation of two insulin granule populations within the reserve pool by distinct calcium sources. *Journal of cell science*, 118(24):5873–5884, 2005.

[7] Rory R Duncan, Jennifer Greaves, Ulrich K Wiegand, Ioulia Matskevich, Georg Bodammer, David K Apps, Michael J Shipston, and Robert H Chow. Functional and spatial segregation of secretory vesicle pools according to vesicle age. *Nature*, 422(6928):176–180, 2003.

[8] D Zenisek, JA Steyer, and W Almers. Transport, capture and exocytosis of single synaptic vesicles at active zones. *Nature*, 406(6798):849–854, 2000.

[9] Jean-Claude Henquin, Nobuyoshi Ishiyama, Myriam Nenquin, Magalie A Ravier, and Jean-Christophe Jonas. Signals and pools underlying biphasic insulin secretion. *Diabetes*, 51(suppl_1):S60–S67, 2002.

[10] Eleni Georgiadou and Guy A Rutter. Age matters: Grading granule secretion in beta cells. *Journal of Biological Chemistry*, 295(27):8912–8913, 2020.

[11] Maayan Levin, Golan Bel, and Yael Roichman. Measurements and characterization of the dynamics of tracer particles in an actin network. *The Journal of Chemical Physics*, 154(14):144901, 2021.

[12] Ralf Metzler and Joseph Klafter. The random walk's guide to anomalous diffusion: a fractional dynamics approach. *Physics reports*, 339(1):1–77, 2000.

[13] SM Ali Tabei, Stanislav Burov, Hee Y Kim, Andrey Kuznetsov, Toan Huynh, Justin Jureller, Louis H Philipson, Aaron R Dinner, and Norbert F Scherer. Intracellular transport of insulin granules is a subordinated random walk. *Proceedings of the National Academy of Sciences*, 110(13):4911–4916, 2013.

[14] Monika Scholz, Stanislav Burov, Kimberly L Weirich, Björn J Scholz, SM Ali Tabei, Margaret L Gardel, and Aaron R Dinner. Cycling state that can lead to glassy dynamics in intracellular transport. *Physical Review X*, 6(1):011037, 2016.

[15] Adam G Hendricks, Eran Perlson, Jennifer L Ross, Harry W Schroeder III, Mariko Tokito, and Erika LF Holzbaur. Motor coordination via a tug-of-war mechanism drives bidirectional vesicle transport. *Current Biology*, 20(8):697–702, 2010.

[16] Denis Wirtz et al. Particle-tracking microrheology of living cells: principles and applications. *Annual review of biophysics*, 38(1):301–326, 2009.

[17] Jay M Newby, Alison M Schaefer, Phoebe T Lee, M Gregory Forest, and Samuel K Lai. Convolutional neural networks automate detection for tracking of submicron-scale particles in 2d and 3d. *Proceedings of the National Academy of Sciences*, 115(36):9026–9031, 2018.

[18] John C Crocker and David G Grier. Methods of digital video microscopy for colloidal studies. *Journal of colloid and interface science*, 179(1):298–310, 1996.

[19] Patrick D Hsu, Eric S Lander, and Feng Zhang. Development and applications of crispr-cas9 for genome engineering. *Cell*, 157(6):1262–1278, 2014.

[20] Sindhu Rajan, Stefani C Eames, Soo-Young Park, Christine Labno, Graeme I Bell, Victoria E Prince, and Louis H Philipson. In vitro processing and secretion of mutant insulin proteins that cause permanent neonatal diabetes. *American Journal of Physiology-Endocrinology and Metabolism*, 298(3):E403–E410, 2010.

[21] Aristea E POULI, Evaggelia EMMANOUILIDOU, Chao ZHAO, Christina WASMEIER, John C HUTTON, and Guy A RUTTER. Secretory-granule dynamics visualized in vivo with a phogrin–green fluorescent protein chimaera. *Biochemical Journal*, 333(1):193–199, 1998.

[22] Simon Watkins, Xuehui Geng, Lehong Li, Glenn Papworth, Paul D Robbins, and Peter Drain. Imaging secretory vesicles by fluorescent protein insertion in propeptide rather than mature secreted peptide. *Traffic*, 3(7):461–471, 2002.

[23] Michael Weiss, Donald F Steiner, and Louis H Philipson. Insulin biosynthesis, secretion, structure, and structure-activity relationships. 2015.

[24] Gina LC Yosten and Grant R Kolar. The physiology of proinsulin c-peptide: unanswered questions and a proposed model. *Physiology*, 30(4):327–332, 2015.

[25] Stanislav Burov, SM Ali Tabei, Toan Huynh, Michael P Murrell, Louis H Philipson, Stuart A Rice, Margaret L Gardel, Norbert F Scherer, and Aaron R Dinner. Distribution of directional change as a signature of complex dynamics. *Proceedings of the National Academy of Sciences*, 110(49):19689–19694, 2013.

[26] Bo Wang, Stephen M Anthony, Sung Chul Bae, and Steve Granick. Anomalous yet brownian. *Proceedings of the National Academy of Sciences*, 106(36):15160–15164, 2009.

[27] David Ando, Nickolay Korabel, Kerwyn Casey Huang, and Ajay Gopinathan. Cytoskeletal network morphology regulates intracellular transport dynamics. *Biophysical journal*, 109(8):1574–1582, 2015.

[28] Peter Hoboth, Andreas Müller, Anna Ivanova, Hassan Mziaut, Jaber Dehghany, Anke Sönmez, Martina Lachnit, Michael Meyer-Hermann, Yannis Kalaidzidis, and Michele Solimena. Aged insulin granules display reduced microtubule-dependent mobility and are disposed within actin-positive multigranular bodies. *Proceedings of the National Academy of Sciences*, 112(7):E667–E676, 2015.

[29] Kejia Chen, Bo Wang, and Steve Granick. Memoryless self-reinforcing directionality in endosomal active transport within living cells. *Nature Materials*, 14(6):589–593, 2015.

[30] Sergei Fedotov, Nickolay Korabel, Thomas A Waigh, Daniel Han, and Victoria J Allan. Memory effects and lévy walk dynamics in intracellular transport of cargoes. *Physical Review E*, 98(4):042136, 2018.

[31] Thomas J Lampo, Stella Stylianidou, Mikael P Backlund, Paul A Wiggins, and Andrew J Spakowitz. Cytoplasmic rna-protein particles exhibit non-gaussian subdiffusive behavior. *Biophysical journal*, 112(3):532–542, 2017.

[32] Anna Ivanova, Yannis Kalaidzidis, Ronald Dirkx, Mihail Sarov, Michael Gerlach, Britta Schroth-Diez, Andreas Müller, Yanmei Liu, Cordula Andree, Bernard Mulligan, et al. Age-dependent labeling and imaging of insulin secretory granules. *Diabetes*, 62(11):3687–3696, 2013.

[33] Shin-ichi Harashima, Anne Clark, Michael R Christie, and Abner Louis Notkins. The dense core transmembrane vesicle protein ia-2 is a regulator of vesicle number and insulin secretion. *Proceedings of the National Academy of Sciences*, 102(24):8704–8709, 2005.

[34] Azazul Chowdhury, Venkata P Satagopam, Levon Manukyan, Konstantin A Artemenko, Yi Man Eva Fung, Reinhard Schneider, Jonas Bergquist, and Peter Bergsten. Signaling in insulin-secreting min6 pseudoislets and monolayer cells. *Journal of proteome research*, 12(12):5954–5962, 2013.

[35] Arthur Sherman and John Rinzel. Model for synchronization of pancreatic beta-cells by gap junction coupling. *Biophysical journal*, 59(3):547–559, 1991.

[36] Kohtaro Minami, Hideki Yano, Takashi Miki, Kazuaki Nagashima, Chang-Zheng Wang, Hiroko Tanaka, Jun-Ichi Miyazaki, and Susumu Seino. Insulin secretion and differential gene expression in glucose-responsive and-unresponsive min6 sublines. *American Journal of Physiology-Endocrinology And Metabolism*, 279(4):E773–E781, 2000.

[37] Kouichi Mizuno, José S Ramalho, and Tetsuro Izumi. Exophilin8 transiently clusters insulin granules at the actin-rich cell cortex prior to exocytosis. *Molecular biology of the cell*, 22(10):1716–1726, 2011.

[38] Debbie C Thurmond, Carmen Gonelle-Gispert, Megumi Furukawa, Philippe A Halban, and Jeffrey E Pessin. Glucose-stimulated insulin secretion is coupled to the interaction of actin with the t-snare (target membrane soluble n-ethylmaleimide-sensitive factor attachment protein receptor protein) complex. *Molecular endocrinology*, 17(4):732–742, 2003.

[39] Mary Ann Jordan, Douglas Thrower, and Leslie Wilson. Effects of vinblastine, podophyllotoxin and nocodazole on mitotic spindles. implications for the role of microtubule dynamics in mitosis. *Journal of cell science*, 102(3):401–416, 1992.

[40] Frederick Gittes, Brian Mickey, Jilda Nettleton, and Jonathon Howard. Flexural rigidity of microtubules and actin filaments measured from thermal fluctuations in shape. *The Journal of cell biology*, 120(4):923–934, 1993.

[41] Jeffrey T Finer, Robert M Simmons, and James A Spudich. Single myosin molecule mechanics: piconewton forces and nanometre steps. *Nature*, 368(6467):113–119, 1994.

[42] Samantha Stam, Simon L Freedman, Shiladitya Banerjee, Kimberly L Weirich, Aaron R Dinner, and Margaret L Gardel. Filament rigidity and connectivity tune the deformation modes of active biopolymer networks. *Proceedings of the National Academy of Sciences*, 114(47):E10037–E10045, 2017.

[43] Simon L Freedman, Shiladitya Banerjee, Glen M Hocky, and Aaron R Dinner. A versatile framework for simulating the dynamic mechanical structure of cytoskeletal networks. *Biophysical journal*, 113(2):448–460, 2017.

[44] Clifford P Brangwynne, FC MacKintosh, and David A Weitz. Force fluctuations and polymerization dynamics of intracellular microtubules. *Proceedings of the National Academy of Sciences*, 104(41):16128–16133, 2007.

3.A Appendix: Supporting Information

3.A.1 Cell culture and confocal imaging

Low Passage MIN6 sublines were grown some single cells of the "wild-type" MIN6 culture kindly gifted from Dr. Louis Philipson at The University of Chicago. A MIN6 subline transduced via CRISPR-Cas9 technology to insert the mCherry gene into the C-peptide sequence. The resultant cells are cultured in high glucose DMEM (Gibco, 11965092) supplemented with 10% Serum Plus-II (MilliporeSigma, 14009C) and 200 uL/mL Penicillin/Streptavidin (Gibco, 15140122). Cells are incubated in 5.0% CO_2 at 37.5 ^oC with high humidity. Media is replaced every 2-3 days. Cell cultures are passaged at 90% confluence using Versene (Gibco, 15040066) and Trypsin (Gibco, 25200056) at manufacturer's recommended protocol.

Cells used in this study were passage 13-20. From the trypsin-ized cell mixture from cell passage, a small aliquot 100-500 μL is placed on a glass bottom imaging dish (Matek, P35G-1.5-10-C) then allowed to sit for 6 h or until the cells to adhere to the glass bottom. Cells are then fed with 2 mL of growth media and allowed to incubate overnight. Growth media is replaced with 28 mM glucose in Krebs-Ringer Buffer (KRB, 132 mM NaCl, 4.7 mM KCl, 2.5 mM $CaCl_2$, 1.2 mM $MgSO_4$, 1.2 mM KH_2PO_4, 2 mM $NaHCO_3$, pH 7.4) with 10mM HEPES. Cells are incubated for 30 min in buffer before imaging on the confocal microscope.

The microscope used for live cell imaging is an inverted microscope body (Nikon Ti), spinning disk confocal scanner (Yokogawa CSW1), 100x oil objective (Nikon, PlanApo) and EMCCD detector (iXON 888). The mCherry fluorescence is excited using a 561 nm laser diode (Spectra-Physics, Excelsior One) and emission is filtered at 610 nm (Chroma). Cells are maintained at 37 ^oC using a home-built microscope camber and heating element. Meanwhile, CO_2 is buffered from the HEPES reagent in the imaging solution. Total time for imaging sessions is under 30 min, which is an empirical guideline such that the HEPES regent is not used up.

Microscopy image stacks are recorded at 10 Hz frame rate for 2000 frames; a total image

acquisition time of 200 s. Imaging sessions are <30 min per sample and multiple image stacks are recorded per sample. Image stacks are saved as unsigned 16-bit TIFF files and subsequently analyzed using ImageJ and MATLAB.

3.A.2 Single Particle Tracking and Trajectory Curation

Single particle tracking is carried out in two steps: particle localization and trajectory linking. The 'raw' trajectory list is obtained from the MOSAIC plug-in from ImageJ[1] which allows for quick parameter adjustment (radius, cutoff, percent) and subsequent image verification. The percent allowed parameter is chosen to accept more false positives, such that the number of false negatives is minimized. The particle localizations at the given radius size has a small particle localization bias towards the center of the 'metapixel'. The SPIFF algorithm is used to remove the localization bias from the XY coordinates [2, 3].

Large groupings of particles are observed in addition to the singular granules. Two particle radii are used for particle localization to capture the singular particles (5 px radius) and large clusters (15 px radius). Singular particle localizations with coincident time frame and position as the large cluster localizations are removed from the singular granules list. The list of singular granules containing X position, Y position, and time frame is then linked into trajectory lists containing X position, Y position, time frame, and trajectory ID. The Crocker-Grier linking algorithm is used which minimizes the distance traveled between all the particles in two consecutive frames[4].

False positive and false negatives from particle tracking are assumed to be present within the trajectory list. The presence of false positives is large since the particle localization parameters are chosen to minimize the number of false negatives. The resultant trajectories for false positives are short in time length (>5 time frames). Trajectories that are shorter than 15 time frames are removed from the trajectory list.

We considered two sampling methods of a trajectory for a given lag time. Lag time sampling of trajectory data for calculating MSD is assumed to be uncorrelated for a stochastic process where

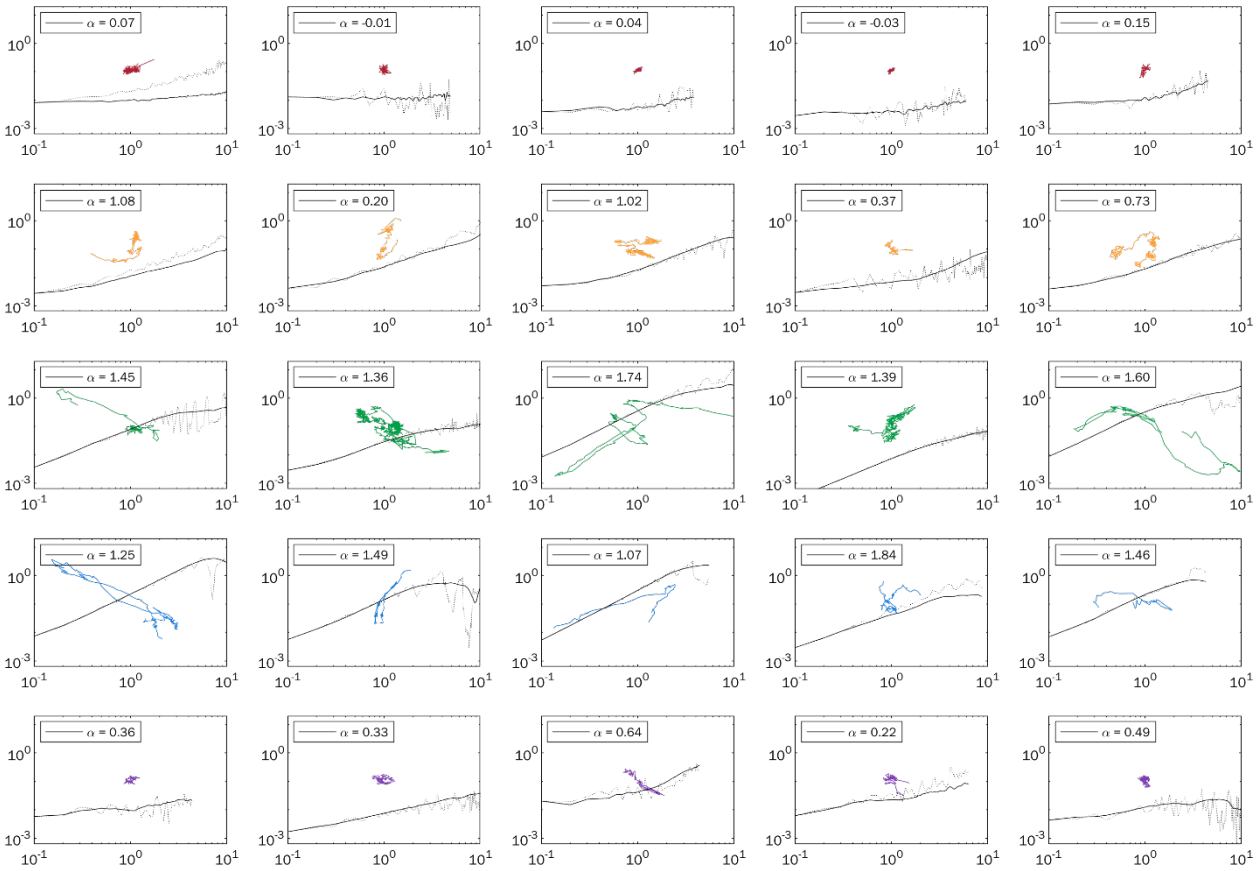

Figure 3.9: **Gallery of Single Trajectories and MSD by Population.** Sample single trajectories separated by population and color coded. Each row is a different population: immobile (top), nearly immobile, run-pause, superdiffusive, subdiffusive (bottom). The TA-MSD is calculated for every trajectory using the traditional sliding sampling (solid black line) and non-overlapping sampling (dotted black line). Axes shown correspond to the MSD scale and the field of view for the trajectories for the same plot box is 3.6 μm x 3.6 μm (axes not shown).

successive steps are random. Yet, highly correlated motion would exhibit biased sampling using an overlapping lag time sampling, or sliding window, approach. While the non-overlapping sampling ensures random and uncorrelated sampling, the statistics are severely worse than the conventional sliding window approach. Both overlapping sampling (solid line) and non-overlapping sampling (dotted line) for lag times was calculated and plotted for several trajectories in each population in Figure 3.9. We concluded that time correlation is not a major bias in MSD calculation and used the overlapping sampling approach for this study.

3.A.3 Turning Angle Analysis

The turning angle from two consecutive vectors in a trajectory is calculated using an approach adapted from Burov et al.[5]. The two vectors for analysis are obtained from a trajectory by coarse-graining or subsampling by the analyzed lag time Δ, so that the three positions analyzed are spaced in time by Δ time steps. The turning angle is analyzed as a sliding analysis to evaluate the whole trajectory. The distribution of turning angles is plotted as a probability density function, $P(\theta, \Delta)$, for a given lag time.

Turning angles are calculated from the arctangent to achieve a $[0, 2\pi]$ range. Conveniently, the relationship between two vectors and their relative angle are given from the cross product and dot product:

$$\vec{v}_t \times \vec{v}_{t+\Delta} = |\vec{v}_t||\vec{v}_{t+\Delta}|sin\theta \tag{3.1}$$

$$\vec{v}_t \cdot \vec{v}_{t+\Delta} = |\vec{v}_t||\vec{v}_{t+\Delta}|cos\theta \tag{3.2}$$

However, the angle calculated from one of these relationships is only in the $[0\ \pi]$ range. Therefore, we used these expressions for $sin(\theta)$ and $cos(\theta)$ to find $tan(\theta)$.

$$tan(\theta) = \frac{sin(\theta)}{cos(\theta)} = \frac{\vec{v}_t \times \vec{v}_{t+\Delta}}{\vec{v}_t \cdot \vec{v}_{t+\Delta}}$$

$$\theta = tan^{-1}\left(\frac{\vec{v}_t \times \vec{v}_{t+\Delta}}{\vec{v}_t \cdot \vec{v}_{t+\Delta}}\right) \tag{3.3}$$

3.A.4 Ageing

We check whether ageing, a characteristic of glassy systems, occurs in the populations and find weak effects in all modes of transport (Figure 3.10). Ageing is an intrinsic property to transport and is different from the granule age, or "Age-Dependence" discussed in Figure 3.6. Ageing effects

manifest as a progressive slowing down of the dynamics at increasing measurement or observation time. The continuous-time random walk model is used ubiquitously in intracellular transport for dynamics that observe ageing, wherein single particle targets interact with 'traps' that impede movement. We rationalize the collective ageing effects are from the interaction of insulin granules with the crowded intracellular environment. Particularly, cytoskeletal scaffolds with pore mesh sizes comparable to the granule or vesicle size leads to crowding effects of the microtubule network against the moving granules.

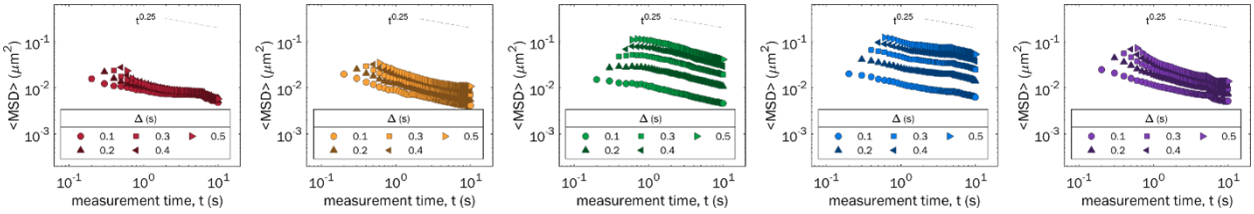

Figure 3.10: **Ageing for Transport Populations.** Weak ageing is observed in all populations: immobile (left), nearly immobile, run-pause, superdiffusive, and subdiffusive (right).

3.A.5 Transport Anisotropy in Axial Plane

The density and composition of the cytoskeletal environment varies with the axial plane of a cell sitting on a coverslip. Imaging at the 'bottom' of the cell, near the coverslip, probes an environment that is dense in actin as well as microtubules. On the other hand, imaging towards the 'middle' of the cell is primarily microtubule rich with cortical actin near the plasma membrane perimeter of the cell. We compare the distribution of α (Fig 3.11) and Deff (Fig 3.12) for a cell cluster at the bottom (left) and middle(right) imaging plane and find that the mean of either variable shows no significant difference. Yet, there is an enhancement in the relative fraction of immobile granules in the bottom imaging plane. This increase in immobile fraction is likely attributed to the increased docking sites for granules in the bottom imaging plane.

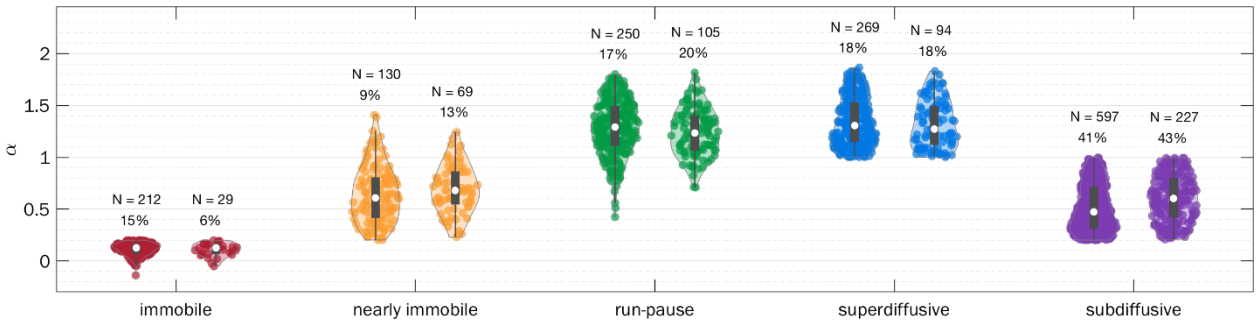

Figure 3.11: **Comparison of α distributions for 2 z-planes in the same cell cluster.** Violin plots show the distribution of α calculated from the TA-MSD. For each pair in a given population category, the left violin distribution is from the bottom of the cell (near the coverslip) and the right violin distribution is from the middle of the cell (where the nucleus radii are the greatest). The number of trajectories analyzed and the relative percent, (N/Ntotal) x 100, is shown above each violin distribution.

3.A.6 Investigating Cell-to-Cell Variability in Transport

Cell-to-cell variability is an inevitable factor influencing live cell studies. We measured the dynamics from the α parameter (Fig 3.13) and Deff (Fig 3.14) for three measurements taken on different days. For each imaging session, clusters of 2-3 cells were chosen so that clustering influences could be disregarded. We find slight variation the mean α and D_{eff} in each measurement as well as shift in the distribution density. Similarly, the relative fraction of each population is comparable across each measurement. We conclude that the populations are consistent across MIN6 cells and note that the first trial in this analysis was used for analysis in the main text.

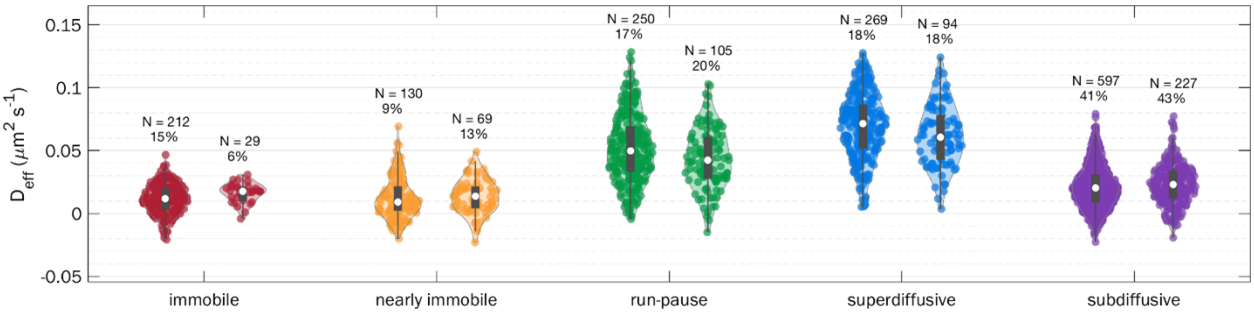

Figure 3.12: **Comparison of D_{eff} distributions for 2 z-planes in the same cell cluster.** Violin plots show the distribution of D_{eff} calculated from the TA-MSD. For each pair in a given population category, the left violin distribution is from the bottom of the cell (near the coverslip) and the right violin distribution is from the middle of the cell (where the nucleus radii are the greatest). The number of trajectories analyzed and the relative percent, (N/Ntotal) x 100, is shown above each violin distribution.

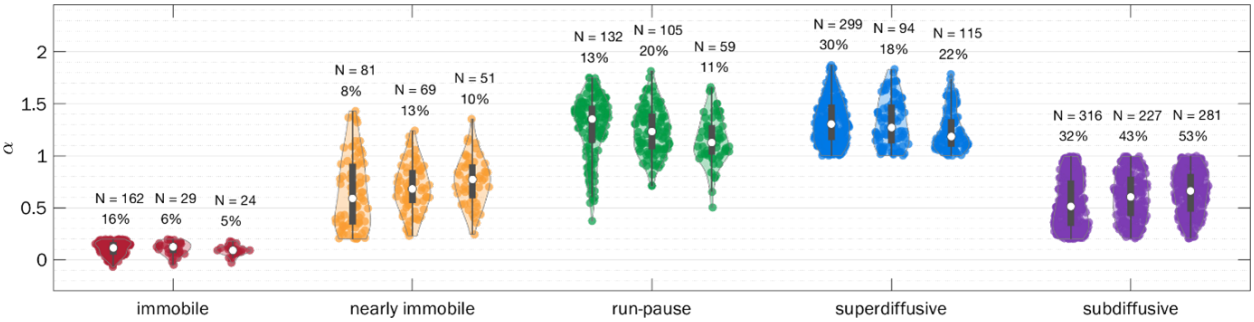

Figure 3.13: **Comparison of α distributions for 3 measurements**. Violin plots show the distribution of α calculated from the TA-MSD. The number of trajectories analyzed and the relative percent, (N/Ntotal) x 100, is shown above each violin distribution.

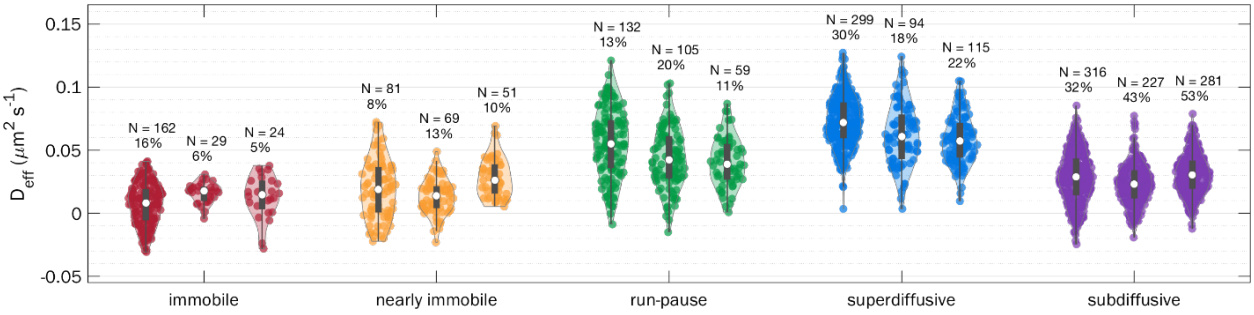

Figure 3.14: **Comparison of D_{eff} distributions for 3 measurements.** Violin plots show the distribution of D_{eff} calculated from the TA-MSD. The number of trajectories analyzed and the relative percent, (N/Ntotal) x 100, is shown above each violin distribution.

REFERENCES

[1] Ivo F Sbalzarini and Petros Koumoutsakos. Feature point tracking and trajectory analysis for video imaging in cell biology. *Journal of structural biology*, 151(2):182–195, 2005.

[2] Yuval Yifat, Nishant Sule, Yihan Lin, and Norbert F Scherer. Analysis and correction of errors in nanoscale particle tracking using the single-pixel interior filling function (spiff) algorithm. *Scientific reports*, 7(1):1–10, 2017.

[3] Stanislav Burov, Patrick Figliozzi, Binhua Lin, Stuart A Rice, Norbert F Scherer, and Aaron R Dinner. Single-pixel interior filling function approach for detecting and correcting errors in particle tracking. *Proceedings of the National Academy of Sciences*, 114(2):221–226, 2017.

[4] John C Crocker and David G Grier. Methods of digital video microscopy for colloidal studies. *Journal of colloid and interface science*, 179(1):298–310, 1996.

[5] Stanislav Burov, SM Ali Tabei, Toan Huynh, Michael P Murrell, Louis H Philipson, Stuart A Rice, Margaret L Gardel, Norbert F Scherer, and Aaron R Dinner. Distribution of directional change as a signature of complex dynamics. *Proceedings of the National Academy of Sciences*, 110(49):19689–19694, 2013.

CHAPTER 4

SCRUMS: A DYNAMIC STORAGE SYSTEM FOR INTRACELLULAR INSULIN IN A MODEL BETA-CELL LINE

4.1 Abstract

In this chapter, a novel storage mechanism is reported for the dynamic storage of insulin granules at basal conditions. The full fluorescently labeled vesicle cell line that we developed is the first demonstration of its kind for intracellular insulin. In contrast, traditional transient transfection approaches label a fraction of existing granules (insulin containing vesicles). We estimate that roughly 14% of vesicles are labeled using transfection given a 2 day window for fluorescent tag incorporation compared to the estimated 2 week lifetime of a granule [1]. The observed clusters that are prominently presented in this study are likely hidden in transfection preparations because of the fractional labeling efficiency. A custom image analysis method is developed for the study of granule interactions with the larger clusters, then the dynamics are analyzed using Poisson statistics.

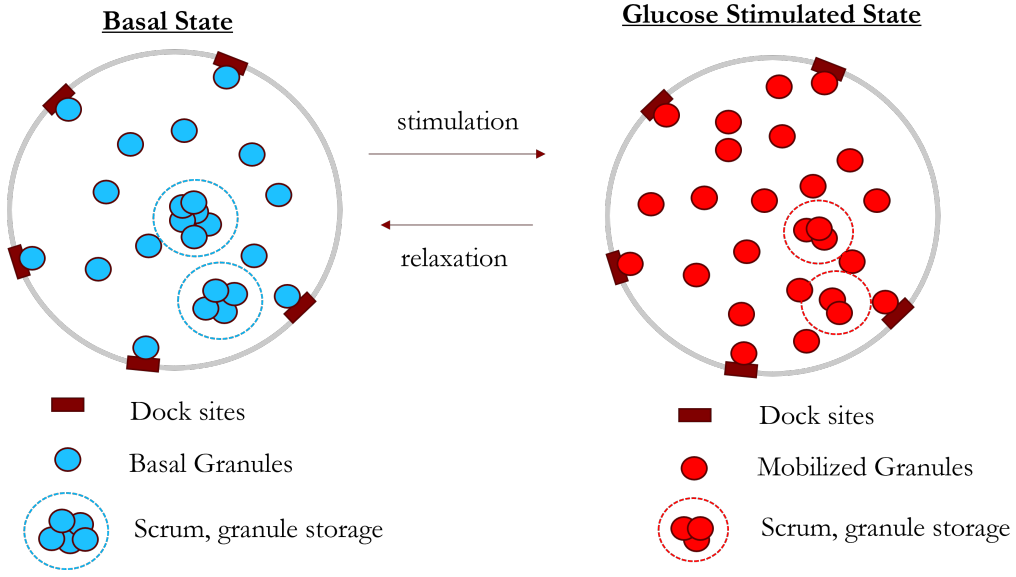

Figure 4.1: **Proposed storage mechanism for glucose stimulated insulin mobilization.**

4.2 Introduction

Intracellular insulin has long been thought of as two pools of insulin-containing vesicles (termed insulin granules) corresponding to the biphasic nature of insulin secretion. These pools are loosely defined in their physical location, but much evidence has been found on functional differences in subsets of insulin-containing vesicles [2–6]. A small subset ($\sim$ 1-5%) of secretory granules known as the readily releasable pool (RRP) are "pre-docked" for insulin secretion and contribute to the rapid first phase of insulin secretion [2, 7]. The rest of the granules compose the reserve pool (RP) and are used to recycle the readily releasable pool. A fraction of the reserve pool is secreted upon glucose stimulation and contribute to the sustained, yet slower rate of insulin secretion in the second phase [6].

Continuing research has challenged the two functional pool picture which fails to capture the heterogeneity in regulation by and sensitivity to chemical and metabolic stimuli [8–11]. Intracellular calcium, in particular, plays a multifacted role in directing subsets of granules to move faster or recruit granules to the RRP [11, 12]. Still, the mechanism for the recruitment and transport of insulin granules between the two (or more) pools remains unknown.

One reason that research on the reserve pool dynamics has been stagnant is the older biogenesis age of reserve pool granules. Shown in Chapter 3 and in other works in secretory vesicle systems [13, 14], young granules are favored for first phase secretion making them a constituent of the RRP and prime candidates for study via transient transfection labeling. The expected lifetime of old granules in the reserve pool are up to two week old [1], making them a more challenging pool to label and study.

Herein, a fully labeled β-cell line tagging insulin is used to study reserve pool dynamics at basal and glucose stimulated states. We observe a novel structure, termed scrums, that stores insulin granules at basal glucose conditions and releases them when granules are mobilized under glucose stimulation (Fig 4.1). Studying the basal glucose state after stimulation shows the reformation of scrums, indicating the reversibility of the storage.

4.3 Scrums are local accumulations of insulin granules

The fluorescent protein mCherry is fused to the C-peptide of pro-insulin in a cell culture of Mouse Insulinoma 6 (MIN6) cells using CRISPR-cas9 to create a transgenically labelled cell line. Consistent to literature designs for transient labelling [15], the fluorescent protein gene is inserted in-frame at the C-peptide gene of pro-insulin. Pro-insulin is the upstream analog comprised of insulin and the C-peptide. Upon vesicular packaging in the Golgi Apparatus, pro-insulin is cleaved to insulin and the C-peptide fused with mCherry. This approach allows for targeted labeling of insulin containing vesicles without the poor vesicle maturation that is observed in insulin fusion proteins [1]. The design and characterization of this transgenic line is discussed in a previous chapter.

Live cell imaging with fluorescent confocal microscopy reveals fluorescently labeled granules with an estimated diameter of 5-8 pixels (355-568 nm) that is consistent with the 200-500 nm diameter insulin granules (Fig 4.2a). The larger observed size is expected since the true size of the granules is smaller than the diffraction limit of the microscopy system, leading to image broadening from light diffraction. Surprisingly, larger 15-25 pixel diameter spots are observed (Fig 4.2a, yellow box). The dynamics of the spots over time suggest that these are local clusters of singular granules (Fig 4.2b). Instances of single granules leaving or entering the large spot are observed over time. We term these clusters as scrums to denote the collective contribution of individual components to create a larger unit.

The constituent composition is confirmed using super resolution microscopy to resolve individual granules in the scrum. A fixed sample of mCherry labelled cells was prepared to eliminate the dynamic movement of insulin granules. The fixed cell is imaged by confocal microscopy (Fig 4.2c) and stimulated emission depletion (STED) microscopy (Fig 4.2d) for the same field-of-view. STED microscopy achieves sub diffraction limit imaging by depleting the outer fluorescence region of an excitation point-spread function to create a smaller excitation region [16]. Under STED microscopy, the image of a scrum in conventional imaging (Fig 4.2c, inset) is resolved to individ-

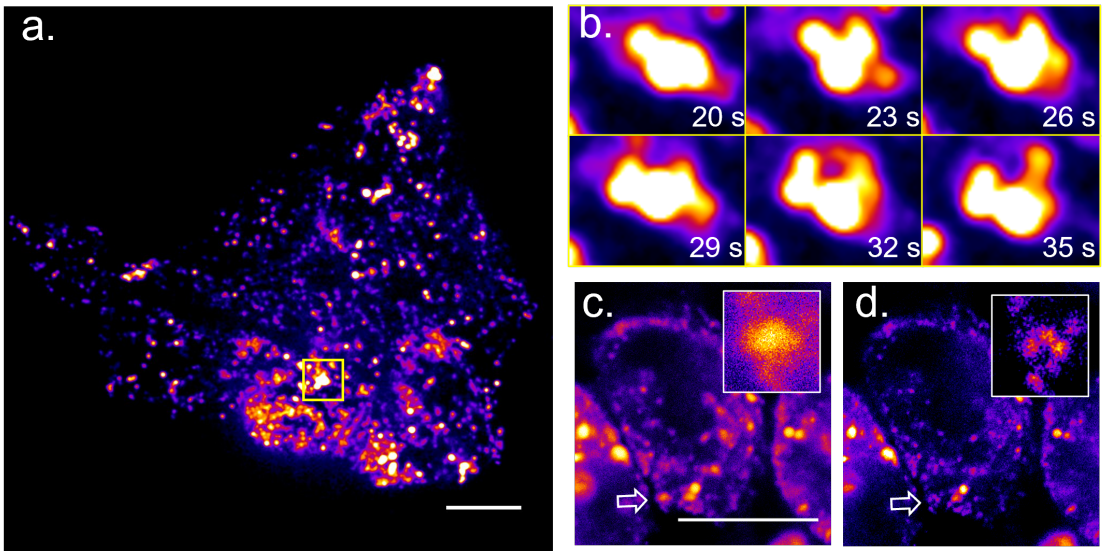

Figure 4.2: **Local clusters of insulin granule vesicles**(a) Confocal live cell image of a MIN6 cells constitutively expressing mCherry labelled insulin. Scale: 10 um. (b) Time series of a large cluster of granules, termed a scrum, from the yellow box in (a) shows the dynamic nature of the cluster. (c) Confocal image of a fixed sample of MIN6 cells with mCherry-insulin expression. Inset shows a zoom into a scrum shown by the arrow. Scale: 10 um. (d) Super-resolution image by STED microscopy of the same sample in (c) shows the resolved individual granules in a scrum. Field-of-view is the same as (c).

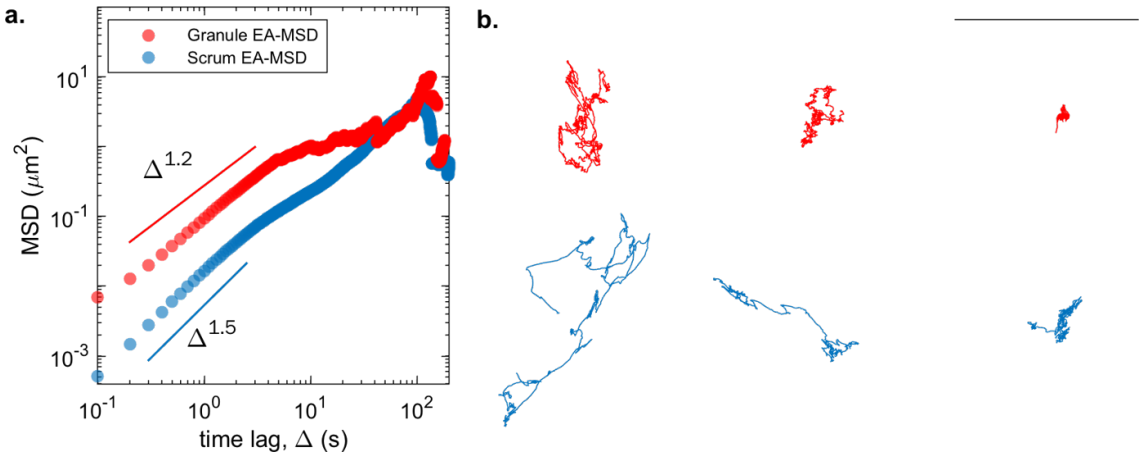

Figure 4.3: **Ensemble dynamics of scrums and singular granules.** (a) Ensemble-averaged mean squared displacement of individual granules (red) and scrums (blue). Linear fitting on the log-log scale is shown in guidelines above or below the data points and slope fitting parameter α is reported as Δ^{α}. (b) Three sample trajectories for scrums and granules that show the range of transport behavior from driven (left) to confined (right) motion. Scale bar (top right): 2 um.

ual granules through this super resolution method (Fig 4.2d, inset). This proves that the images of scrums are large spots because the individual granules are closely clustered at a distance below the diffraction limit of the confocal imaging system. The resultant large spot size of scrums is the convolution of the fluorescent signal from the closely clustered, individual granules.

Comparison of the ensemble MSD for granules and scrums show that scrums diffuse a smaller length than granules. On the the log-log plot of MSD, the power law form $\langle R(\Delta)^2 \rangle = K_\alpha \Delta^\alpha$ rearranges to $\alpha(\Delta) + log(K_\alpha)$ where K_α is the effective diffusion coefficient and the y-intercept. The shift down in the scrum ensemble MSD in Fig 4.3a at comparable α slope indicates the smaller diffusion observed in the scrum ensemble and the expected net displacement in scrums are lower than in granules. Similar to previous studies in Chapter 3, the ensemble is heterogeneous for both scrum and granules (Fig 4.3b).

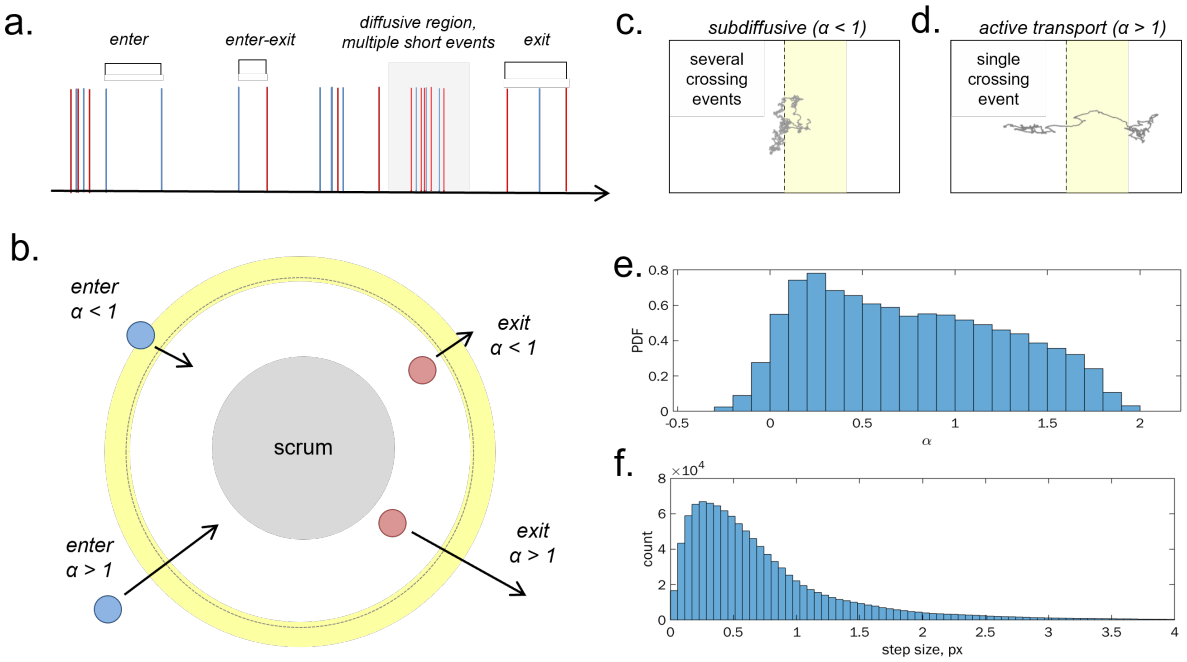

Figure 4.4: **Detecting granule flux through a scrum.**(a) Schematic of reaction coordinate showing enter (blue) and exit (red) events of granules into a scrum. Observed flux dynamics show events closely spaced in time which is highlighted in gray. The brackets demonstrate how time between events is determined for subsequent figures. (b) Diagram of image analysis approach and interpretation of observed dynamics. A detection annulus (yellow ring) starting from the inner interaction radius (dashed line) is used to identify candidate granules from the larger granule set. Scrum flux events are detected from the candidate granules that cross the fixed interaction radius. The diffusive regime of a singular granule can be confined ($\alpha < 1$) or driven ($\alpha > 1$). (c) Granules exhibiting subdiffusive motion enable several enter and exit events across the interaction radius, leading to the closely spaced events highlighted in (a). (d) Granules exhibiting active transport ($\alpha > 1$), or superdiffusive motion, manifest a single crossing event through the interaction radius. (e) The experimental distribution of all granule diffusive parameter α (N = 182,433 trajectories) show two broad peaks corresponding to the two diffusive regimes. (f) Distribution of frame-to-frame step sizes for all analyzed granule trajectories used to determine the detection annulus width (1.5 px).

4.4 Tracking flux dynamics of insulin granules in scrums

An image analysis method was developed to study the dynamics of scrum and granule interactions. Interaction events are determined when a granule crosses an interaction boundary around the scrum (Fig 4.4b) and the time and event type, enter or exit, are recorded (Fig 4.4a). Two crossing regimes are considered for their interaction with the detection boundary and the time scale of the crossing dynamics. Subdiffusive granule transport, where $\alpha < 1$, leads to short time-scale multiple crossing events from the same granule (Fig 4.11c). Superdiffusive granule trnasport ($\alpha > 1$), also called active transport, results in a single crossing event for each trajectory (Fig 4.11d). The time scale for this type of transport is longer because every recorded event comes from a different granule crossing the interaction boundary and these events are uncorrelated. The contribution of these two diffusive regimes are comparable as the distribution of granule α under basal glucose conditions is bimodal (Fig 4.4e). The sample size for the number of trajectories is large and calculating the pair distance for every scrum to every granule was simplified by only considering granules withing a narrow annulus (Fig 4.4b, yellow ring). The width of this annulus was chose to be larger than the expected step size of a granule trajectory, such that at least one step is taken within the detection annulus. The detection annulus width is 1.5 px (or 106 nm) which is larger than ¿90% of granule step sizes (Fig 4.4e). More details are described in Section 4.A.1.

The flux tracking approach was implemented on 74 scrums obtained from 6 videos of live MIN6 cells containing 2-5 cells per video. Scrum and granule trajectory data were obtained from a video of live MIN6 cells using confocal microscopy imaged at 10 hz frame rate for 3000 frames. While scrum trajectories ranged from 5-300 s (Fig 4.5), only scrum trajectories longer than 100 s were used for analysis. This restriction reduces the number of analyzed scrums trajectories to fewer than 20 samples per video. Yet, the quality of each scrum trajectory is vastly enhanced as each trajectory has several observable flux events, thus increasing the range possible of event-to-event times and the number of events per trajectory.

Enter and exit dynamics stochastic processes with random observation rates. The event coordi-

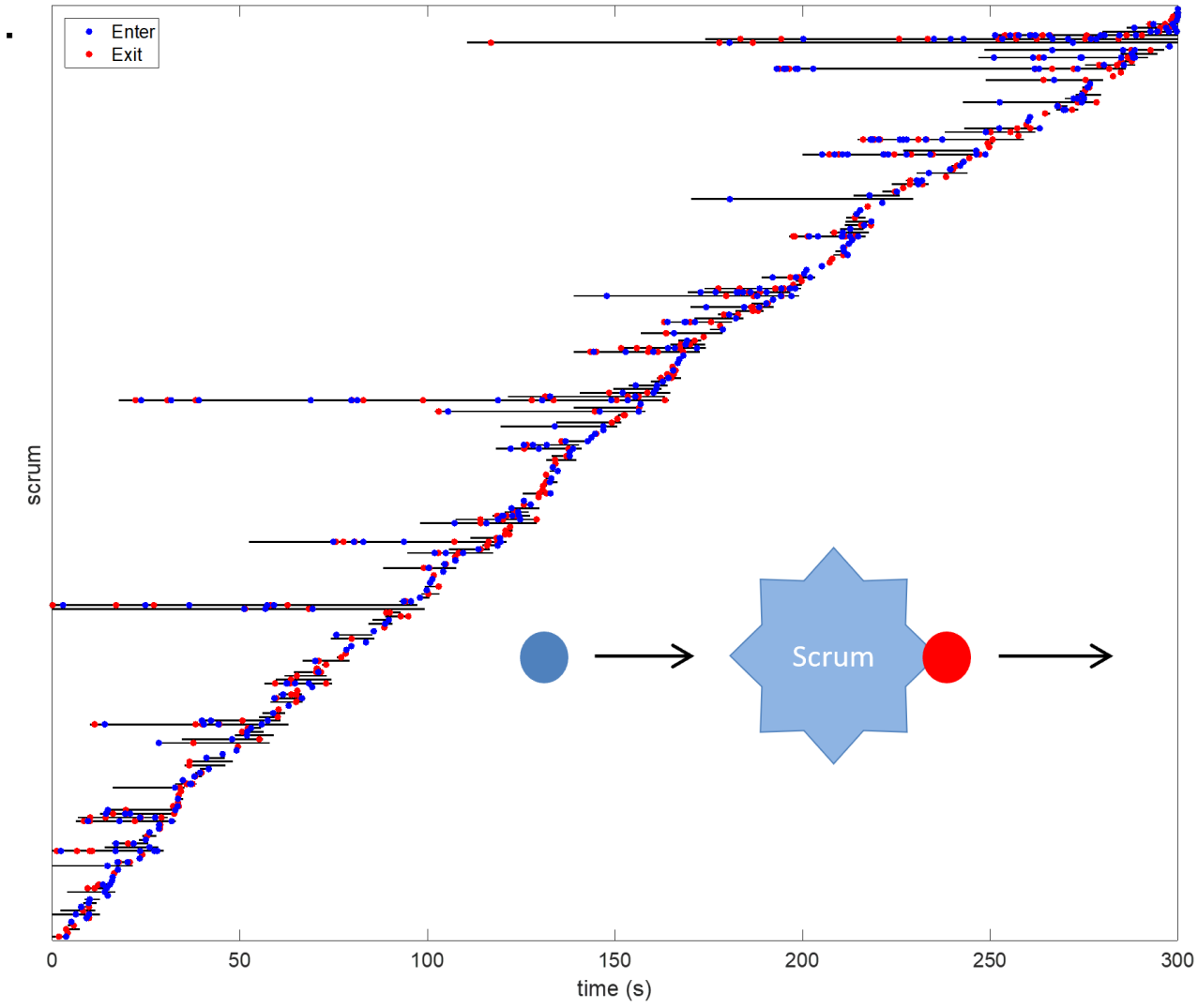

Figure 4.5: **Reaction coordinate for flux of single granules interacting with scrums.** Coordinate of all analyzed scrums (black lines, N = 593 trajectories) with the detected granule arrivals/enters (blue) and granule departures/exits (red) for one video. Interaction Radius is 17 px.

nate obtained from flux analysis is used to study the dynamics of granule flux. We consider whether the two processes are correlated or independent from each other. Then compare the dynamics at basal and glucose stimulated states.

4.5 Scrums are a steady-state granule storage container

The event arrival probability is calculated for both the number of arrivals (enters) and the number of departures (exits) from a scrum at a fixed time interval. The event probability for both cases is Poisson distributed with a Poisson rate parameter of $\lambda_{enter} = 1.4013$ and $\lambda_{exit} = 1.4410$ for the 10 s time interval (Fig 4.6a). These parameters are extracted from fitting the experimental probability distributions to:

$$P(x) = \frac{e^{-\lambda t}(\lambda t)^x}{x!} \tag{4.1}$$

where x is the random variable for the number of events that occur and λt is the average number of occurrences per t units of time [17]. P(x) is the discrete distribution to describe the number of occurrences per unit of time.

The Poisson nature of both the arrival and departure rate indicates that events are independent, or that the enter and exit events are memoryless. While both being independent and random processes, the event rate (λ) for both the enter and exit processes are nearly identical. This could indicate that the flux of granules in and out of a scrum is held at steady-state, because the rate of arrivals and departures are the same. While these conditions also satisfy equilibrium, the biological system is studied *in vivo* which implies that energy is produced and expended in the form of ATP. ATP hydrolysis is utilized by motor proteins to obtain the requisite energy to carry insulin granules throughout the cell.

We consider whether the two processes are correlated. The superposition of independent Poisson processes is the summation of the processes. For $N_i(t), i = 1, ..., k$ are independent Poisson processes with rates λ_i, respectively. Then $N_1(t) + ... + N_k(t)$ is a Poisson process with rate $\lambda_1 + ... + \lambda_k$.

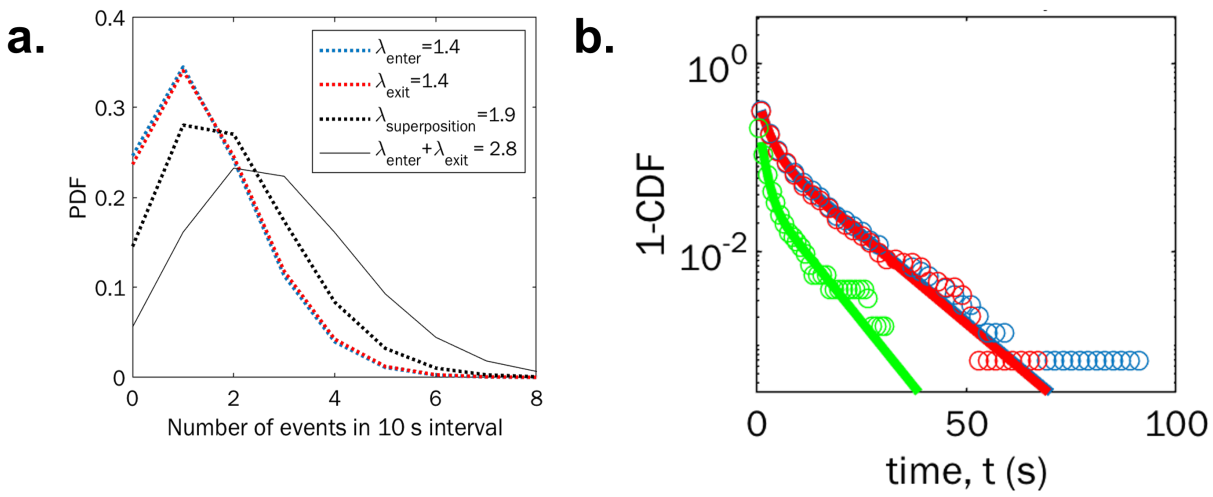

Figure 4.6: **Granule flux is a Poisson counting process.** (a) Probability of event occurrence in a 10s interval for granule enters (blue, dashed; N = 1253 enter events), granule exits out of a scrum (red, dashed; N = 1239 exit events), superposition of the two processes (black, dashed; N = 2492 events). The theoretical independent superposition of the enter and exit process is simulated from 2λ (black, solid). (b) Probability of time until next event (interevent time) for enter (blue, circles), exits (red, circles), and the exit event given an enter event (green, circles). The biexponential fitting is shown (solid lines).

In the case of the steady-state granule flux process, the expected rate is 2λ if the two processes are independent (Fig 4.6a, black solid line). The superposition of the experimental data (Fig 4.6a, black dashed line) has a rate that is lower that the theoretical independent case. To achieve this correlation in the enter and exit rates, the entering granules could be held in the scrum for a period of time before another granule is released.

Interevent, or interarrival, times are exponentially distributed as derived from Poisson counting probability. Considering that the time for the next event occurs at time T, the probability that the even will not be seen at a time t for equation 4.1 is $P(T > t) = P(x = 0) = exp(-\lambda t)$. The probability that an event will occur at time T is $P(T < t) = CDF = 1 - P(x = 0) = 1 - exp(-\lambda t)$. The experimental distribution for the interevent time distributions are biexponential (Fig 4.6b). Here, we rationalize that two Poisson processes contribute to the interevent time distribution: short time-scale subdiffusive crossings and long time-scale superdiffusive crossings (Fig 4.4c&d). The steady state dynamics and shorter dynamics for the combined enter to exit processes still appear in

the interevent probability.

4.6 Scrum release granules at glucose stimulation

The functional role of scrums is studied by comparing the properties of scrums at basal glucose and glucose stimulated conditions. The basal condition measurement is taken from the same sample dish as the glucose stimulated measurement. After glucose stimulation and imaging, the cells are placed in normal growth media overnight to reach the basal state before imaging again. The observed dynamics at basal state after glucose stimulation match the observed dynamics from the never stimulated cells studied in Chapter 3. So observed changed in the scrum and granule dynamics seen during glucose stimulation are reversed back to steady-state dynamics.

The insulin granule dynamics are slower during glucose stimulation. Granule transport at the basal state show a bimodal distribution of α (Fig 4.7a), accessing confined and active transport behavior. At high glucose stimulation, the active transport regime is lost and subdiffusive transport is dominant. In addition to the more confined behavior in glucose stimulated state, the anomalous diffusion coefficient (D_{eff}) favors slower diffusive behavior (Fig 4.7b&d). This seemingly contradicts the cellular directive to mobilize granules at glucose stimulation to increase the number of granules able to dock and secrete insulin out of the cell.

The event rate for granule flux through scrums increases during glucose stimulation. For the same cell passage, the flux rate at basal (Fig 4.8a) and at stimulated (Fig 4.8b) conditions maintain the steady-state rates for the enter and exit as well as correlated behavior compared to the independent superposition. The preparation in Fig 4.8a is the same as Fig 4.6a, but a smaller sample set is analyzed such that Fig 4.8a and Fig 4.8b are from the same sample plate. The number of measurements and precision are sacrificed to avoid influence in dynamics by passage number and variable conditions. Here, the flux rate is increased when in the glucose stimulated state ($\lambda \approx 1.8$ to $\lambda \approx 2.2$ events /30 s).

Granule dynamics slow down and become more confined while the observed flux of granules

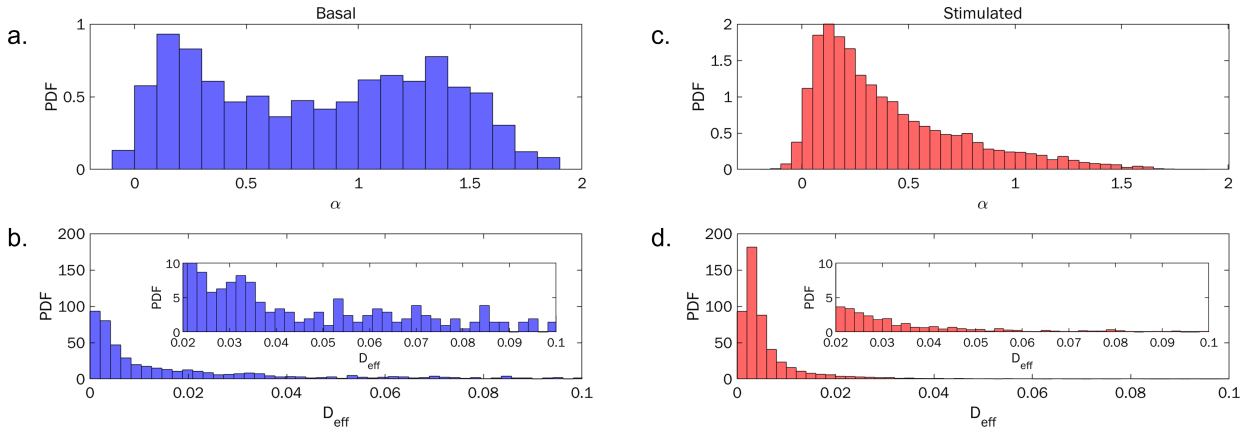

Figure 4.7: **Slow granule transport dynamics at glucose stimulation.** (a) Distribution of α parameter for insulin granules at basal glucose conditions. (b) Distribution of diffusion coefficient (D_{eff}, or K_α) at basal glucose conditions (inset: zoom into tail of distribution). (c) Distribution of α parameter for insulin granules at stimulated glucose conditions. (d) Distribution of diffusion coefficient (D_{eff}, or K_α) at stimulated glucose conditions (inset: zoom into tail of distribution).

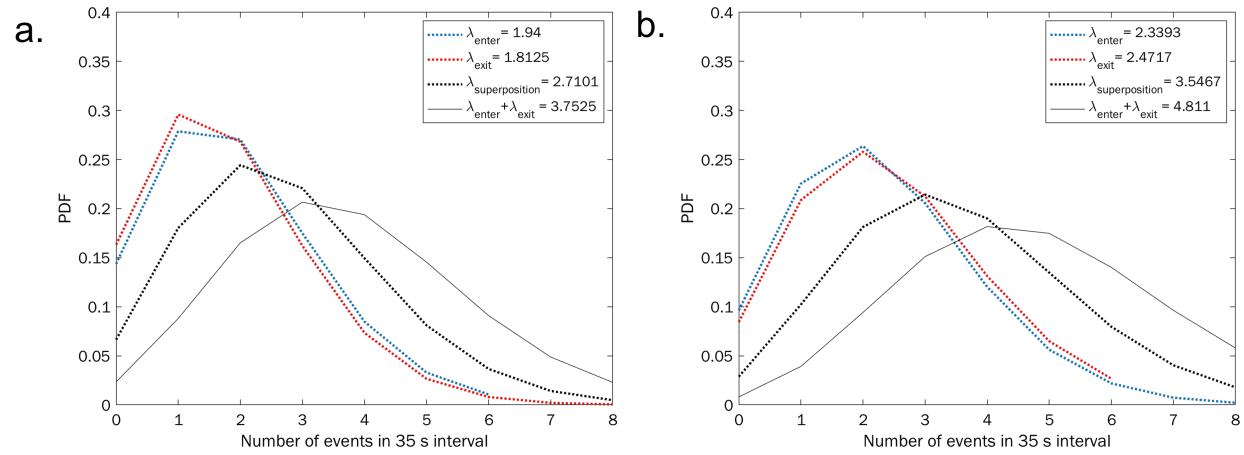

Figure 4.8: **Increased flux rate through scrums at high glucose.** (a) Probability of event occurrence for enter (blue, dashed; N = 100 events), exit (red, dashed; N = 88 events), superposition (black dashed; N = 188 events), and theoretical independent superposition (black solid) under basal glucose conditions. (b) Probability of event occurrence for enter (blue, dashed; N = 136 events), exit (red, dashed; N = 132 events), superposition (black, dashed; N = 268 events), and theoretical independent superposition (black, solid) under glucose stimulated conditions. Analysis window is 35 s.

through scrums increases. These results are seemingly contradictory. We consider if the number of granules increases during glucose stimulation to compensate for the loss in driven motion in granule transport. In this case, the increased granule density will increase the number of crossing events by increasing the probability for independent granules to interact with a scrum.

The number of granules increases during glucose stimulation. This is confirmed by counting the number of granules per cell and then by characterizing the density of granules by the radial distribution function. The number of granules at the basal state is 39.08 ± 14.67 and at the stimulated state, 118.78 ± 35.72 (Table 4.1). These numbers were determined by using the number of detected particles in the first frame on a given video. Localizations by single particle tracking before trajectory filtering and curation are used. The density of granules is also higher because the radial distribution probability has a lower density. The radial distribution, G(r), is the radial probability distribution of particle positions from any particle in an ensemble. In the case of intracellular insulin granules, the ten nearest neighbors of every granule, creating $G_{10}(r)$, were used to simplify the number of pairwise distance calculations. The distribution density of accesses longer distances at the tail of the distribution for insulin granules in basal glucose conditions (Fig 4.9a). In the stimulated case, granules are more closely packed and nearly all distances of the 10 closest neighbors is less than 5 μm (Fig 4.9b).

Table 4.1: **Number of granule localizations per micrograph time series**

Video	Basal Glucose # of localizations/cell (# of cells)	Glucose Stimulation # of localizations/cell (# of cells)
1	38 (2)	133.14 (7)
2	59 (2)	87.14 (7)
3	35.67 (3)	92.25 (8)
4	23.67 (3)	162.57 (7)
Average	39.08 ± 14.67 (2.5)	118.78 ± 35.72 (7.25)

Whether the increase in granule density at glucose stimulation has contribution from the scrum storage containers is analyzed by comparing the size of the scrums at glucose stimulation. Size parameters for each insulin granule are obtained by fitting every granule and scrum localization to

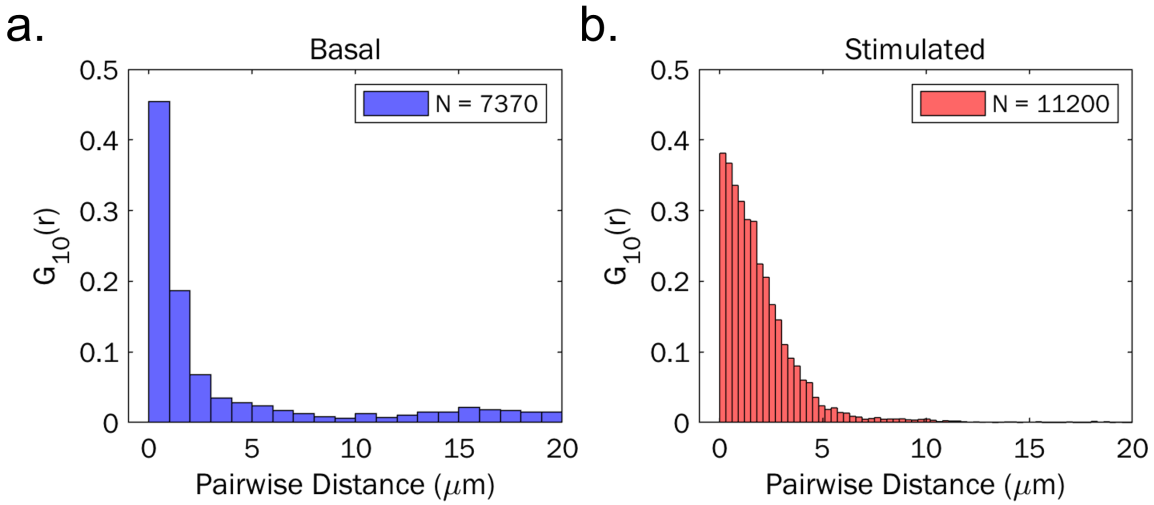

Figure 4.9: **Radial probability distribution of 10 nearest neighbors for basal and glucose stimulated conditions.** (a) Radial probability distribution for the 10 nearest neighbors for insulin granules under basal glucose conditions (8 videos compiled, N = 7370 pair distances). (a) Radial probability distribution for the 10 nearest neighbors for insulin granules under stimulated glucose conditions (7 videos compiled, N = 11200 pair distances).

a Gaussian intensity profile:

$$f(x) = A * \exp\left(\frac{(x-\mu)^2}{2\sigma^2}\right) + c \tag{4.2}$$

The peak height was used as an alternative measure for the number of granules in a scrum. At diffraction limited distances, such as the close packing of granules in a scrum, the individual fluorescense emission signals convolve and the image of the clustered spot will have a higher peak intensity than the individual particle peaks. The peak intensity of every granule and scrum is fitted and the distribution of the ensemble (scrums and granules) and only granules are compared. A challenge in comparing size of particles among different microscopy video is the variable signal to noise for each acquisition (fluorophore density, excitation light source power, camera gain, exposure time, etc.) that can modulate the height of the curve's peak height (A) or the width (σ). The fitted peak heights are normalized by the average granule peak height of every video so that the expected I/I_{avg} for the ensemble distribution dominated by granules is $\approx$1.

The intensity difference in ensemble and scrum distributions is greater under basal glucose

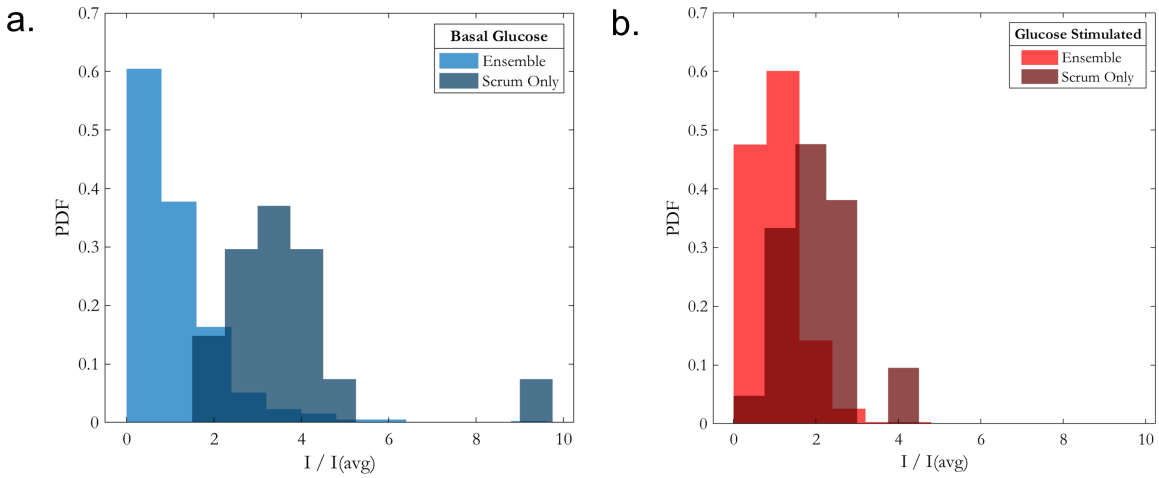

Figure 4.10: **Relative granule and scrum particle intensity distributions for basal and glucose stimulated conditions.** (a) Relative intensity distribution for all scrum and granule (light blues; 4 videos combined (10 cells), N = 490 localizations) and only scrum (dark blue; 4 videos combined (10 cells), N = 18 localizations) particle localizations under basal glucose conditions. (b) Relative intensity distribution for all scrum and granule (light red; 4 videos combined (29 cells), N = 828 localizations) and only scrum (dark red; 4 videos combined (29 cells), N = 18 localizations) particle localizations under stimulated glucose conditions.

conditions. The distribution peaks for the relative particle intensity in basal conditions (Fig 4.10a) show a higher difference than the peak-to-peak distance under glucose stimulated conditions (Fig 4.10b). Assuming that size and intensity of a insulin granule does not change at different glucose conditions, then the number of insulin granules per scrum decreases under glucose stimulated conditions (Table 4.2).

Table 4.2: **Comparison of I/I_{avg} relative intensities of all localizations and scrum localizations**

Glucose Condition	Ensemble (I/I_{avg})	Scrum Only (I/I_{avg})	Difference
Basal (n=4 videos)	1.11 ± 1.08	4.02 ± 2.33	3.41 ± 1.71
Stimulated (n=4 videos)	1.03 ± 0.58	2.08 ± 0.89	1.05 ± 0.74
% change	-7.21 ± 1.23%	-48.26 ± 0.92%	

4.7 Conclusion

This chapter introduces a novel storage structure found in insulin-containing MIN6 cells. The discovery of these storage clusters, termed scrums, was from the comprehensive labeling approach using CRISPR/cas9 technology to fuse a fluorescent protein tag into the insulin vesicles. The full labelling method allows for the discovery of these unforeseen clusters and the granule clustering structure was corroborated with super-resolution microscopy. Using a custom developed image analysis program, the flux of single granules in and out of scrums was found to be at a meta-stable steady-state.

The mobilization of insulin granules at glucose stimulation is critical for blood glucose management. Studying the mobilization for second phase secretion from the reserve pool of granules is challenged by the lack of physical or biological markers to identify reserve pool granules. We show that one mechanism that the reserve pool uses to mobilize granules for insulin secretion is the release of granules stored in scrums. This release property is critical for mobilization to compensate for the observed slower dynamics in granule movement which decreases the probability for a granule to come in contact with a dock site.

Comparison between the size decrease in scrums and the population increase in granules show proportional, yet opposite contributions. The number of granules present after glucose stimulation is $\sim$ 3x greater than in the basal state (Table 4.1). We considered how many granules produced are associated with the observed decrease in scrum size. There is a $\sim$ 2x reduction, or -50% change, in the relative scrum signal intensity (Table 4.2). The number of granules released to contribute to the 2x signal intensity decrease is more than 2x granules released. The convolved signal intensity of two or more particles in close distance is less than the addition of the individual signal intensities.

The implications of an intracellular vesicle storage system are profound for cellular regulation of metabolic processes. In particular, a reversible storage system for insulin secretory granules can be a physical method for directing stimulated and basal insulin dynamics towards glucose stimulated insulin secretion. A possible boundary condition for the finite carrying capacity of

granules in a scrum could be the mesh pores of the microtubule network. Several mechanisms have been conceived theoretically [18] and observed experimentally[19][20] for vesicle cargo systems that are trapped in small pores of the microtubule network. So, we consider that the scrums are an aggregate phenomenon from these mechanisms. Then, conformational and dynamic changes in the microtubule network from glucose stimulation would regulate the carrying capacity of the trapped scrums [21]. Future work should consider the interplay of microtubules and insulin granules. In particular, the dynamics of both microtubules and scrums at a glucose stimulated state will give new mechanistic insight into glucose stimulated insulin secretion.

REFERENCES

[1] Julie Støy, Donald F Steiner, Soo-Young Park, Honggang Ye, Louis H Philipson, and Graeme I Bell. Clinical and molecular genetics of neonatal diabetes due to mutations in the insulin gene. *Reviews in Endocrine and Metabolic Disorders*, 11(3):205–215, 2010.

[2] Noriko Takahashi, Hiroyasu Hatakeyama, Haruo Okado, Jun Noguchi, Mitsuyo Ohno, and Haruo Kasai. Snare conformational changes that prepare vesicles for exocytosis. *Cell metabolism*, 12(1):19–29, 2010.

[3] Guy A Rutter and Elaine V Hill. Insulin vesicle release: walk, kiss, pause... then run. *Physiology*, 21(3):189–196, 2006.

[4] Troitza K Bratanova-Tochkova, Haiying Cheng, Samira Daniel, Subhadra Gunawardana, Yi-Jia Liu, Jennifer Mulvaney-Musa, Thomas Schermerhorn, Susanne G Straub, Hiroki Yajima, and Geoffrey WG Sharp. Triggering and augmentation mechanisms, granule pools, and biphasic insulin secretion. *Diabetes*, 51(suppl_1):S83–S90, 2002.

[5] Susanne G Straub and Geoffrey WG Sharp. Glucose-stimulated signaling pathways in biphasic insulin secretion. *Diabetes/metabolism research and reviews*, 18(6):451–463, 2002.

[6] Patrik Rorsman and Erik Renström. Insulin granule dynamics in pancreatic beta cells. *Diabetologia*, 46(8):1029–1045, 2003.

[7] Charlotta S Olofsson, Sven O Göpel, Sebastian Barg, Juris Galvanovskis, Xiaosong Ma, Albert Salehi, Patrik Rorsman, and Lena Eliasson. Fast insulin secretion reflects exocytosis of docked granules in mouse pancreatic b-cells. *Pflügers Archiv*, 444(1):43–51, 2002.

[8] Aniko Varadi, Takashi Tsuboi, Linda I Johnson-Cadwell, Victoria J Allan, and Guy A Rutter. Kinesin i and cytoplasmic dynein orchestrate glucose-stimulated insulin-containing vesicle movements in clonal min6 β-cells. *Biochemical and biophysical research communications*, 311(2):272–282, 2003.

[9] Rosita Ivarsson, Stefanie Obermüller, Guy A Rutter, Juris Galvanovskis, and Erik Renström. Temperature-sensitive random insulin granule diffusion is a prerequisite for recruiting granules for release. *Traffic*, 5(10):750–762, 2004.

[10] Aristea E POULI, Evaggelia EMMANOUILIDOU, Chao ZHAO, Christina WASMEIER, John C HUTTON, and Guy A RUTTER. Secretory-granule dynamics visualized in vivo with a phogrin–green fluorescent protein chimaera. *Biochemical Journal*, 333(1):193–199, 1998.

[11] Mingming Hao, Xia Li, Mark A Rizzo, Jonathan V Rocheleau, Benoit M Dawant, and David W Piston. Regulation of two insulin granule populations within the reserve pool by distinct calcium sources. *Journal of cell science*, 118(24):5873–5884, 2005.

[12] June Chunqiu Hou, Le Min, and Jeffrey E Pessin. Insulin granule biogenesis, trafficking and exocytosis. *Vitamins & Hormones*, 80:473–506, 2009.

[13] Rory R Duncan, Jennifer Greaves, Ulrich K Wiegand, Ioulia Matskevich, Georg Bodammer, David K Apps, Michael J Shipston, and Robert H Chow. Functional and spatial segregation of secretory vesicle pools according to vesicle age. *Nature*, 422(6928):176–180, 2003.

[14] Anna Ivanova, Yannis Kalaidzidis, Ronald Dirkx, Mihail Sarov, Michael Gerlach, Britta Schroth-Diez, Andreas Müller, Yanmei Liu, Cordula Andree, Bernard Mulligan, et al. Age-dependent labeling and imaging of insulin secretory granules. *Diabetes*, 62(11):3687–3696, 2013.

[15] Li Ma, Vytautas P Bindokas, Andrey Kuznetsov, Christopher Rhodes, Lori Hays, J Michael Edwardson, Kazuya Ueda, Donald F Steiner, and Louis H Philipson. Direct imaging shows that insulin granule exocytosis occurs by complete vesicle fusion. *Proceedings of the National Academy of Sciences*, 101(25):9266–9271, 2004.

[16] Stefan W Hell and Jan Wichmann. Breaking the diffraction resolution limit by stimulated emission: stimulated-emission-depletion fluorescence microscopy. *Optics letters*, 19(11):780–782, 1994.

[17] Don S Lemons. An introduction to stochastic processes in physics, 2003.

[18] Monika Scholz, Stanislav Burov, Kimberly L Weirich, Björn J Scholz, SM Ali Tabei, Margaret L Gardel, and Aaron R Dinner. Cycling state that can lead to glassy dynamics in intracellular transport. *Physical Review X*, 6(1):011037, 2016.

[19] Linnea M Lemma, Michael M Norton, Alexandra M Tayar, Stephen J DeCamp, S Ali Aghvami, Seth Fraden, Michael F Hagan, and Zvonimir Dogic. Multiscale microtubule dynamics in active nematics. *Physical Review Letters*, 127(14):148001, 2021.

[20] Kejia Chen, Bo Wang, and Steve Granick. Memoryless self-reinforcing directionality in endosomal active transport within living cells. *Nature Materials*, 14(6):589–593, 2015.

[21] Kung-Hsien Ho, Xiaodun Yang, Anna B Osipovich, Over Cabrera, Mansuo L Hayashi, Mark A Magnuson, Guoqiang Gu, and Irina Kaverina. Glucose regulates microtubule disassembly and the dose of insulin secretion via tau phosphorylation. *Diabetes*, 69(9):1936–1947, 2020.

4.A Appendix: Supporting Information

4.A.1 Determining granule flux through scrums

Single particle tracking requires two steps: (1) particle detection, or localization, for spot shaped targets at every time frame and (2) frame-to-frame linking of particle positions to form trajectories. Particle detection gives position and time information, then linking assigns a unique trajectory ID for every moving particle over time. ImageJ was used to determine the particle localization for granules (r = 4 px) and scrums (r = 10 px) with the MOSAIC plugin [1]. In some cases, overlapping particle identifications occur; a granule particle is detected in same location and time as a scrum particle. The degenerate localizations are maintained in the scrum particle list, but are removed from the granule particle list in post-processing using MATLAB. The granule and scrum particle lists are then re-linked into trajectory lists using the Crocker-Grier linking algorithm which constructs trajectories from a list of particle position and time points by minimizing the distance travelled frame-to-frame [2]. Nearly 600 scrums trajectories are studied by tracking the flux of granules in and out of a scrum.

For every scrum, instances of granules entering (blue) and exiting (red) are detected and the time of the event is recorded as represented in Fig 4.4a. Granule enter or exit events are identified as the time when a granule trajectory crosses a pre-defined interaction radius centered at the scrum (Fig 4.4b, dashed black line). The number of detected events scales linearly with the interaction radius because the perimeter of the interaction circle ($2\pi r$) also increases linearly with radius (r). So, the total size of the detection circle is increased with larger radius thus allowing for more possible detected events. A detection annulus (Fig 4.4b, yellow ring) is defined to reduce the number of granule trajectories that are tested for interaction radius crossing. The number of candidate trajectories is far smaller than the total number of granule trajectories; typically 10-30 potentially interacting granule trajectories out of nearly 200,000 total granule trajectories.

Two cases of granule transport are considered for the observed flux dynamics. Subdiffusive

motion, where the α parameter of the Mean Squared Displacement (MSD) is less than 1, is motion that is confined from crowding effects or multi-motor mechanisms[3, 4]. In contrast, superdiffusive motion, where $\alpha > 1$, shows active transport in a directional or driven manner. The distinct traces manifest into characteristic radius crossing dynamics. Opportunistic crossing from granules undergoing subdiffusive motion result in several crossing events in a short period of time from a single granule (Fig 4.4c). Directed crossing events from actively transported granules show a single crossing event for each interacting granule (Fig 4.4d). Both classes of granule motion are observed in the ensemble granule trajectories analyzed for a single video. The distribution of α obtained from the time-averaged MSD (taMSD $=< [R(t) + R(t + \Delta)]^2 > \propto \Delta^{\alpha}$, where $< ... >$ is the time-average at fixed Δ and R is the particle position) for every granule trajectory is bimodal, corresponding to the two diffusive regimes (Fig 4.4e).

To calculate enter and exits events through a scrum with a specified interaction radius, r_2, all candidate trajectories ($R'_g(x, y, t, id)$) are first identified from the list of all granule trajectories ($R_g(x, y, t, id)$) for a scrum trajectory ($R_s(x, y, t, id)$) as

$$R'_g = R_s + r_2 \leq R_g \leq R_s + r_1 \tag{4.3}$$

where r_2, the outer radius of the annulus is always 1.5 px + r_1. Note that all granule trajectories (every granule id) are analyzed for each single scrum trajectory (per scrum id). The width of the detection ring (1.5 px) was chosen from the distribution of step sizes for granule trajectories (Fig 4.4f). The 1.5 px annulus width is sufficiently large enough to capture > 90% of trajectory steps based on the experimentally derived step size distribution of all analyzed trajectories.

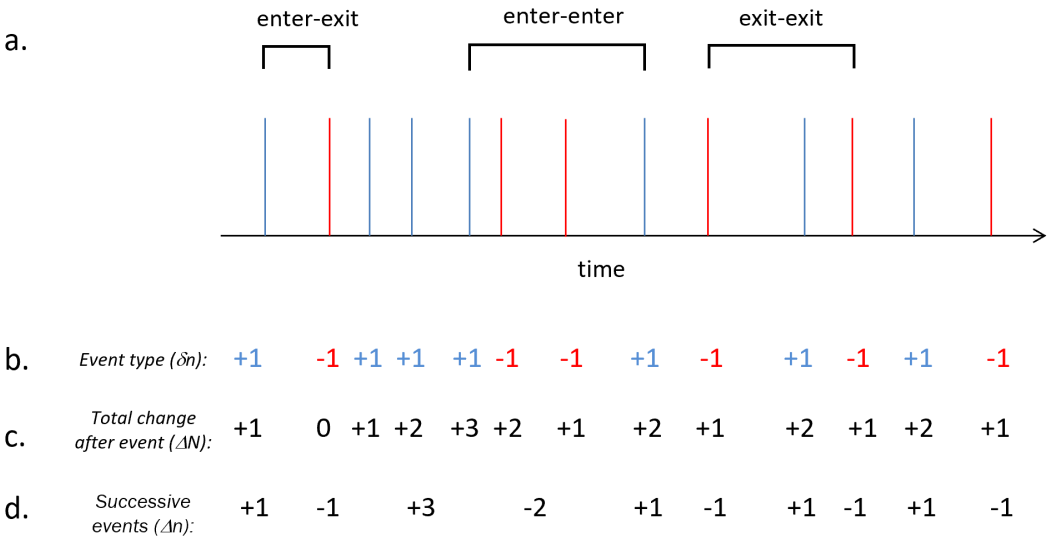

Figure 4.11: **Determining flux dynamics parameters.**(a) Simplified schematic of reaction coordinate showing enter (blue) and exit (red) events of granules through a scrum. Enter-exit times are calculated for every enter event and their nearest, subsequent exit event. Enter-enter times are calculated for every enter event and the nearest, subsequent enter event. Exit-exit times are calculated for every exit event and the nearest, subsequent exit event. (b) The mass or particle flux is determined from the event type where the type $(\delta n) = \{+1, -1\}$ for enter and exit events, respectively. (c) The total change of the number of particles in a scrum (ΔN) is calculated from the cumulative sum of the event types. This is assuming the initial state of the scrum is $\Delta N = 0$. (d) The number of successive steps (Δn) is calculated as the sum of successive, identical event types. In the representation in (a), there are two cases of successive events shown by +3 and -2.

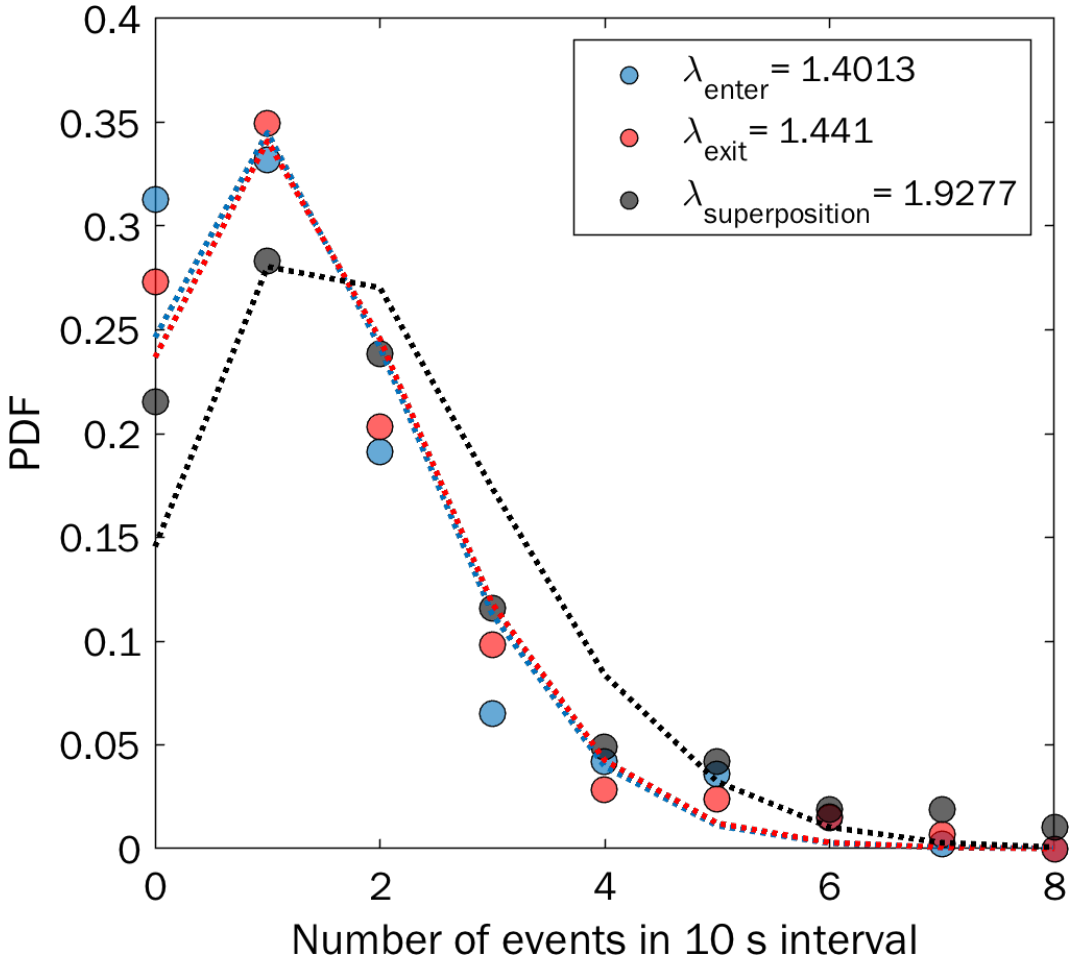

Figure 4.12: **Experimental and fitting Poisson counting.** Experimental distribution of enter (blue, circles), exit (red, circles), and the superposition of enter and exit (black, circles) events in a 10 second time window. The rate parameter λ is found by the average event occurrence and the fit is plotted in the corresponding dashed lines. The theoretical distribution for the superposition of two independent processes is calculated as $\lambda_{super} = \lambda_{enter} + \lambda exit$ (black, solind lines)

4.A.2 Poisson process fitting

4.A.3 Waiting time and mass flux statistics

For a Poisson process, the inter-event times are exponentially distributed [5]. This is derived from the the event probability P(x) considering whether an event at time T_i is observed. The total time until the ith event (T_i) and the waiting time until the ith event (t_i) are expressed as

$$T_i = t_1 + t_2 + ... + t_N, \;\; i \geq 1$$

$$t_i = T_i - T_{i-1}.$$

For convention, T_0 is the time when the scrum trajectory is first detected where $T_0 = 0$. Therefore, the total time until the ith event (T_i) is relative to when the scrum is detected with respect to the total measurement time of a video.

If the first occurrence is at time T_1, then the probability to observe an event at a time before the first event ($T_1 > t$) is the same as the probability of observing no events P(x=0). This is substituted into Eq. 4.1, which shows that the probability to observe an event is exponentially distributed:

$$P(T_1 > t) = P(x = 0) = e^{-\lambda t} \tag{4.4}$$

Conversely, the probability to observe the first event is the same as the cumulative distribution function, given as:

$$CDF = P(T_1 \leq t) = 1 - P(x = 0) = 1 - e^{-\lambda t}. \tag{4.5}$$

The waiting times (t_i), or inter-event times, are calculated and represented in Fig. 4.11a for consecutive enters (enter-enter), consecutive exits (exit-exit) and the conditional enter-exit. This parameter is commonly referred to as the inter-arrival time. In this study, the term inter-event times is used instead as both arrival (enters) and departures (exits) are analyzed for their Poisson-like

counting statistics.

The mass flux is also calculated by counting the number of entering and exiting granules in a scrum. In Fig 4.11b, the event type for the ith event (δn_i) is represented as

$$\delta n_i = \begin{cases} -1, & R_g(T_{i-1}) > r_1 \ \text{ (exit events)} \\ +1, & R_g(T_{i-1}) \leq r_1 \ \text{ (enter events)} \end{cases} \tag{4.6}$$

where $R_g(T_{i-1})$ is the granule distance from the scrum at the occurrence time of the $i-1$th event and r_1 is the interaction radius defined for the analysis. Assuming the location of the interacting granule at the event occurrence time is about the same distance as the interaction radius, $R_g(T_i) \sim r_1$, the looking at the previous granule location at the previous time step will give information about the direction of granule flux. Enter events are assigned a change in granule mass of +1 and exits events are assigned -1 with respect to the change in the number of granules in a scrum.

In Fig 4.11c, the cumulative sum of the event types for a scrum gives the total change in the capacity state of the scrum (ΔN):

$$\Delta N_i = \sum_{k=1}^{i} \delta n_k \ \text{ for } i = 1, 2, ..., N. \tag{4.7}$$

Note that the starting capacity state is assumed to be $\Delta N = 0$. This starting condition implies that the first observed state of a scrum is at an energetic local minimum $\Delta N = 0$ for the steady-state system. The corresponding waiting time, t_i, is recorded for every measurement of the scrum capacity state, ΔN_i, and the probability is reported in the sum of waiting times ($\sum t_i$) in each ΔN_i state. This is reminiscent of a joint probability for the waiting time and capacity state (P(t,ΔN)) and reports the time-weighted probability that a scrum is in a specific carrying state.

The number of successive events, as demonstrated in Fig 4.11d, is tabulated as:

$$\Delta n_i = \sum_{k=1}^{i} \delta n_k \ \text{ while } \delta n_{i-1} = \delta n_i \ \text{ for } i = 1, 2, ..., N. \tag{4.8}$$

The number of successive steps is similarly calculated as a cumulative sum. The key condition in successive step determination is that the event type (δn) in the previous step and the current step are the same.

4.A.4 Steady-state dynamics and flexible storage capacity

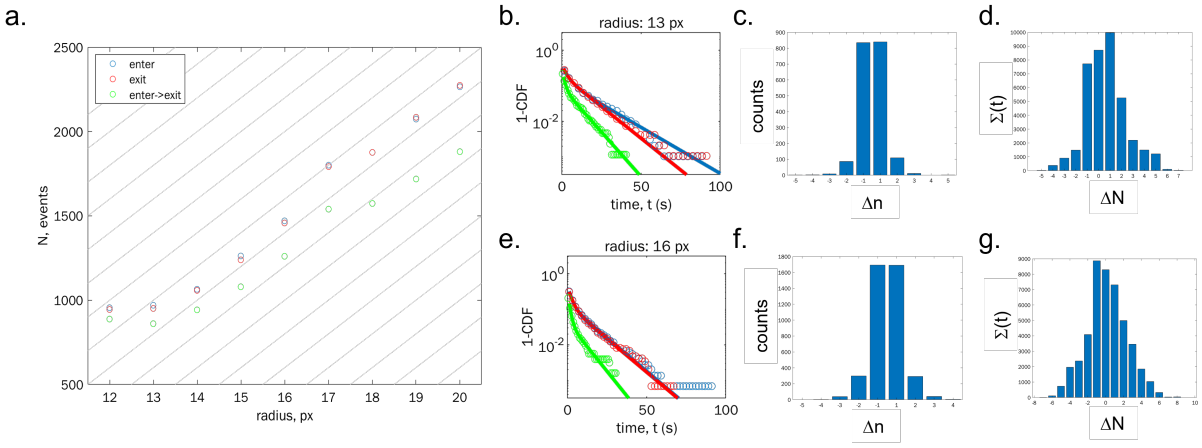

Figure 4.13: **Scrums are dynamic storage mechanisms with flexible carrying capacity.**(a) Statistics for the interaction radius and the number of detected successive events (enter-enter, blue; exit-exit, red; enter-exit, green). Number of events increases with larger radius linearly which scales with the increased circumference of the interaction radius. Guidelines in gray are slope m = 200 events/px. (b) First passage time probability for enters (blue), exits (red), and enter-to-exit (green) from flux events detected with an interaction radius of 13 px. Distributions are fitted to a biexponential decay (solid lines). (c) Distribution of successive, identical events from flux events detected with an interaction radius of 13 px. (d) Time-weighted probability for the dwell time in a given carrying capacity from flux events detected with an interaction radius of 13 px. (e-g) Identical data as respective panels (b-d) from the flux events detected with an interaction radius of 16 px. Note that the x limits are not consistent in the two rows of data.

Several interaction radius sizes were considered for analyzing scrum flux events. The number of inter-event times analyzed increases linearly with interaction radius size; around 200 additional events per 1 pixel increase in interaction radius (Fig 4.13a). As the detection boundary circle increases with interaction radius, there is an increased probability of detecting granule flux events. The circumference of the detection boundary scales linearly with the interaction radius as $2\pi r$ to lead to the observed trend in detectable events.

The ideal interaction radius balances two competing factors. First, the accuracy of detecting "true" flux events is favored at small interaction radii. With the detection circle being closer to the scrum, the detected granules that cross the detection boundary will ultimately contribute to or interact with the scrum. In contrast, a detection circle placed further away from the scrum will detect nearby granules that do not directly interact with the scrum. The second factor is the counting statistics which favors large interaction radii. The subsequent probabilistic metrics (Fig 4.11a,c,d) will have higher resolution in their binning to create discrete probability distributions as more observable events are used. Scrum metrics are analyzed for an interaction radius of 13 pixels (Fig 4.13b-d) and interaction radius of 16 pixels (Fig 4.13e-g).

The inter-event time probability is represented as a survival function, or complementary cumulative distribution function, for the three inter-event samplings (Fig 4.13b&e). The survival function, S(t), is commonly used in population survival dynamics and failure rate assessment to estimate the likeliness of an event (usually a death or failure variable) to occur as a function of time. This can be calculated from the cumulative distribution function as S(t) = 1-CDF, so that the survival function approaches likeliness of S(t) = 0 at a large observation time [5]. In terms of the inter-event times, the survival function reports the probability for the next event to occur. The probability approaches 0 at long times because of the vanishingly small probability that no events will happen in the future. For Poisson processes such as scrum flux, the survival function is exponential as represented in Equation 4.4.

Inter-event times are, notably, biexpoentially distributed for the three sampling methods (consecutive enters, consecutive exits, and enter to exit time). The biexponential probability manifests from two underlying Poisson event occurrence rates that contribute the event time probability. The short dynamic process is mainly from the diffusing granules that cross several times over the interaction boundary (Fig 4.4c). The longer dynamics are from the actively transported scrums (Fig 4.4d). Importantly, the inter-event times at the short time scale reflect the event dynamics of a single granule across the detection boundary and may be an artifact of the image analysis ap-

proach. The true granule flux events are reflected in the longer time scale where inter-event times are sampled from different granules entering or exiting the scrum.

The scrums have a finite storage capacity that is identified in the dynamic, time-domain probability and in the counting statistics. Dynamic evidence in Fig 4.13 b&e show that the inter-event time probability for consecutive enters and exits are the same, a consequence of the steady-state condition. Yet, the expected time between enter to exit events (green curve) is shorter. Since the scrums exist at the steady-state carrying capacity, an additional granule entering the scrum destabilizes scrum and another granule is pushed out of the scrum to maintain stability. The likeliness to kick out a granule faster than observing a second consecutive enter is also reflected when counting the consecutive enter/exit events (Fig 4.13c&f). Here, the probability of having a single enter ($\delta n = +1$) or single exit (($\delta n = -1$) is far higher than observing consecutive enters or exits. The fact that the trends are observable in both interaction radii shows the robust performance of the image analysis approach.

The notion of a stable carrying capacity is bolstered when counting the number of granules in and out of a scrum by counting consecutive events (Fig 4.13c&f) and measuring the relative overall carrying state (Fig 4.13d&g). Both counting approaches are centered at the δn or δN state of 0 which would be the optimal carrying state of the scrum. Fig 4.13d&g report the total amount of time a scrum stays in a carrying state and peaks at the carrying state $\Delta N = 0$. The total carrying state counts how many granules have joined or left the scrum since the start of the scrum trajectory. So, a total carrying state of $\Delta N = -2$ would mean that there was a net change of two granules exiting the scrum since that start of the measurement. A total carrying state of $\Delta N = 0$ is the most likely state that was recorded and means that the scrum state at the start of measurement is the most favorable or stable condition.

4.A.5 Interaction Radii v. Interevent Times

The flux dynamics were analyzed at several interaction radii (R = 12 px - 20 px) and the interarrival distribution was fit to a biexponential decay:

$$I(t) = A_1 e^{-\frac{1}{\tau_1}} + A_2 e^{-\frac{1}{\tau_2}}. \tag{4.9}$$

In nearly all cases, the nonlinear least squares fitting converged to fit the experimental distribution to Eqn 4.9. The fitted parameters are summarized in Tables 4.3, 4.4, and 4.5. The conserved dynamics for steady-state condition and faster conditional enter-to-exit rate show the robust performance of the analysis method over several interaction radii.

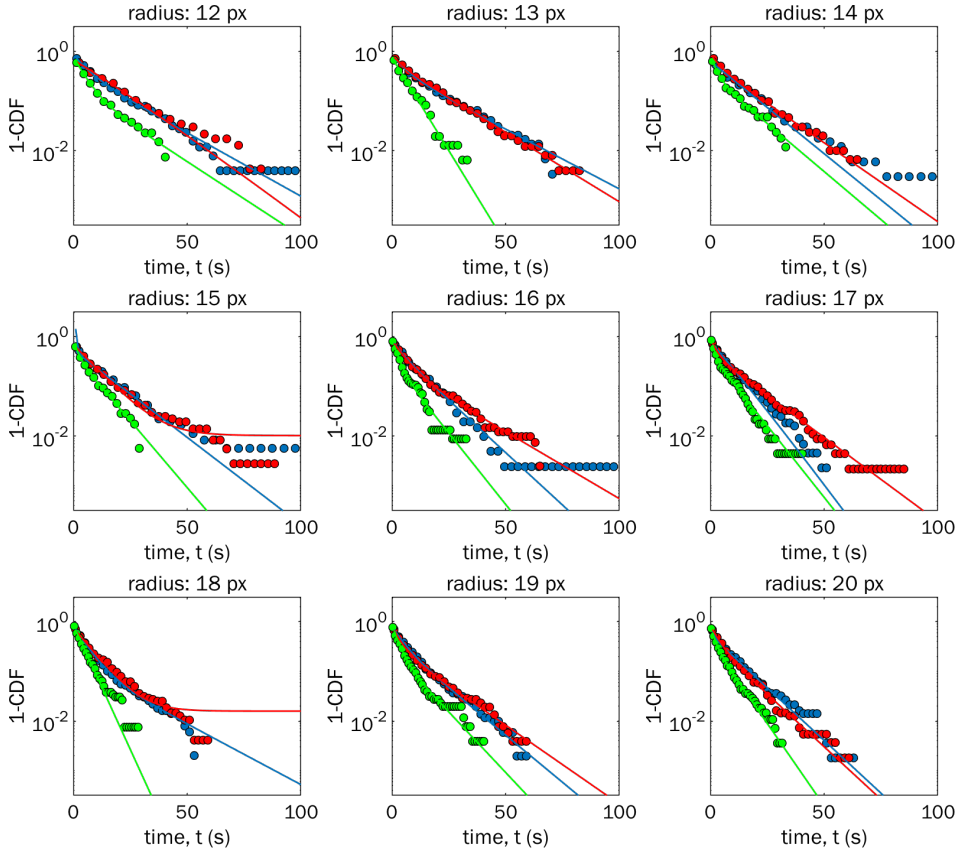

Figure 4.14: **Robust dynamics over several interaction radii.**

Table 4.3: **Enter Interarrival Time Fits**

Radius (px)	A_1	τ_1	A_2	τ_2
12	0.4291	5.3241	0.4301	17.0430
13	0.4123	5.098	0.4320	18.0584
14	0.59401	0.1696	0.6273	11.6911
15	4.835	0.6071	0.5285	12.40851
16	0.25790	3.8350	0.59260	10.3101
17	-18.3394	6.6086	19.1326	6.6632
18	0.68302	5.4092	0.1452	17.7682
19	0.4034	4.2780	0.4107	11.4330
20	0.3461	1.2533	0.5404	10.2179

Table 4.4: **Exit Interarrival Time Fits**

Radius (px)	A_1	τ_1	A_2	τ_2
12	-6.8115	11.7449	7.4789	12.0112
13	0.2758	3.9614	0.5819	15.5524
14	0.3234	3.8197	0.5560	13.6898
15	0.01038	10266.477	0.6813	9.0867
16	0.5621	5.2592	0.2691	16.15
17	0.45967	2.5089	0.45793	12.8638
18	0.01573	-14054.236	0.74604	7.6808
19	0.4935	3.5147	0.3201	13.6601
20	0.3966	10.2535	0.4416	3.6280

Table 4.5: **Enter to exit Interarrival Time Fits**

Radius (px)	A_1	τ_1	A_2	τ_2
12	0.5833	4.502	0.1874	14.552
13	0.6051	0.0050	0.7431	5.8112
14	0.47543	2.4856	0.3254	11.2428
15	0.4461	8.0872	0.42078	1.7023
16	0.3104	7.577	0.6261	2.2219
17	0.6103	1.3600	0.4424	7.5456
18	0.86375	4.32700	-19.7025	0.02755
19	0.25203	8.9023	0.6265	2.6218
20	0.40671	6.5471	0.46425	1.6745

4.A.6 Image Normalization for Intensity analysis

Challenges in comparing granule signal parameters such as width and peak height stem from varied signal-to-noise ratios (SNR). Fig 4.15 shows the need for normalization to relative size parameters. Scrums in low signal-to-noise conditions (Fig 4.15a&c) are lower in signal intensity and image width. The difference in SNR leads to scrums in low SNR videos (Fig 4.16a) to have comparable intensity profiles as granules from high SNR videos (Fig 4.16d).

Granule intensity profiles are normalized to the mean granule intensity in each video. The normalization with respect to the average granule intensity leads to the expected normalized peak height to be 1 across all videos and SNR conditions. This is depicted in Fig 4.16 which is the normalized images and signal intensity profiles for the same granules and scrums as Fig 4.15. The relative intensity of the low SNR scrum (Fig 4.16a) is higher, implying that the number of granules at the local area is greater or that the distance between neighboring granules in closer.

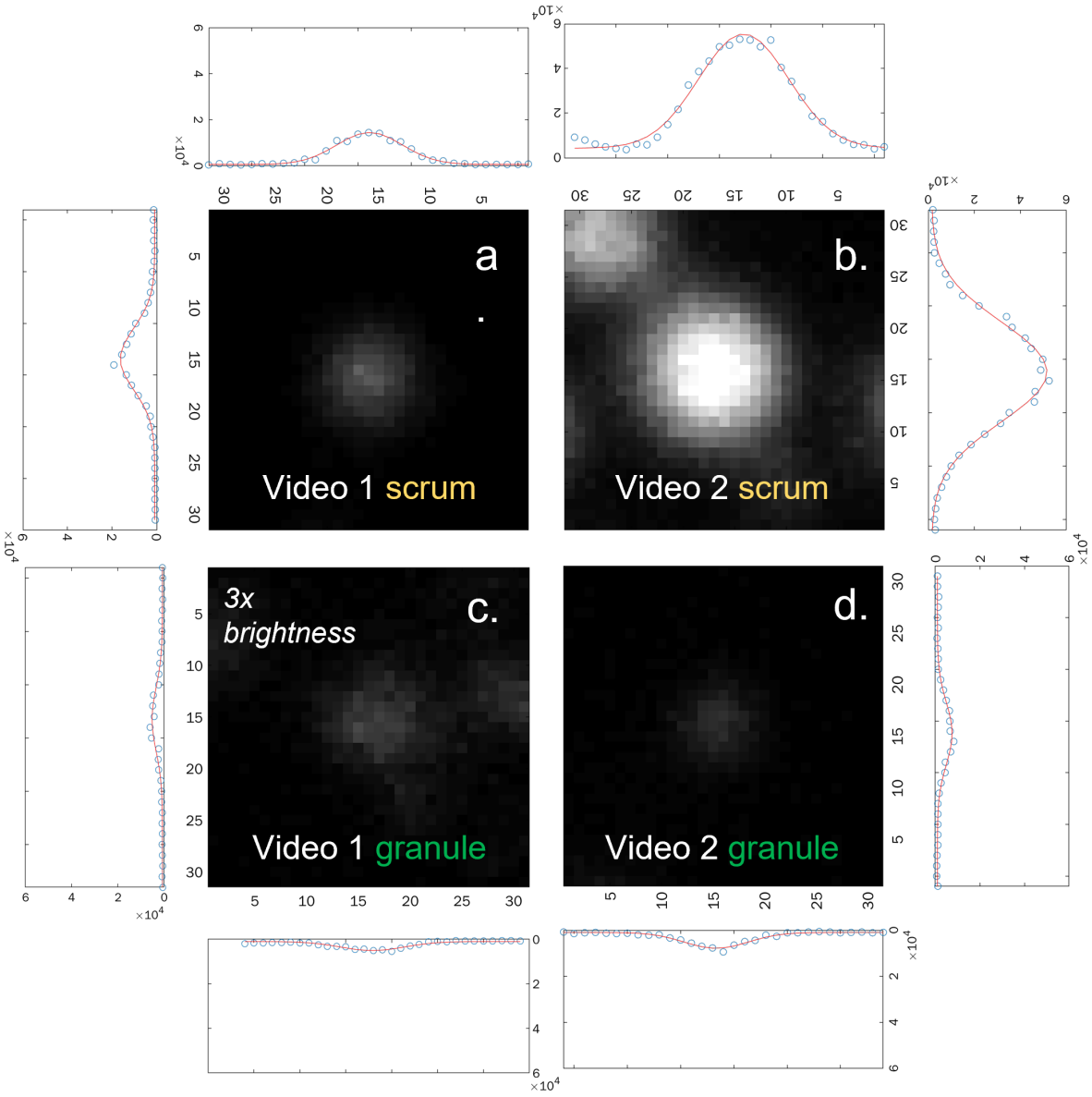

Figure 4.15: **Sample scrum and granule images and signal intensity profile for two videos.**

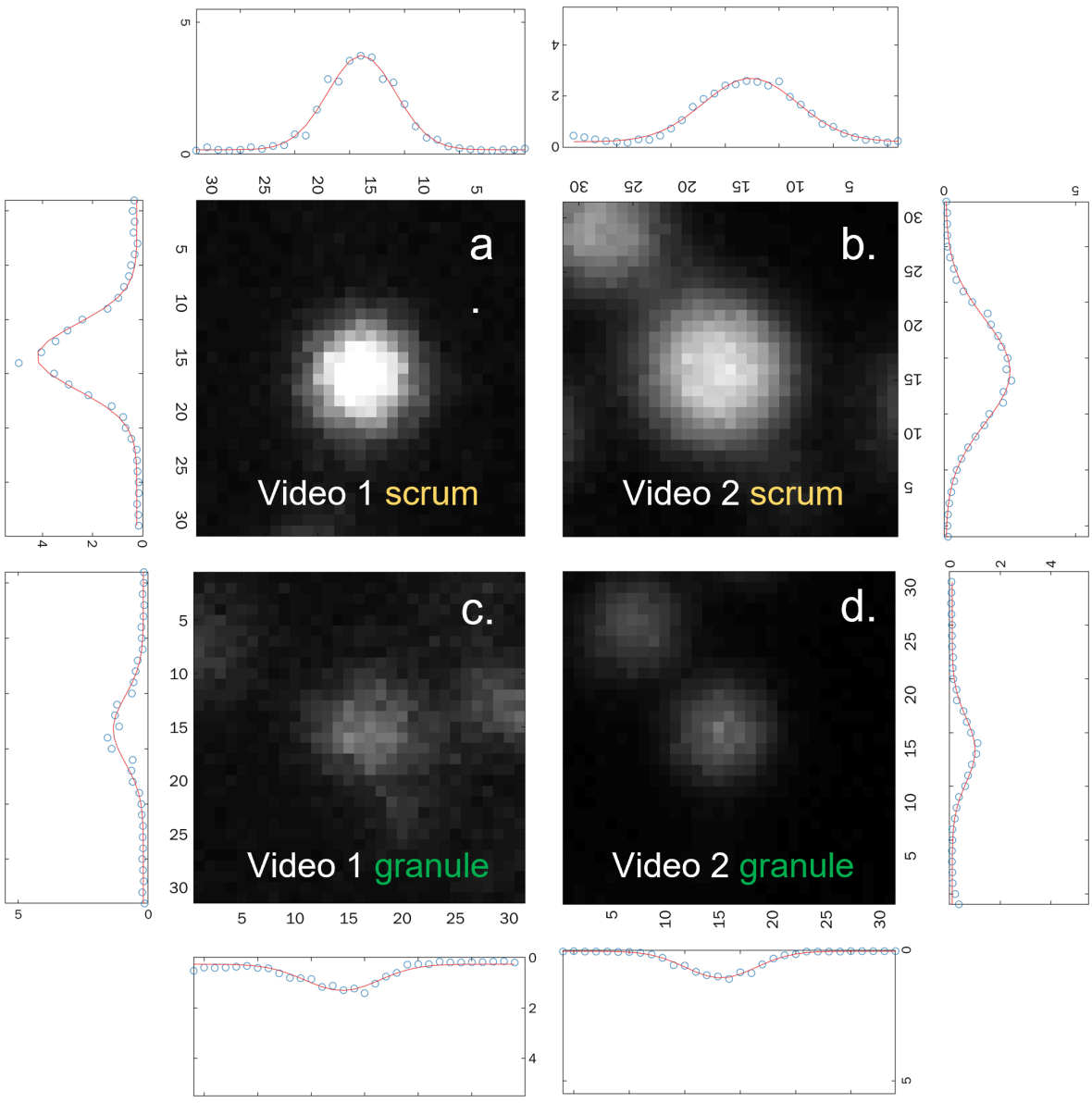

Figure 4.16: **Intensity normalized sample scrum and granule images and signal intensity profile for two videos.**

REFERENCES

[1] Ivo F Sbalzarini and Petros Koumoutsakos. Feature point tracking and trajectory analysis for video imaging in cell biology. *Journal of structural biology*, 151(2):182–195, 2005.

[2] John C Crocker and David G Grier. Methods of digital video microscopy for colloidal studies. *Journal of colloid and interface science*, 179(1):298–310, 1996.

[3] Monika Scholz, Stanislav Burov, Kimberly L Weirich, Björn J Scholz, SM Ali Tabei, Margaret L Gardel, and Aaron R Dinner. Cycling state that can lead to glassy dynamics in intracellular transport. *Physical Review X*, 6(1):011037, 2016.

[4] Kejia Chen, Bo Wang, and Steve Granick. Memoryless self-reinforcing directionality in endosomal active transport within living cells. *Nature Materials*, 14(6):589–593, 2015.

[5] Don S Lemons. An introduction to stochastic processes in physics, 2003.

CHAPTER 5

SNAPSHOT VOLUMETRIC IMAGING AND TRACKING METHODS FOR INSULIN GRANULE TRANSPORT

Reprinted with permission from Nano Lett. 2019, 19, 10, 6781–6787. Previous Postdoctoral Scholar Dr. Xiaolei Wang designed and built the instrument then developed an image reconstruction protocol using Imaris software (MTD-SEC-I approach). Biological preparation, trajectory analysis, and defocusing localization algorithm was developed by the thesis author Hannah Yi. Further analysis on localization bias and a new method for 3D single particle tracking is discussed herein and unique to this chapter.

5.1 Abstract

Accurate, precise, and rapid particle tracking in three dimensions remains a challenge; yet, its achievement will significantly enhance our understanding of living systems. We developed a multifocal microscopy (MFM) that allows snapshot acquisition of the imaging data, and an associated image processing approach, that together allow simultaneous 3D tracking of many fluorescent particles with nanoscale resolution. The 3D tracking was validated by measuring a known trajectory of a fluorescent bead with an axial accuracy of 19 nm through an image depth (axial range) of 3 μm and 4 nm precision of axial localization through an image depth of 4 μm. A second test obtained a uniform axial probability distribution and Brownian dynamics of beads diffusing in solution. We also validated the MFM approach by imaging fluorescent beads immobilized in gels and comparing the 3D localizations to their "ground truth" positions obtained from a confocal microscopy z-stack of finely spaced images. Finally, we applied our MFM and image processing approach to obtain 3D trajectories of insulin granules in pseudoislets of MIN6 cells to demonstrate its compatibility with complex biological systems. Our study demonstrates that multifocal microscopy allows rapid (video rate) and simultaneous 3D tracking of many "particles" with nanoscale accuracy and

precision in a wide range of systems, including over spatial scales relevant to whole live cells.

5.2 Introduction

Optical microscopy is one of the most common and powerful tools to study the dynamics of living systems [1–3]. Scattered light and fluorescence emission measurements can be rapid (e.g., 100 fps) while minimally perturbative and invasive. The ability to rapidly image and track particles in three dimensions is a crucial capability that if fully realized will greatly enhance studies of many open questions in biological systems[4]. For example, cells are three-dimensional objects and the transport (trafficking) of interesting targets (e.g., different proteins or vesicles) is not constrained to one plane[5, 6]. However, simultaneously obtaining all of the information for accurate 3D imaging and particle tracking, termed snapshot 3D imaging, remains a challenge. In most recent imaging technologies, such as epi-fluorescence wide-field, spinning disk confocal, and light sheet microscopies[7], only one focal plane is in focus at one time. Thus, sequential scanning is needed to obtain volumetric information. The sequential nature of 3D data acquisition at or near the limits of optical resolution results in missing information about the stochastic dynamics of particles. Also, mechanical movements associated with sequential scanning could generate systematic errors (e.g., motion blur).

Some emerging technologies that mitigate and potentially overcome these limitations include interferometric microscopy [8, 9], light field microscopy [10], light-field metasurface microscopy[11], actively laser beam steering [12, 13], point spread function (PSF) engineering[14, 15], and multi-focal plane microscopy [16, 17]. PSF engineering, which encodes axial information in the shape of the PSF with phase modulation of the electromagnetic field in the Fourier (conjugate) plane, is very powerful for simultaneously tracking the complex dynamics of several objects in biological environments. Pavani and Moerner demonstrated 10–20 nm localization precision over a depth of 2 μm in a polymer sample with the double-helix PSF [18]. Besides the double-helix PSF, many different kinds of PSFs [14] have been designed for 3D particle localization beyond the diffraction

limit. However, overlapping particle PSFs in dense samples may overwhelm this class of methods.

Multifocal plane microscopy was first demonstrated in a conventional microscope equipped with a beam splitter to image two focal planes on separate cameras [16, 17]. This method has high light collection efficiency and a large field of view but is relegated to small image depths and requires one camera per focal plane. Abrahamsson and co-workers developed an aberration-corrected multifocal microscope (MFM) as a post-sample PSF engineering methodology [15]. MFM has a practical advantage of requiring just one camera, although that comes at the expense of nontrivial optical fabrication and a reduced field of view. MFM, which combines multifocal plane microscopy and PSF engineering, is particularly promising for simultaneously obtaining all of the 3D (and 2D) information in one snapshot even for high number density samples.

Although there have been several publications using MFM, there are two main potentialities that have yet to be fully realized: (i) 3D imaging and reconstruction of extended objects and (ii) 3D in vivo particle/molecule tracking for high number density samples. To address (i) we proposed a computational MFM method to address information sparsity and image degradation to allow 3D image reconstruction [19]. To address (ii), 3D particle tracking in biological environments with MFM, requires two (new) issues to be resolved. First, single particles/molecules must be localized accurately and precisely for high number density samples. Second, the axial depth for particle/molecule tracking should ideally be comparable with the thickness of the whole cell for in vivo studies. While multifocal plane microscopy equipped with a beam splitter obtained localization precision of 11–20 nm in an image z range of 500 nm [16], these two issues have not been resolved for samples with a high number density of (fluorescently) trackable particles with MFM.

In this chapter, we demonstrate how the challenges for snapshot 3D particle tracking of high number density biological samples are addressed using MFM. We validate nanoscale accuracy and the precision of 3D particle localization/tracking with MFM with a systematically translated fluorescence bead sample. We also demonstrate the snapshot 3D measurement of the positions

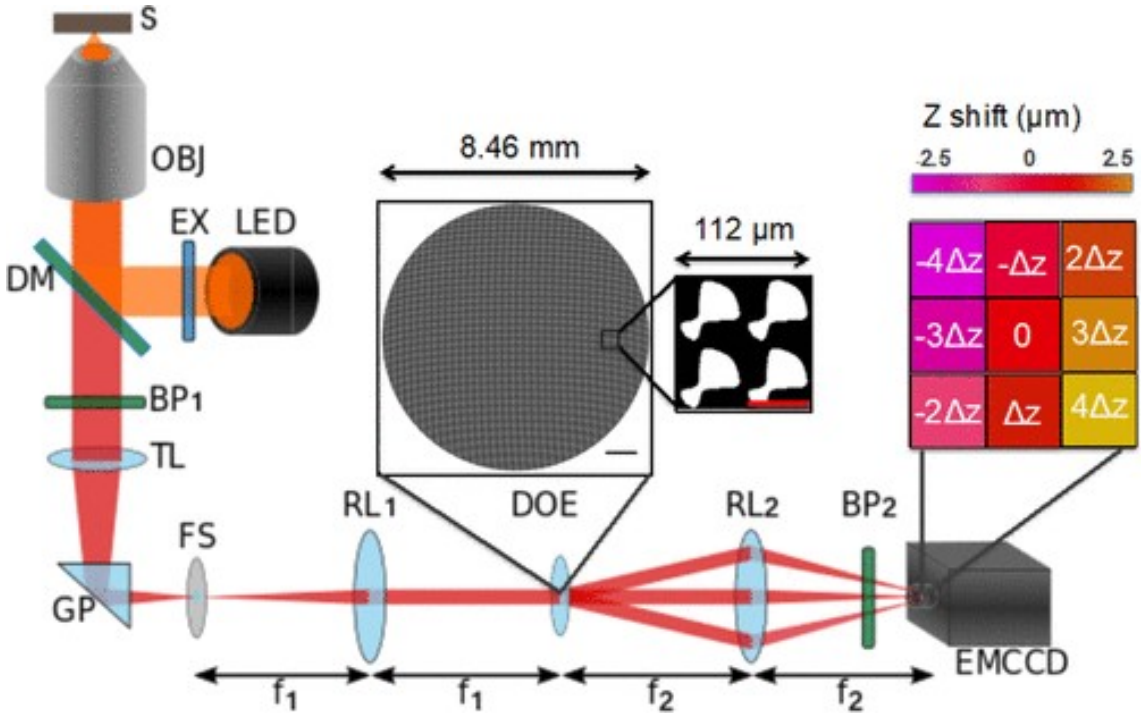

Figure 5.1: **A schematic of a multifocal microscope (MFM)**. The left-hand portion is a conventional inverted microscope (Nikon Ti). FS is a field stop that defines the measured field of view. RL1 and RL2 are relay lenses with 200 and 400 mm focal lengths, respectively. The diffractive optical element (DOE) is located at the second pupil plane, which the first relay lens generates. The resultant nine focal planes are focused on the camera with the image focal shifts indicated. We designed and fabricated the DOE; a zoomed-in view shows 4 unit cells of the DOE binary phase pattern. The scale bar (black) is 1 mm, and the scale bar (red) for four periods of the DOE is 56 μm. A schematic MFM image on the camera, showing 9 titles imaging different focal planes. Different colors represent different focal planes.

and trajectories of single fluorescence beads over a wide range of spatial and temporal scales. Finally, we show that the MFM measurement and image processing approach we describe here allows quantifying the complex 3D dynamics in biological systems, specifically the 3D transport of insulin granules in live cells. Our study demonstrates the potential of the approach to achieve new insights into cellular function.

5.3 Multifocal Microscope (MFM) Design and Image Reconstruction Method

A custom-built MFM was developed as an extension to a commercial (Nikon Eclipse Ti) inverted microscope (Figure 5.1) [20]. The microscope is housed in a temperature controlled and acoustically damped enclosure. A solid-state LED light source (Lumencor, Spectral X light engine) with highly stable output was coupled to the microscope with a liquid light guide. The excitation light was bandpass filtered (Semrock FF01-578/21-25) with a maximum power of 515 mW in the range of 568–589 nm used for wide-field illumination. Samples were mounted on a mechanical stage (Ludl 99S106-N2K-LE2, MAC5000 controller). Fluorescence emission collected by the objective (Nikon 60× 1.27 NA CFI Plan Apo water immersion, MRD07650) was separated from the excitation light by a dichroic mirror (Semrock, FF596-Di01-25 × 36) and bandpass filter (Semrock, FF02-641/75-25). An in-house fabricated metal-on-glass field stop was placed at the primary image plane, which crops the image plane to 2 mm^2 (or 33 μm^2 sample field of view) for MFM. The field stop consisted of a 200 nm Cr layer with a 2 mm square clear region deposited on a circular 25.4 mm diameter by 1 mm thick fused silica substrate (Thorlabs WG41010). A 4-f lens system relayed the image from the primary image plane to a second image plane on the detector (Andor iXon 888 EMCCD). The first lens (f = 200 mm, Thorlabs AC508-200-A) matched the focal length of the tube lens (Nikon, f = 200 mm) and generated the secondary pupil (Fourier) plane where the MFM diffractive optical element (DOE) was placed. Figure 1 shows the binary patterned DOE fabricated for the present study, which has a unit cell period of 56 μm and design focal shift, Δz, of 600 nm (see Supporting Information for details). The second lens (f = 400 mm, Thorlabs AC508-400-A) focused the fluorescence emission from the DOE onto the EMCCD detector. A second narrower bandpass filter (Semrock, FF01-620/14-25) was placed after the DOE to narrow the bandwidth of the emission light to mitigate chromatic aberration.

The DOE was characterized by imaging 200 nm diameter fluorescence beads (ThermoFisher, F8810) immobilized on a cover glass by scanning the bead sample along the z-axis with 50 nm

steps using a closed-loop piezo translator (MadCity, Nano-Z200) (see Supporting Information for details). As shown in Figure 5.6, the measured focal shift, Δz, is 650 nm, which is slightly larger than what we designed (i.e., 600 nm) because the equation used for the design is a first-order approximation of the phase description of a lens [15].

The 3D reconstructed image is obtained by post processing the MFM images using a procedure we term multi-tile deconvolution shift-error correction and interpolation (MTD-SEC-I) (See Figure 5.7 for details). We use a 3D confocal z-stack image as "ground truth" to validate 3D MFM image reconstruction by the MTD-SEC-I approach. The FARMER method [21] allows us to successfully correlate images between the confocal microscopy and MFM platforms. We calculated the standard deviation of position differences of an identical set of fluorescent beads imaged by confocal microscopy and MFM. The MFM image is reconstructed in 3D (see Figure 5.8d) with the MTD-SEC-I approach, which is described in detail in our discussion of Figure 5.7. The multi-tile deconvolution and interpolation approach using beads in the central region of the axial range measured gives a 17 nm standard deviation in axial localization (error) of the 3D MFM results from the confocal microscopy ground truth localization data.

5.4 Determining Accuracy and Precision of Axial MFM Particle Tracking

We used an immobilized 200 nm diameter fluorescent bead to evaluate the accuracy and precision of our MFM measurement and MTD-SEC-I image post-processing approach for single particle localization/tracking. The sample stage was moved in 50 nm steps with a closed-loop piezo nanopositioner (MadCity, Nano-Z200) to obtain images of fluorescent beads with different axial (z) positions. The measurement was repeated 5 times. The z position of the fluorescent beads was determined by Imaris software (Oxford Instruments) after MFM image reconstruction as described above.

Figure 5.2 shows the tracked (estimated) z locations of the bead determined over the full 5 μm range (8×0.65 μm) of the MFM measurement vs the actual position of the sample obtained

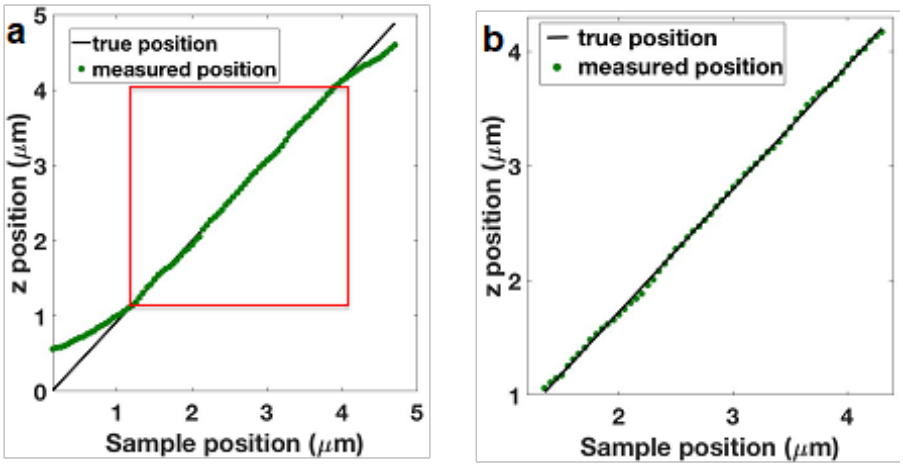

Figure 5.2: **Determining the accuracy of MFM imaging and image reconstruction by scanning an immobilized 200nm diameter fluorescent bead in the axial (z) direction.** (a) The black line shows the true position established with the piezo nano-positioner encoder, while the green points are the measured position obtained by MFM. (b) The standard deviation is 19 nm in the z range of 3 μm defined by the red square in (a).

from a 50 nm step movement of the piezo nanopositioner (determined via capacitance closed-loop feedback). The green dots in Figure 5.2a are the positions estimated from the measurement and tracking, while the black line (slope = 1.06) is the best fit to the measured data. The slope is slightly larger than 1 because of a systematic error of the MFM (See Supplementary Information). However, we use this determination of the systematic error shown in Figure 5.2 to correct measured data. Figure 5.2a shows that the accuracy deviates systematically near the ends of axial range due to missing information for particle localization. That is, as the beads approach the focal planes at the ends of the MFM axial range (i.e., tiles 1 or 9), the localization "saturates" to these limits. Therefore, the accuracy is different for different ranges of image depth as shown in Table 5.1. It can be as small as 7 nm for a small image depth of 500 nm. Still, the accuracy determined here is very consistent with that obtained by comparison with confocal ground truth as presented above.

The theoretical precision of 3D single particle localization, which is calculated using the FandPLimitTool software [22], is based on the Cramer–Rao lower bound (CRLB) and Fisher information matrix [16]. According to the CRLB, the variance of any unbiased estimator of an unknown parameter is always greater than or equal to the inverse Fisher information (matrix). The unknown

parameter is the location of the particle for the 3D location estimation problem carried out here, and the precision is the square root of the leading diagonal entry of the inverse Fisher information matrix.

Table 5.1: **Accuracy for axial particle localization for different ranges of image depth**

Image Depth (μm)	Accuracy (nm)
3	19
2	10
0.5	7

We obtained an image stack of a 200 nm diameter fluorescent bead (using 532 mW LED illumination power at 610 nm wavelength over the entire sample field of view) over a range of 10 μm along z. Together with an EMCCD exposure time of 0.5 s and EM gain of 30, this gives about 300,000 total measured photons per frame. With these experimental parameters, the theoretical precision of single particle localization with MFM is 1.7 nm over a range of 3 μm as shown in Figure 5.3b, which is better than our experimental results because the calculation only considers Poisson photon counting noise. The precision is least good at the individual MFM focal planes since there is less axial localization information at a focal plane than between them. The experimental and calculated results are consistent with each other; the theoretical axial precision can be better than 2 nm over most of the z range, while the experimental precision is in the range of 2–6 nm. The experimental conditions used here are generally consistent with the measurements performed on live cells shown below, so the estimates of accuracy and precision quantified here are expected to apply to the live cell measurements. Finally, as shown in Figure 5.3c, the precision decreases with a decreasing number of detected photons. When the number of detected photons is decreased to values more appropriate for single molecule measurements, e.g., ~1000 photons/frame/molecule (assuming that one wants to measure dynamics and spread out the photon budget over several hundred frames), the precision for axial localization degrades to approximately 30 nm.

Figures 5.2 and 5.3 show that the accuracy of axial localization has a larger error than the stan-

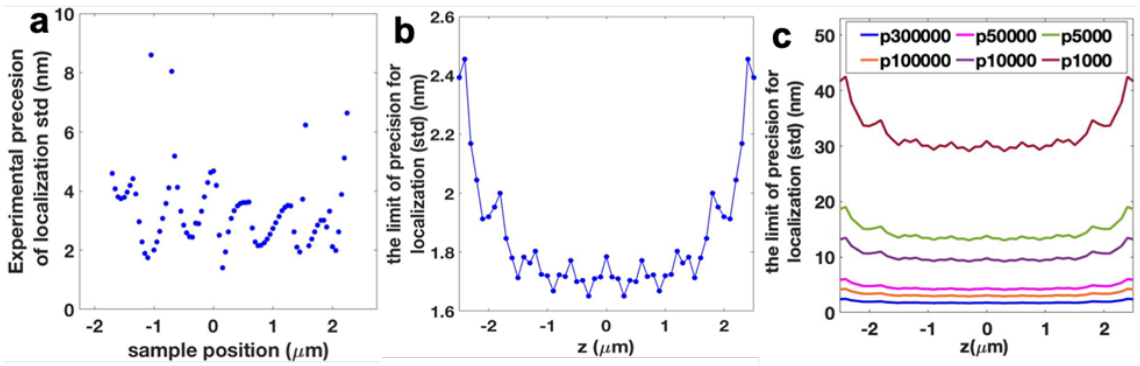

Figure 5.3: **Characterization of the precision of MFM measurements and the corresponding theoretical estimate.** (a) The precision of localization (standard deviation of 5 repeated measurements) for each z position is indicated by the blue dots. The precision of single particle localization is around 4nm over the z range of 4 μm. (b) Theoretical precision of single particle localization calculated as the Cramer-Rao lower bound over the entire 5 μm range of the MFM used in this paper.(c) Theoretical precision for conditions that would be appropriate for single particle localization experiments. The calculated results are presented in terms of the Cramer-Rao lower bound over the entire 5 μm range of the MFM with different photon budgets.

dard deviation of the multiple measurements (i.e., the precision), which indicates that the MFM system is very stable and gives reproducible results. The small systematic errors in the accuracy could arise from how well we could account for the tile-by-tile chromatic aberration with deconvolution with the cognate tile-specific PSFs and/or the alignment of the MFM optic. This is discussed at greater length in the Section 5.A.4 (particularly Figures 5.9–5.11), where we present additional results obtained with a different DOE (Δz = 418 nm). The accuracy for these additional measurements is 13 nm over a 1.3 μm axial range, which is comparable to the results obtained here with the Δz = 650 nm system.

5.5 3D Localization of Diffusing Beads

To determine whether our MFM imaging and tracking analysis does not introduce artifacts in dynamic samples, 200 nm diameter fluorescent beads (ThermoFisher, F8810) were tracked in 3D in a 50% glycerol–water solution. The specific ratio of glycerol–water solution was chosen to balance precise tracking and fast diffusion. The sample was carefully prepared to avoid air bubbles

in the 120 μm thick sample sandwiched between a cover glass and glass slide that might generate fluid flow. We imaged the 3D movement of fluorescent beads with each MFM snapshot within a depth of a 5.2 μm z range about 50 μm deep in the solution for 250 s at 20 frames per second (Video S1). The room and microscope temperatures were tightly controlled during the measurements to avoid mechanical drift.

Freely diffusing fluorescent beads moved in and out of focus of the nine z planes in the raw MFM image shown in Figure 5.4a and Video S1. Figure 5.4b shows that the distribution of bead positions along the z direction is uniform with the small amplitude periodic structure. A uniform distribution is expected for isotropic Brownian diffusion for beads far from the walls of the container. The black curve shown above the distribution is the inverse of the precision calculated with the CRLB shown in Figure 5.3b. The modulation of the axial position PDF and the "inverse" precision of localization suggest a correlation between them.

We examined the possibility of a localization bias more closely with the Δz = 418 nm DOE MFM as shown in Figures 5.12 and 5.13. If such a localization bias exists that enhances the probability of localization in regions of greater precision (i.e., between the MFM focal planes), then it should be evident as a so-called "pixel locking" error. We showed elsewhere [23, 24], that one can test for this by aggregating the localization data into a "meta-pixel" and determining if the probability density deviates from the ideal uniform distribution. Figures 5.13–5.15 show the analogous probability density function for the Δz= 418 nm MFM. The small enhancements of localization probability align with the focal planes, indicating that the localization probability is not related to localization precision.

The time averaged mean square displacement (TA-MSD) is used to characterize the motion of single presumed freely diffusing beads according to

$$\overline{\delta(\Delta, t)^2} = \frac{1}{t-\Delta}\int_0^{t-\Delta} [\vec{r}(\tau+\Delta) - \vec{r}(\tau)]^2 d\tau \tag{5.1}$$

where $r(\vec{\tau})$ is the trajectory of each single particle; Δ is the lag time, t is the total measurement

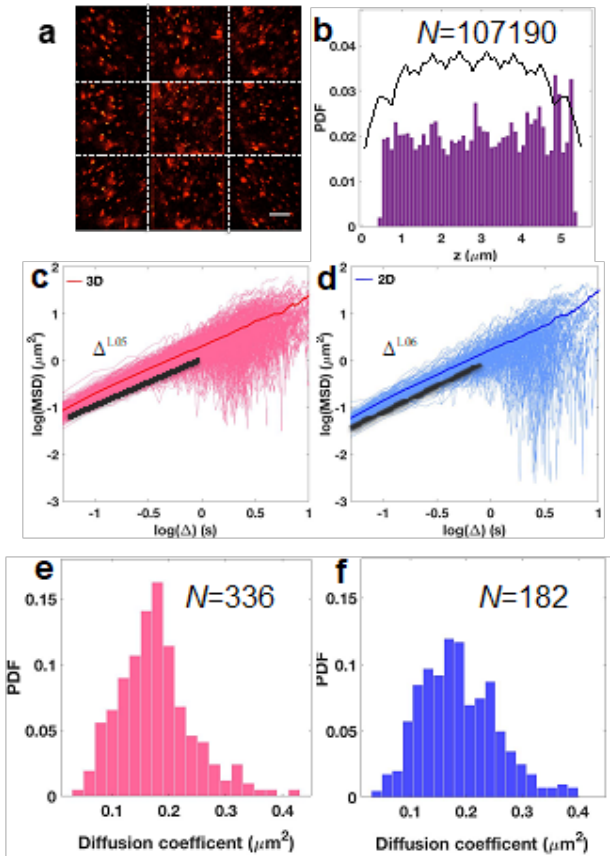

Figure 5.4: **Axial distribution and transport of 200 nm diameter fluorescence beads in 50% glycerol-water measured by MFM**. (a) A raw MFM image of 336 fluorescent beads diffusing in a 33x33 μm^2 field of view. Scale bar is 10 μm. (b) Distribution of 336 fluorescence beads along z acquired at 20 fps for 150 sec. The black curve is the inverse of the theoretical precision curve in Figure 5.3b. (c) A log-log plot of mean square displacement as a function of lag time Δ for 3D trajectories. The light pink lines are MSDs for individual beads, and the solid red line is the average MSD of the ensemble of 336 beads. The straight line paralleling the data is a visual representation of the slope for the value of the transport exponent shown (α=1.05). (d) A log-log plot of MSD as a function of lag time Δ for 2D trajectories (i.e. in the xy plane determined from the center tile of the MFM image). The light blue lines are the MSDs of individual beads, while the dark blue line is the average MSD. The straight line paralleling the data is a visual representation of the slope for the value of the transport exponent shown (α=1.06). (e) The distribution of diffusion coefficients, D, calculated from individual bead trajectories in (c) for 3D particle tracking. (f) The distribution of diffusion coefficient D calculated from individual trajectories in (d) for 2D particle tracking. Note that sharply downward curving MSD curves are the result from MSD's being calculated for lag times equal to the full temporal length of the individual bead trajectories. The slopes to characterize the transport are obtained from fitting the first 10% of the lag time and does not include these downward tails.

time for each trajectory, and the overbar indicates the average over all particles. The scaling relation between MSD and lag time [25] is

$$\overline{\delta^2} = cD\Delta^{\alpha} \tag{5.2}$$

where D is the diffusion coefficient, c is a dimension factor (c = 6 for 3D dynamics and c = 4 for 2D dynamics) and α is the transport exponent for the ensemble of particles. As the lag time, Δ, increases, the amount of data available for averaging decreases, so we only use lag times that are $\geq 10\%$ of the total measurement time of each trajectory to estimate the transport parameters D, α. Note that α characterizes the type of motion ($\alpha < 1$, subdiffusion; $\alpha = 1$ Brownian diffusion; $\alpha > 1$ superdiffusive), while D gives its magnitude at lag time log (Δ) = 0.

Mean square displacement analysis was performed for both 3D and 2D trajectories; the latter are from the center tile. As shown in Figure 5.4c,d, the ensemble MSD for 2D and 3D motion gives $\alpha \approx 1$, consistent with Brownian diffusion. Analogous results are given in Figure 5.13 for measurements of bead diffusion with the Δz = 418 nm DOE MFM, where the slope $\alpha = 0.993$. Figure 5.4e,f shows the distribution of diffusion coefficients for 3D and 2D particle tracking of 200 nm fluorescent beads that are calculated with individual trajectories shown in Figure 5.4c,d. The determined diffusion coefficients are $0.17 \pm 0.02\ \mu m^2$/s and $0.18 \pm 0.04\ \mu m^2$/s for 3D and 2D motion, which are consistent with theoretical results using the Stokes–Einstein equation for the viscosity and bead size used here [12]. Therefore, these experiments further validate 3D particle tracking of dynamic particles of the MFM measurement and image analysis method we developed for many (>300) simultaneously measured fluorescent particles.

5.6 3D MFM Snapshot Tracking of Insulin Granules in Live Cells

We demonstrate snapshot 3D particle tracking with MFM in a complicated biological system by imaging and tracking insulin granules in clusters of MIN6 cells derived from pancreatic β-cells. Insulin, a small peptide (hormone), regulates cellular uptake of glucose from the bloodstream.

Defects in insulin release (secretion) upon stimulation, including defective transport, can play a role in disease [26, 27]. β-Cells package insulin into vesicles (termed granules) that are transported along microtubules to docking sites in the cellular membrane, allowing insulin secretion upon suitable stimulation. Therefore, understanding intracellular insulin granule transport is essential not only to understand insulin secretion and organismal glucose regulation but also to investigate diagnostics and therapeutics [28].

We imaged the 3D movement of insulin granules with snapshot 3D MFM data acquisition within a 5.2 μm depth (slab) from clusters of MIN6 cells for 100s at 10 frames per second (Video S2). We used CRISPR-Cas9 to tag mCherry to insulin for high efficiency labeling [29]. Monolayer grown MIN6 cells were trypsinized and suspended in growth media on untreated Petri dishes to form pseudoislets [30], which are three-dimensional clusters of MIN6 cells that mimic the spatial arrangement of β-cells in islets of Langerhans. The suspended cells were grown for 1–2 weeks at 37 °C and 5% CO2 with media replacement every 2–3 days. The red dots in Figure 5.5 are a 3D image reconstruction of the granules in a pseudoislet cluster of MIN6 cells. The two side panels are the xz and yz image projections that clearly show that different insulin granules have different z positions. Figure 5.5b shows 3D trajectories of insulin granules. The trajectories demonstrate that the movement of insulin granules is three-dimensional rather than two-dimensional. In comparison with confocal microscopy studies we have performed for granules in MIN6 cells, the trajectories do not abruptly end when granules move beyond the small (¡1 μm) z range associated with confocal microscopy. The individual MSDs for 375 insulin granules (Figure 5.5c) and the broad distribution of the diffusion coefficient derived from individual MSDs (Figure 5.5d) indicate heterogeneous motion of these insulin granules. This result demonstrates the potential of MFM for quantitative measurement of complex 3D dynamics in live systems. Detailed analysis of these trajectories will be presented elsewhere.

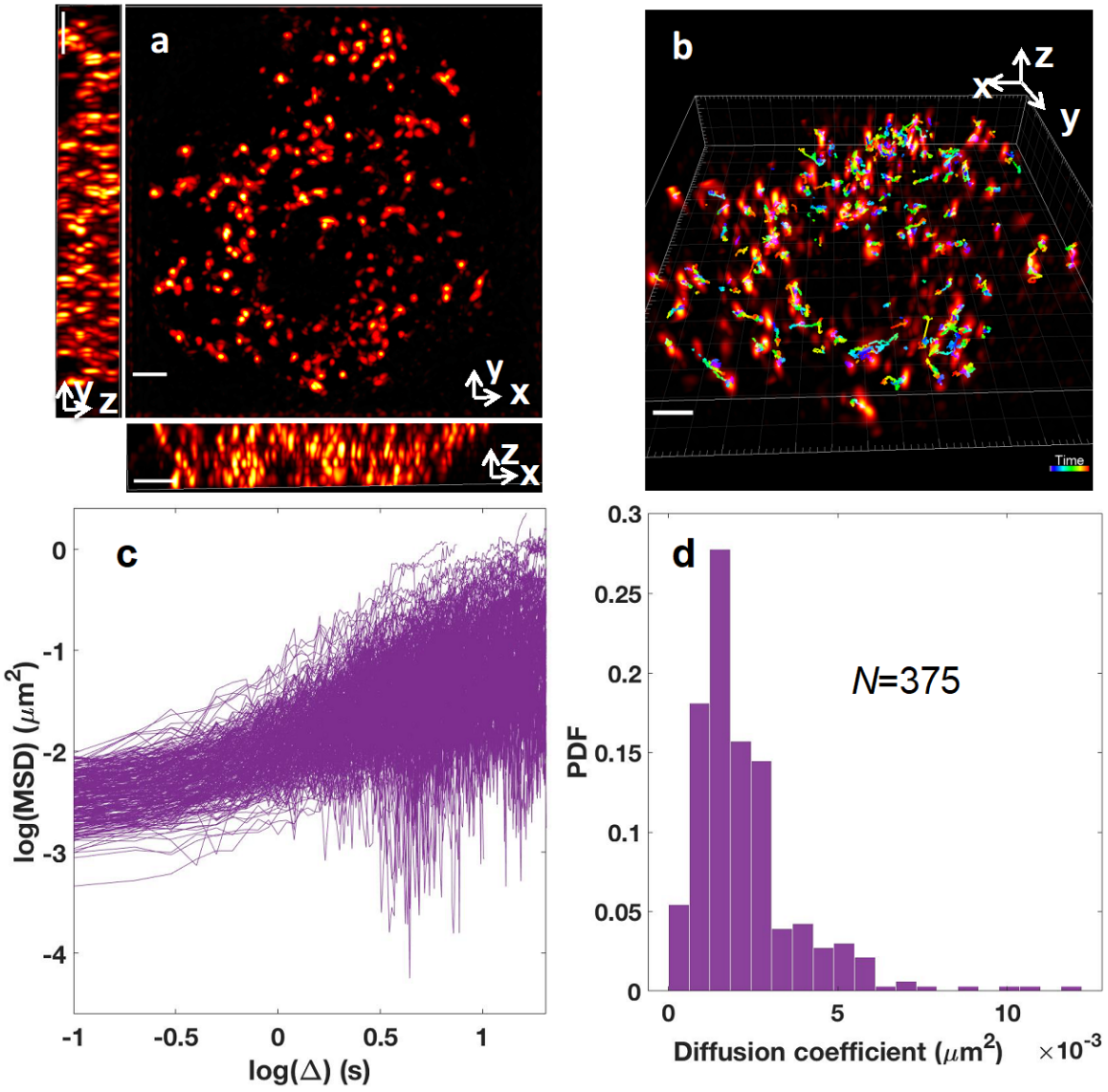

Figure 5.5: **3D dynamics of insulin granules in live MIN6 cells obtained with MFM.** (a) A reconstructed 3D image of mCherry-labeled insulin granules in pseudo-islets of MIN6 cells (scale bar is 3 μm). Approximately 8 cells are imaged in this slab of the pseudo-islet. The main portion of (a) is the xy projection. The two rectangular panels (right and bottom) are xz and yz projections, respectively. (b) 3D color-coded trajectories of insulin granules in a pseudo-islet of MIN6 cells shown in 5.5a. Scale bar is 3 μm. The color bar denotes time, in seconds; the total time is 100s and MFM images were acquired at 10 Hz. (c) The purple curves are the MSDs for 375 insulin granules in MIN6 cells shown in Figure 5.5a. (d) The distribution of diffusion coefficients, D, calculated from individual bead trajectories in (c). Note that the MSD's are nonlinear in the log-log representation of (c) and also spread, suggesting a wide distribution of α values. This is in contrast to the Brownian diffusion and narrow distribution of α's shown in Figure 5.4.

5.7 Conclusion

We presented a new approach for snapshot 3D particle tracking by multifocal microscopy (MFM) combined with an approach for 3D image reconstruction that is suitable for 3D particle tracking. We characterized the accuracy and precision of the MFM imaging and data analysis approach through a series of control experiments. Comparative measurements of fluorescent beads embedded in agarose gel obtained by confocal microscopy and MFM give an axial location error of 17 nm vs the confocal "ground truth". The accuracy and precision of 3D localization can be determined for single particle tracking. We tested our MFM system and imaging processing with axially scanned immobilized 200 nm fluorescence beads immobilized to a moving sample stage, showing that the accuracy of axial localization is 7 nm in a 500 nm range and 19 nm in a 4 μm z range. The precision of axial localization is 2–4 nm in a 4 μm z range. The precision is consistent with the Fisher information matrix (FIM) and the Cramer–Rao lower bound (CRLB) of MFM for our experimental conditions. The 3D MFM tracking of fluorescence beads freely diffusing in 50% glycerol–water manifests Brownian movement of beads, which further demonstrates the reliability of MFM for 3D particle tracking with high accuracy and precision.

These controls enabled us to confidently track the 3D motion of crowded samples, such as fluorescently labeled insulin-containing granules in live cells, undergoing complex motions, with nanometer-scale resolution. The 3D intracellular insulin granule tracking demonstrates that MFM addresses the challenge of simultaneity of data acquisition with fast imaging speed and accurate 3D image analysis for tracking objects present in high density in complex live cell environments.

Studies of the 3D dynamics of objects (molecules, vesicles, organelles) in complex and heterogeneous live systems pose rigorous requirements on simultaneity of image acquisition, imaging speed, localization precision, and density of objects to be imaged. Experiments of this type require careful attention to the trade-offs between image depth and localization precision. MFM and a suitable image processing approach we introduce allowed us to successfully eliminate chromatic aberration and background noise to obtain high accuracy and precision 3D tracking of dense

particle samples; many particles are simultaneously tracked with nanometer-scale accuracy and precision at speeds limited by the camera readout time (frame rate) over a wide range of spatial and temporal scales. Due to its compatibility with standard microscopes, other super resolution methods, and excellent imaging performance, MFM-based 3D particle tracking will be a powerful tool for deducing complex 3D dynamics from single molecules to small cellular organelles.

REFERENCES

[1] BC Chen, WR Legant, K Wang, L Shao, and DE Milkie. Davidson, 624 mw. *Janetopoulos, C., Wu, XS, Hammer, JA, Liu, Z., English, BP*, 625.

[2] Robert S Fischer, Yicong Wu, Pakorn Kanchanawong, Hari Shroff, and Clare M Waterman. Microscopy in 3d: a biologist's toolbox. *Trends in cell biology*, 21(12):682–691, 2011.

[3] Na Ji, Hari Shroff, Haining Zhong, and Eric Betzig. Advances in the speed and resolution of light microscopy. *Current opinion in neurobiology*, 18(6):605–616, 2008.

[4] Lexy von Diezmann, Yoav Shechtman, and WE Moerner. Three-dimensional localization of single molecules for super-resolution imaging and single-particle tracking. *Chemical reviews*, 117(11):7244–7275, 2017.

[5] Guy A Rutter and Elaine V Hill. Insulin vesicle release: walk, kiss, pause... then run. *Physiology*, 21(3):189–196, 2006.

[6] D Zenisek, JA Steyer, and W Almers. Transport, capture and exocytosis of single synaptic vesicles at active zones. *Nature*, 406(6798):849–854, 2000.

[7] Philipp J Keller, Annette D Schmidt, Joachim Wittbrodt, and Ernst HK Stelzer. Reconstruction of zebrafish early embryonic development by scanned light sheet microscopy. *science*, 322(5904):1065–1069, 2008.

[8] Gleb Shtengel, James A Galbraith, Catherine G Galbraith, Jennifer Lippincott-Schwartz, Jennifer M Gillette, Suliana Manley, Rachid Sougrat, Clare M Waterman, Pakorn Kanchanawong, Michael W Davidson, et al. Interferometric fluorescent super-resolution microscopy resolves 3d cellular ultrastructure. *Proceedings of the National Academy of Sciences*, 106(9):3125–3130, 2009.

[9] Itay Gdor, Xiaolei Wang, Matthew Daddysman, Yuval Yifat, Rosemarie Wilton, Mark Hereld, Marie-Françoise Noirot-Gros, and Norbert F Scherer. Particle tracking by repetitive phase-shift interferometric super resolution microscopy. *Optics Letters*, 43(12):2819–2822, 2018.

[10] Robert Prevedel, Young-Gyu Yoon, Maximilian Hoffmann, Nikita Pak, Gordon Wetzstein, Saul Kato, Tina Schrödel, Ramesh Raskar, Manuel Zimmer, Edward S Boyden, et al. Simultaneous whole-animal 3d imaging of neuronal activity using light-field microscopy. *Nature methods*, 11(7):727–730, 2014.

[11] Aaron L Holsteen, Dianmin Lin, Isaac Kauvar, Gordon Wetzstein, and Mark L Brongersma. A light-field metasurface for high-resolution single-particle tracking. *Nano letters*, 19(4):2267–2271, 2019.

[12] Manuel F Juette and Joerg Bewersdorf. Three-dimensional tracking of single fluorescent particles with submillisecond temporal resolution. *Nano letters*, 10(11):4657–4663, 2010.

[13] Shangguo Hou, Xiaoqi Lang, and Kevin Welsher. Robust real-time 3d single-particle tracking using a dynamically moving laser spot. *Optics letters*, 42(12):2390–2393, 2017.

[14] Yoav Shechtman, Steffen J Sahl, Adam S Backer, and William E Moerner. Optimal point spread function design for 3d imaging. *Physical review letters*, 113(13):133902, 2014.

[15] Sara Abrahamsson, Jiji Chen, Bassam Hajj, Sjoerd Stallinga, Alexander Y Katsov, Jan Wisniewski, Gaku Mizuguchi, Pierre Soule, Florian Mueller, Claire Dugast Darzacq, et al. Fast multicolor 3d imaging using aberration-corrected multifocus microscopy. *Nature methods*, 10(1):60–63, 2013.

[16] Sripad Ram, Prashant Prabhat, Jerry Chao, E Sally Ward, and Raimund J Ober. High accuracy 3d quantum dot tracking with multifocal plane microscopy for the study of fast intracellular dynamics in live cells. *Biophysical journal*, 95(12):6025–6043, 2008.

[17] Erdal Toprak, Hamza Balci, Benjamin H Blehm, and Paul R Selvin. Three-dimensional particle tracking via bifocal imaging. *Nano letters*, 7(7):2043–2045, 2007.

[18] Sri Rama Prasanna Pavani, Michael A Thompson, Julie S Biteen, Samuel J Lord, Na Liu, Robert J Twieg, Rafael Piestun, and William E Moerner. Three-dimensional, single-molecule fluorescence imaging beyond the diffraction limit by using a double-helix point spread function. *Proceedings of the National Academy of Sciences*, 106(9):2995–2999, 2009.

[19] Kuan He, Zihao Wang, Xiang Huang, Xiaolei Wang, Seunghwan Yoo, Pablo Ruiz, Itay Gdor, Alan Selewa, Nicola J Ferrier, Norbert Scherer, et al. Computational multifocal microscopy. *Biomedical Optics Express*, 9(12):6477–6496, 2018.

[20] Xiaolei Wang, Xiang Huang, Itay Gdor, Matthew Daddysman, Hannah Yi, Alan Selewa, Theresa Haunold, Mark Hereld, and Norbert F Scherer. Snapshot 3d tracking of insulin granules in live cells. In *Three-Dimensional and Multidimensional Microscopy: Image Acquisition and Processing XXV*, volume 10499, pages 33–39. SPIE, 2018.

[21] Toan Huynh, Matthew K Daddysman, Ying Bao, Alan Selewa, Andrey Kuznetsov, Louis H Philipson, and Norbert F Scherer. Correlative imaging across microscopy platforms using the fast and accurate relocation of microscopic experimental regions (farmer) method. *Review of Scientific Instruments*, 88(5):053702, 2017.

[22] Jerry Chao, Sripad Ram, E Sally Ward, and Raimund J Ober. Ultrahigh accuracy imaging modality for super-localization microscopy. *Nature methods*, 10(4):335–338, 2013.

[23] Yuval Yifat, Nishant Sule, Yihan Lin, and Norbert F Scherer. Analysis and correction of errors in nanoscale particle tracking using the single-pixel interior filling function (spiff) algorithm. *Scientific reports*, 7(1):1–10, 2017.

[24] Stanislav Burov, Patrick Figliozzi, Binhua Lin, Stuart A Rice, Norbert F Scherer, and Aaron R Dinner. Single-pixel interior filling function approach for detecting and correcting errors in particle tracking. *Proceedings of the National Academy of Sciences*, 114(2):221–226, 2017.

[25] SM Ali Tabei, Stanislav Burov, Hee Y Kim, Andrey Kuznetsov, Toan Huynh, Justin Jureller, Louis H Philipson, Aaron R Dinner, and Norbert F Scherer. Intracellular transport of insulin granules is a subordinated random walk. *Proceedings of the National Academy of Sciences*, 110(13):4911–4916, 2013.

[26] Erica Chevalier-Larsen and Erika LF Holzbaur. Axonal transport and neurodegenerative disease. *Biochimica et Biophysica Acta (BBA)-Molecular Basis of Disease*, 1762(11-12):1094–1108, 2006.

[27] James E Rothman. The machinery and principles of vesicle transport in the cell. *Nature medicine*, 8(10):1059–1062, 2002.

[28] Bo Wang, Stephen M Anthony, Sung Chul Bae, and Steve Granick. Anomalous yet brownian. *Proceedings of the National Academy of Sciences*, 106(36):15160–15164, 2009.

[29] Sindhu Rajan, Stefani C Eames, Soo-Young Park, Christine Labno, Graeme I Bell, Victoria E Prince, and Louis H Philipson. In vitro processing and secretion of mutant insulin proteins that cause permanent neonatal diabetes. *American Journal of Physiology-Endocrinology and Metabolism*, 298(3):E403–E410, 2010.

[30] Azazul Chowdhury, Venkata P Satagopam, Levon Manukyan, Konstantin A Artemenko, Yi Man Eva Fung, Reinhard Schneider, Jonas Bergquist, and Peter Bergsten. Signaling in insulin-secreting min6 pseudoislets and monolayer cells. *Journal of proteome research*, 12(12):5954–5962, 2013.

5.A Appendix: Supporting Information

5.A.1 Diffractive optical element fabrication and characterization

The DOE for multifocal microscopy (MFM) was designed to create a 3x3 array of sub-images (tiles) that have a focal shift of 600 nm [1, 2]. The binary patterned DOE fabricated for the present study has a unit cell period of 56 μm and design focal shift, Δz, of 600nm. Our DOE is designed for a (fluorescence) wavelength of 610nm with emission light distributed evenly and efficiently (67%) among the nine tiles. We fabricated the DOE in-house on a 5 mm thick 25mm diameter UV fused silica substrate (WG41050, Thorlabs). The fused silica window was cleaned with acetone, isopropyl alcohol and distilled water, then spin-coated with a 1.5 μm thick layer of AZ1512 photoresist (Shipley). A laser writer (Heidelberg MLA150) exposed the desired pattern at 0.5 μm pixel resolution in the photoresist (405 nm laser at a dose of 150 mJ/cm^2). The photoresist was developed in AZ-300 MIF developer (Integrated Micro Materials) for 20 s. The window with the pattern written in photoresist was etched in a reactive ion etcher (RIE, Oxford Instruments). The glass substrate was etched to a depth of 680nm for the design wavelength of 610nm using Ar gas (25 standard cubic centimeters per minute (sccm)) and CHF_3 (25 sccm), and 200 W RF power for about 28 min. The photoresist remaining after etching was stripped with acetone in an ultrasonic bath. The etching depth and surface roughness of the DOE were measured with contact profilometry (Bruker Dektak XT-S profilometer). All fabrication steps were completed at the Pritzker Nanofabrication Facility and the Searle Cleanroom Facility at the University of Chicago.

The DOE lateral imaging and axial focal properties were characterized by imaging 200 nm diameter fluorescence beads (ThermoFisher, F8810) immobilized on a cover glass; the bead sample was scanned along the z-axis in 50 nm steps using a closed-loop piezo translator (MadCity, Nano-Z200). The beads were successively focused in each consecutive tile of the MFM image in this z stack (see video 3 in the Supporting Information). Figure 5.6a and Figure 5.6b show the bead focused at tile #2 and #8 at two different z positions of the bead-on-coverslip sample.

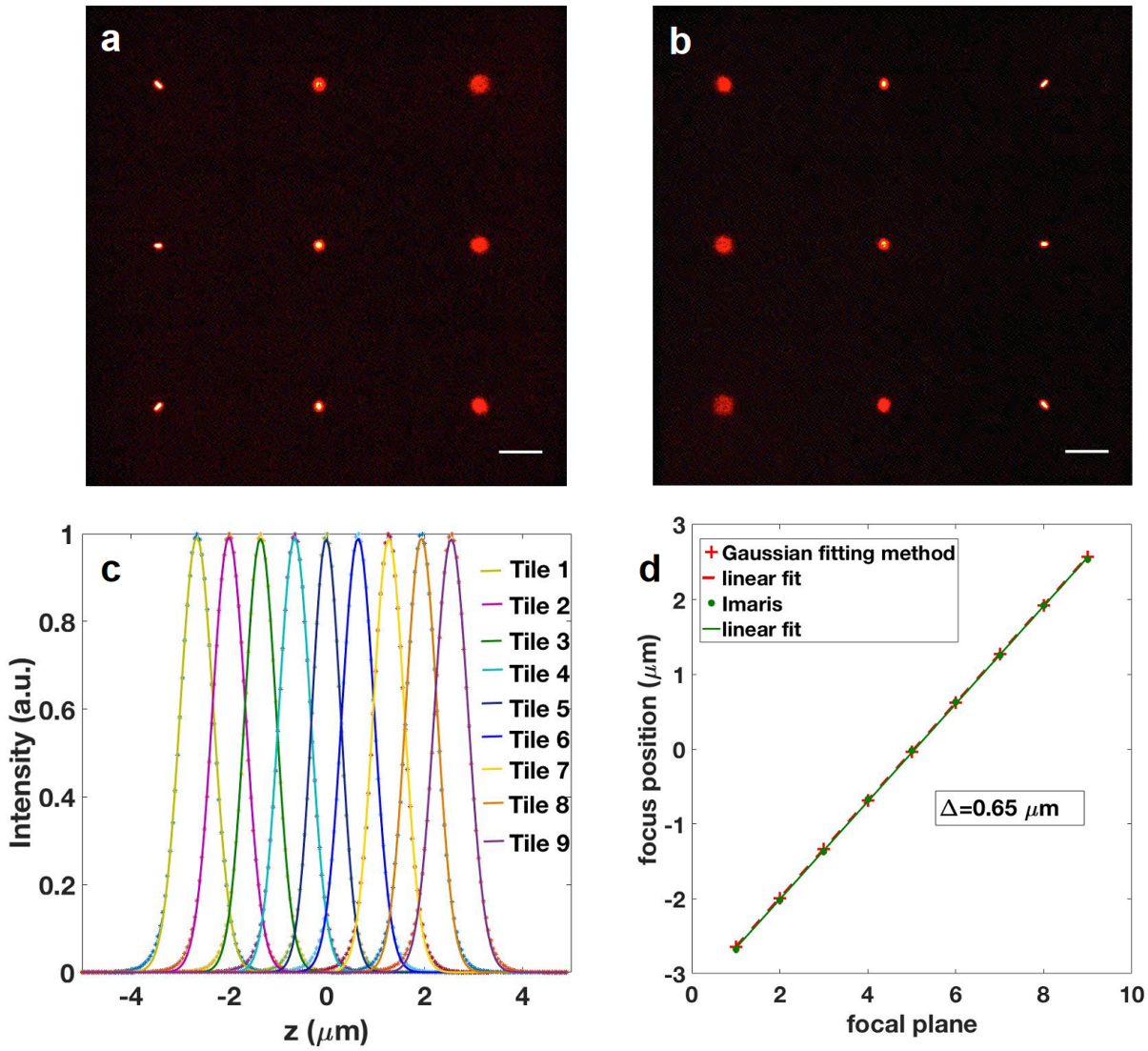

Figure 5.6: **Characterization of the diffractive optical element (DOE).** (a) and (b) are MFM images of a single fluorescent bead at two different z positions. These raw MFM images show the bead focused at tile 2 (a) and 8 (b), respectively. Scale bar (white) is 10 μm with a 33x33 μm^2 field of view. (c) Gaussian curves fitted to the fluorescence signal of a 200 nm diameter bead that was scanned along the z-axis with a closed-loop piezo translation stage (MadCity, Nano-Z200). Each curve is the signal from each individual tile for the sequence of z positions of the stage and sample. (d) Plot of the focus position of each tile obtained from the fitted centroids of the focal shift curves from Fig. (c) (red crosses) and Imaris (green dots). The linear fit has a slope of Δz=650 nm/tile or per focal plane, which is the experimentally determined focal shift between tiles. The goodness of fit substantiates that the focal shift is constant for the 9 tiles (planes) of the MFM DOE. Note the magnitude of the focal shift is slightly larger than the design target due to the first order lens approximation used in the design

The particular chromatic aberrations present in each tile were removed by deconvolution with the corresponding 3D point spread functions (PSFs) of each tile using Huygens (Scientific Volume Imaging, Hilversum, The Netherlands). We used two image processing methods to determine the focal shift: (i) 1D Gaussian fitting for the z position of a fluorescent bead; and (ii) 3D localization using Imaris software (Oxford Instruments). Figure 5.6c shows the normalized fluorescence intensity distributions of the bead that appear successively in-focus in each of the nine tiles, which were fitted to Gaussian curves in z. The positions of best focus for each tile are shown in Figure 5.6d as red crosses and green dots, respectively, for these two methods. It is clear that there is negligible difference between the results using these two methods, which demonstrates the accuracy of focal shift determination of our image processing method. The slope of the linear fitted line establishes the focal shift, Δz, to be 650 nm. This focal shift is slightly larger than what we designed for (i.e., 600 nm) because the equation used for the design is a first order approximation of the transverse phase description (function) of a lens 1.

5.A.2 MFM Image Reconstruction

Reconstructing a 3D image from the set of nine 2D multifocal images involves a series of steps: (i) arranging the nine focal plane images in order of the focal shift; (ii) aligning them laterally using a flood image; (iii) deconvolving each image with the corresponding measured point spread function using Huygens; (iv) aligning them into a 3D stack with a transformation matrix approach that was calibrated using a set of 200 nm fluorescent beads (ThermoFisher, F8810) immobilized on a coverslip; and (v) interpolating the 3D stack of 9 planes into a 3D stack with 81 planes. We term this procedure multi-tile deconvolution shift-error correction and interpolation (MTD-SEC-I). A flood image was obtained with a fluorescent plastic slide (Chroma) with an excitation wavelength of 575 nm and the same emission filters as for the mCherry fluorescent protein imaging. This measurement allows determining the borders of the 9 tiles using a threshold of the flood image.

Figure 5.7 is an MFM image of three 200 nm diameter fluorescent beads obtained using 610 nm

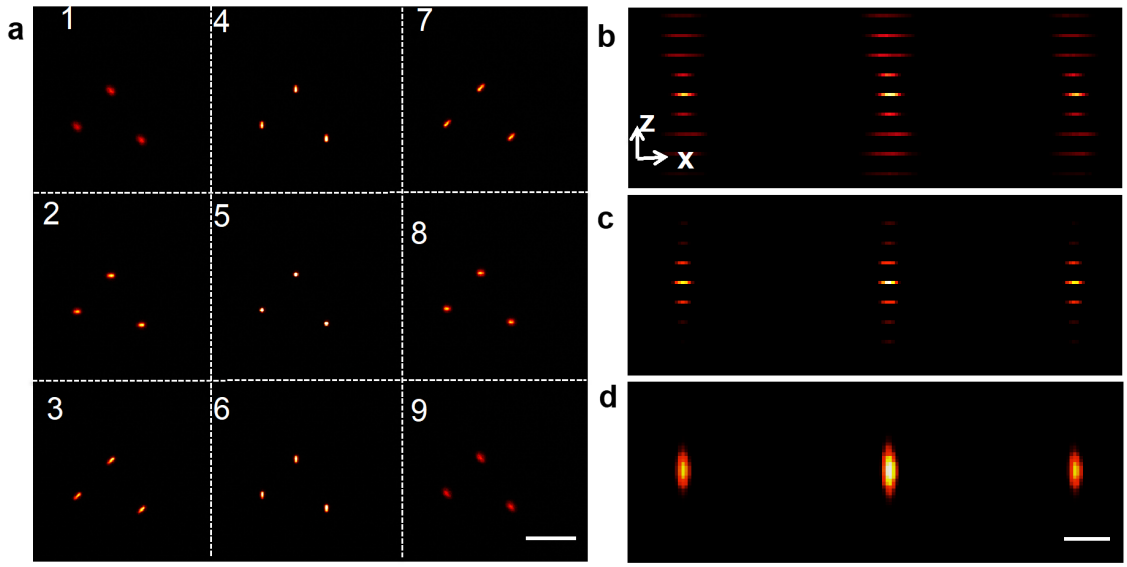

Figure 5.7: **Details of image processing to create a 3D MFM image.** (a) A single frame (image) of MFM data (9 tiles or focal planes) of three 200nm fluorescent beads viewed in the xy plane perspective. Scale bar is 10 μm. (b) The xz projection of the raw data. (c) The xz projection of the MFM data processed by deconvolution and shift error correction. (d) The xz projection of the MFM data processed with multi-tile deconvolution and shift error correction and interpolation (MTD-SRC-I). Scale bar is 2 μm.

LED illumination and the same filters as for mCherry imaging (see below). Figure 5.7b shows side-on planarized projections of the 9 focal plane-shifted images following coarse alignment based on the flood image. It is clear that there is an x, y shift between different focal planes and significant achromatic aberration. The point spread function (PSF) that removes the achromatic aberration with deconvolution was obtained with 100 nm fluorescent beads (ThermoFisher, F8801). A z-stack of MFM images is measured by scanning the bead sample along the z-axis in 50 nm steps using a closed-loop piezo translator. In this z stack, the beads successively come into focus in each MFM image tile. Nine 3D PSFs, one for each tile, were obtained with PSF distiller in Huygens. Chromatic aberration and the out-of-focus background were removed for each focal plane (i.e., for each different tile) by deconvolution with the appropriate (one of nine) 3D PSFs using Huygens. The positions of maximum intensity of the three 200 nm fluorescent beads in each tile (different focal planes) were used to determine the transformation matrix for fine alignment; i.e.,

by translation, rotation and scaling [3]. Finally, the nine deconvoluted focal planes were accurately superimposed using the transformation matrix as shown in Figure 5.7c. New data points are constructed by interpolation between the nine focal planes resulting in continuous looking 3D images of the fluorescent beads (Fig. 5.7d).

The elimination of chromatic aberration by PSF deconvolution of each individual tile, as opposed to using a second diffractive optical element and multifaceted prism for this purpose, is discussed in detail elsewhere [4].

5.A.3 Validation of MFM 3D image reconstruction

To validate MFM 3D image reconstruction by the MTD-SEC-I approach, we use a 3D confocal z-stack image as "ground truth". The FARMER method [3] allows us to successfully correlate images across the confocal microscopy and MFM platforms. We calculated the standard deviation for position differences of identical sets of fluorescent beads imaged by confocal microscopy and MFM. Confocal microscopy was performed using a Yokogawa W1 spinning disk confocal with a 100x oil immersion objective (Nikon 100x NA 1.45, MRD01905) with an EMCCD array detector (Andor iXon Ultra 888). The objective was moved in 50 nm steps to obtain confocal z stacks.

Figure 5.8a shows a 3D deconvolved confocal image of 200nm diameter fluorescent beads (ThermoFisher, F8810) embedded in 2% agarose gel. Figure 5.8b is the xz projection of the confocal data. Figure 5.8c shows the reconstructed MFM image with 3D deconvolution using a single 3D PSF generated from one MFM frame (the center tile is in focus). Comparing the bead axial positions to the positions of the identical beads imaged and localized from confocal z-stacks gives a large standard deviation of 70 nm in axial particle localization (for the 3D deconvolved MFM data). This large error of localization is paralleled by a significant distortion of the shape of the beads located near the axial limits of the 3D deconvolved MFM image volume. This result demonstrates that 3D deconvolution with a single 3D PSF does not work for MFM reconstruction since shift invariance is not satisfied by the 3D PSF because of different chromatic aberration in

each MFM tile.

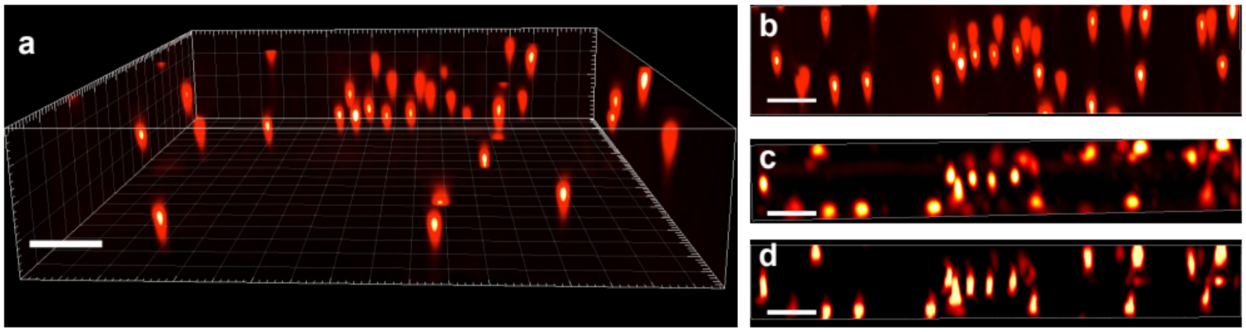

Figure 5.8: **Correlated images between identical regions of the same bead-in-gel sample measured by confocal microscopy (ground truth) and MFM.** (a) A 3D confocal image of 200 nm fluorescent beads in an agarose gel. Scale bar is 3 μ m. (b) is the xz projection of the confocal data. (c) The xz projection of the MFM data processed with 3D deconvolution with a single PSF and interpolation. (d) The xz projection of the MFM data processed with the nine multi-tile PSF deconvolution and interpolation (MTD-SEC-I) approach.

By contrast, Figure 5.8d shows that the MFM image is accurately reconstructed in 3D with the MTD-SEC-I approach described in detail in our discussion of Figure 5.7. The axial localization (error) using the multi-tile deconvolution and interpolation approach is 17 nm standard deviation, which is determined by again comparing with the confocal microscopy "ground truth" localization data.

5.A.4 Fabrication and characterization of a DOE with 400 nm focal shift

We fabricated and characterized a second DOE for multifocal microscopy (MFM) to further confirm the process described above and to give consideration to possible trade-offs of localization error vs. extent of axial range that is useful for 3D localization and tracking. The details of design and fabrication are the same as described above; the second DOE was designed to create a 3x3 array of sub-images (tiles) that have a focal shift of 400 nm [1, 2] and for a (fluorescence) wavelength of 610 nm. With careful alignment, the emission light was distributed evenly and efficiently (67%) among the nine tiles. All fabrication steps were as described above and completed at the Pritzker Nanofabrication Facility and the Searle Cleanroom Facility at the University of Chicago.

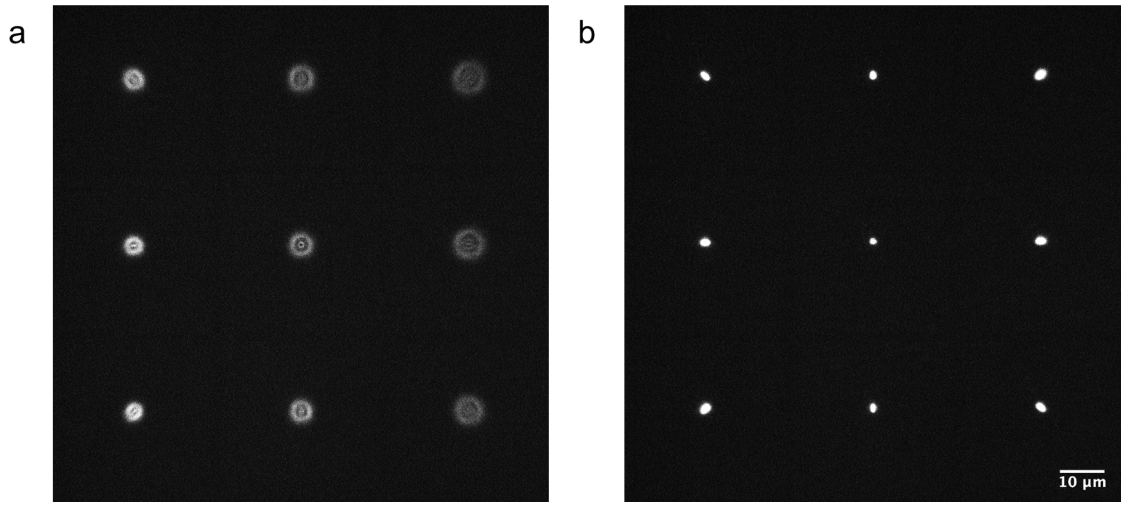

Figure 5.9: **Point spread function measured using a 100 nm diameter red (610 nm emission) fluorescent bead.** Snapshots taken from axial positions (a) out-of-focus and (b) in-focus at the center tile. The tile ordering starts at the bottom left tile (up the column) to the top right tile. This order represents the focal plane closest to the coverslip to the focal place furthest from the coverslip that forms the bottom of the sample cell and the inverted optical microscope.

The DOE lateral imaging and axial focal properties were characterized by imaging 100 nm diameter fluorescence beads (ThermoFisher, F8810) immobilized on a cover glass by scanning the bead sample along the z-axis in 100 nm steps using the same closed-loop piezo translator (MadCity, Nano-Z200) in the same solution used for studies of diffusing bead samples (i.e., 50% glycerol:water). A single bead used for PSF determination was successively focused in each consecutive tile of the MFM image in this z stack (see video 4 in the Supporting Information; imaging parameters; 100 nm focal shift, 0.5 Hz frame rate, 100x gain on the EMCCD detector). Figure 5.9a and Figure 5.9b show the MFM image defocused slightly above the bead (i.e. focused in the solution; the bead is below the focal plane) and the bead in focus at the center tile. The particular chromatic aberrations present in each tile were removed by deconvolution with the corresponding 3D point spread functions (PSFs) of each tile using Huygens (Scientific Volume Imaging, Hilversum, The Netherlands).

Similar to the analysis for Figure 5.6, we used 1D Gaussian fitting to determine the z position of fluorescent beads (200 nm dia.) in each tile. We measured three 200 nm diameter fluorescent beads,

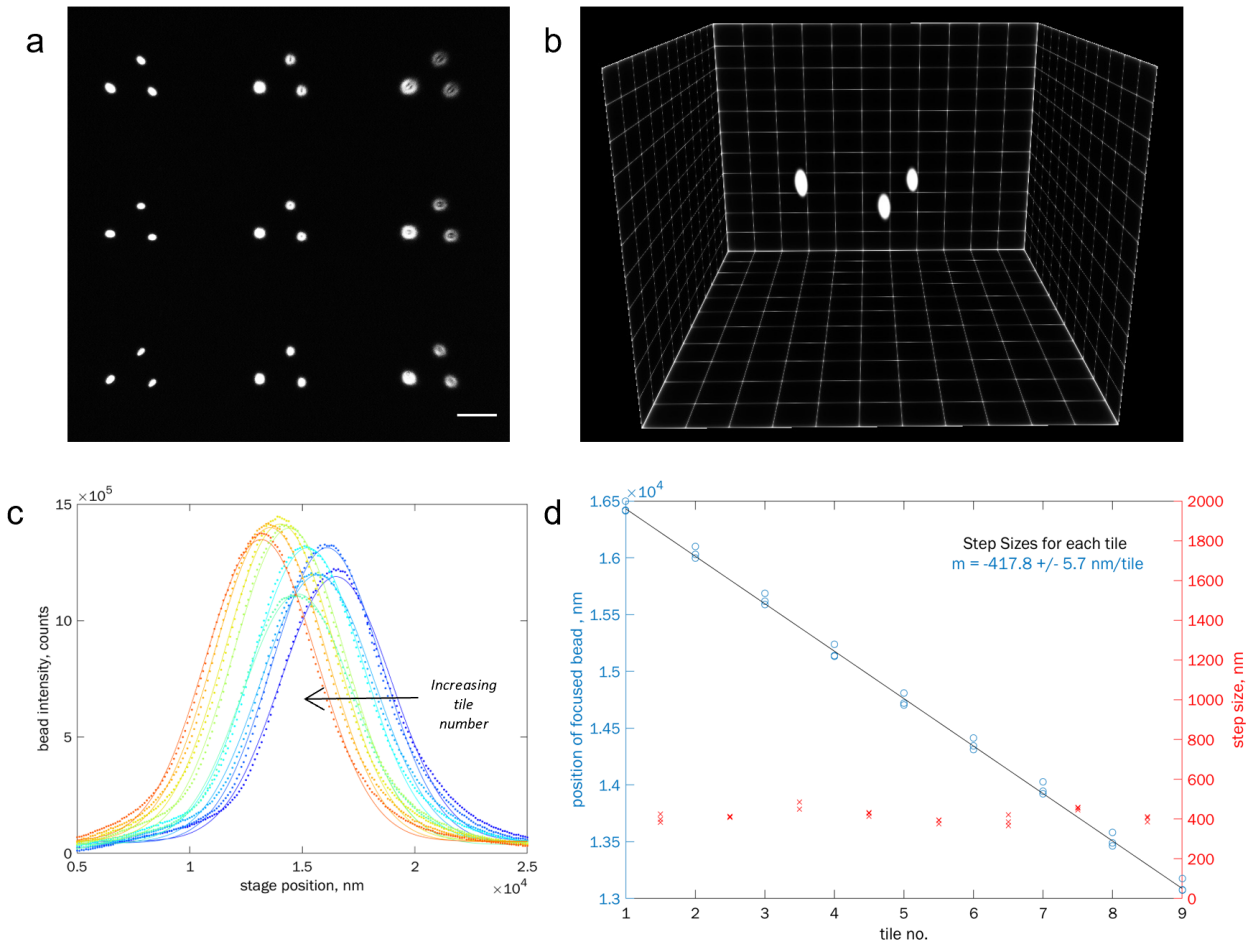

Figure 5.10: **MFM characterization of a 400 nm focal-shift DOE from a z-stack of immobilized 200 nm dia. red fluorescent beads.** (a) MFM images of three 100 nm red fluorescent beads immobilized to a coverslip. Beads are in-focus at the plane closest to the coverslip, i.e., the bottom left tile. Scale: 10 μm. (b) 3D reconstruction of beads after deconvolution. Grid: 3 μm/grid square. (c) Bead intensity as a function of stage position from the tile closest to the bottom coverslip and objective (1, blue) to the tile furthest from the coverslip (9, red). Gaussian fit (solid lines) for each intensity profile determines the z localization of the bead in each tile and therefore the position of the associated focal plane. (d) Analysis of Gaussian fitted intensity profiles from tile 1 to 9. The position of the focused bead is extracted from the mean (centroid) of the corresponding Gaussian fit (blue circles). The fitted slope (black line) is the average focal shift for each tile: 417.8 +/- 5.7 nm/tile (or per focal plane). The individual focal shifts (red crosses) are the difference of adjacent tile localizations. Note there are 3 values for each tile from the 3 beads in the image in (a).

shown in Figure 5.10a. This measurement is also used to shift-correct and construct the 3D MFM image of the three beads, in Figure 5.10b, which is explained in further detail below. Figure 5.10c shows the normalized fluorescence intensity distributions of a single bead that appears successively in focus in each of the nine tiles, which were fitted to Gaussian curves in z. The positions of best focus for each tile are shown as blue dots (for 3 beads/measurements) in Figure 5.10d, while the tile-to-tile focal shifts are shown as red crosses. The slope of the fitted line establishes the focal shift, Δz, to be 418 +/- 5.7 nm. This focal shift is slightly larger than what we designed for (i.e., 400 nm) because the equation used for the design is a first order approximation of the transverse phase description (function) of a lens [1]. The tile-to-tile focal shifts are very consistent. However, this consistency is strongly dependent on the alignment of the DOE in the 4f relay system shown in Figure 5.1.

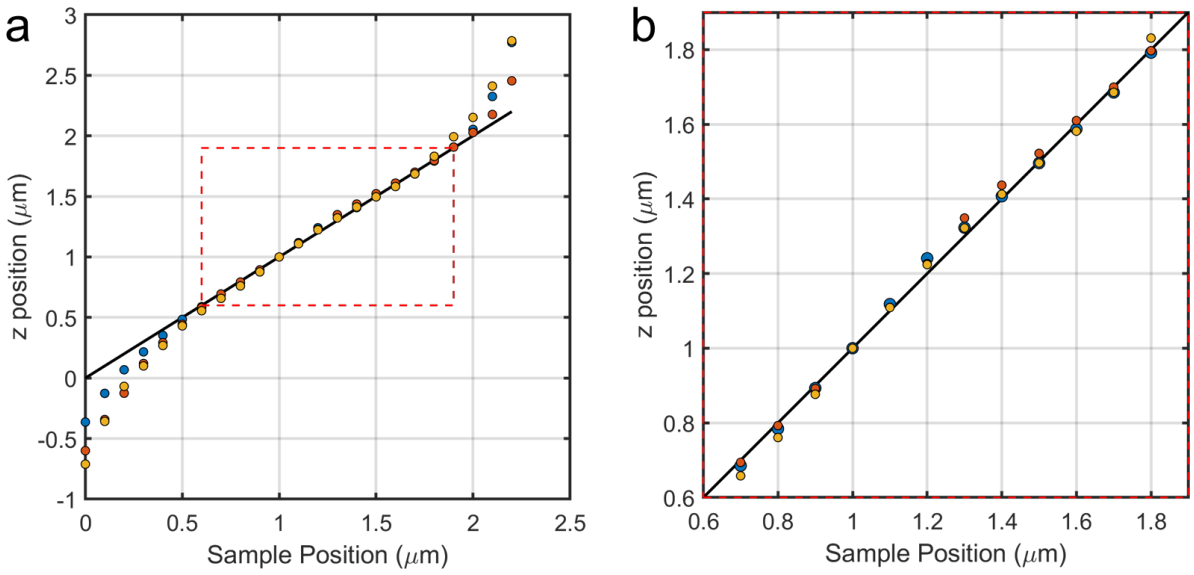

Figure 5.11: **Accuracy determination for particle localization in MFM imaging and reconstruction for a 418 nm focal shift DOE.** (a) The black line is the true position of the bead established with the piezo nano-positioner encoder. The colored points (blue, yellow, orange) are the measured positions after reconstruction and localization of the three beads. (b) The standard deviation is 13.1 +/- 0.2 nm in the 1.3 μm z range defined in the red box.

The alignment of the 9 tiles was performed as described above on the image data shown in Figure 5.10a and also in video 5. Three 200 nm dia. beads were immobilized to a coverslip and

were scanned in the axial direction (200 ms exposure time, 5 frames per second, 100 nm/step, 300 steps total). The video data of the 3 beads show a strikingly clear view of the axial interference associated with the axial Airy function and the delay that occurs as a result of the different focal planes in each tile (see center pixels of each bead image) [5]. We obtained the 3D deconvoluted images shown in Figure 5.10b using Imaris applying the MTD-SEC-I approach described above (see Section 5.A.2).

The localization measurements of the 3 beads shown in Figure 5.10 was also used to determine the accuracy of the localization. The results of the z-axial positions (measured) vs. the true positions (from the z-axis piezo encoder) for 3 beads are shown in Figure 5.11. Figure 5.11a shows the results over the full range allowed by the MFM optical (9 planes with a 418 nm focal shift between the planes) along with a line of slope = 1. As in Figure 5.3, there is a deviation from the line near the ends of the range that are a result of the increasingly poor determination of the bead locations due to the fact that the axial image of the bead is being increasingly truncated as it approaches the first and last MFM focal planes. Therefore, the central range (~1.3 μm) shown in Figure 5.11b is used to determine the accuracy. The accuracy is determined as the standard deviation of the differences between the measured and true values of the axial location. The results for the 3 beads are combined and give 13 nm for the accuracy over the 1.3 μm range.

5.A.5 Measurement and 3D analysis of beads diffusing in solution

As in the main text, we conducted measurements of 200nm dia. beads diffusing in 50% glycerol:water solutions. The expectation is for a uniform probability density function in the axial direction since the volume slab being sampled was 30um from the bottom coverslip surface. Figure 5.12a shows an MFM image of the beads in the 9 tiles and video 6 show the imaging data. Figures 5.12b,c are a portion of the reconstructed 3D images of the beads in solution using the MTD-SEC-I approach (2 different renderings; the egg shapes in Figure 5.12c are a schematic creation in Imaris and not a reconstruction of the actual beads).

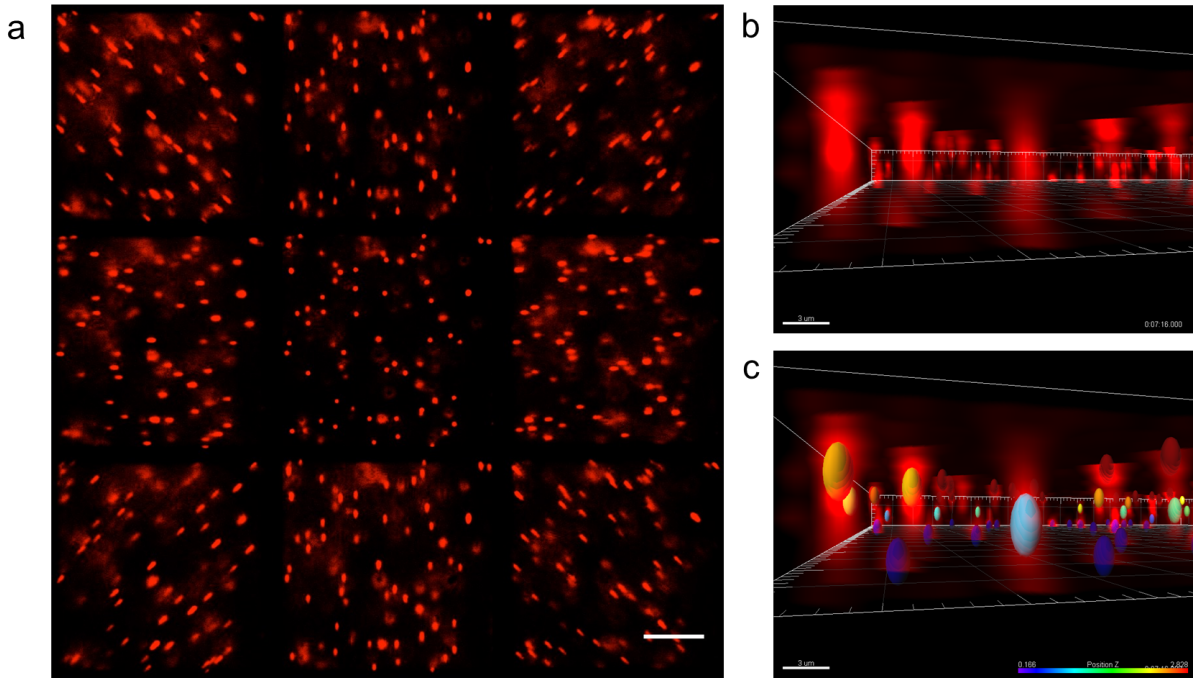

Figure 5.12: **Measurement and particle localization for 200 nm diffusing beads in 50% glycerol solution.** (a) Diffusing fluorescent beads measured at 20 Hz frame rate for 500 frames with 50 ms exposure time. Scale bar = 10 μm. (b) 3D reconstruction of beads using the MTD-SEC-I approach and final rendering and localization determination with Imaris. Each frame of the video data was preprocessed by deconvolution as described above in the SI. Scale bar = 3 μm. (c) 3D particle localization of reconstruction image. Ellipsoids are creations of the localization and the color coding shows the z position of each bead. White scale bars = 3 μm.

Figure 5.13a shows the distribution of log(counts) vs. z-position over the full range of the MFM optic. This is different than Figure 5.4b in the main text where the localizations near the limits of the axial range were omitted. The reason for that is clear from the U-shaped distribution in Figure 5.13b. The pile-up near the limits of the range results from the fact that the axial localization approach used here cannot have a centroid located beyond the 1st or 9th focal planes. This is clearly evident in video 7 of the 3D trajectories of the beads; the trajectories of the centroids do not extend beyond the upper and lower focal planes. The region between the 2 limits is rather flat and uniform as expected. Further corroboration of the fidelity of the reconstruction comes from an analysis of the dynamics. The transport of the beads is characterized by the 3D Ensemble Averaged Mean Square Displacement (EA-MSD) of their motion. The slope in the log(MSD) vs. log lag

time plot is α=0.993, which is the expected results for Brownian diffusion (α =1).

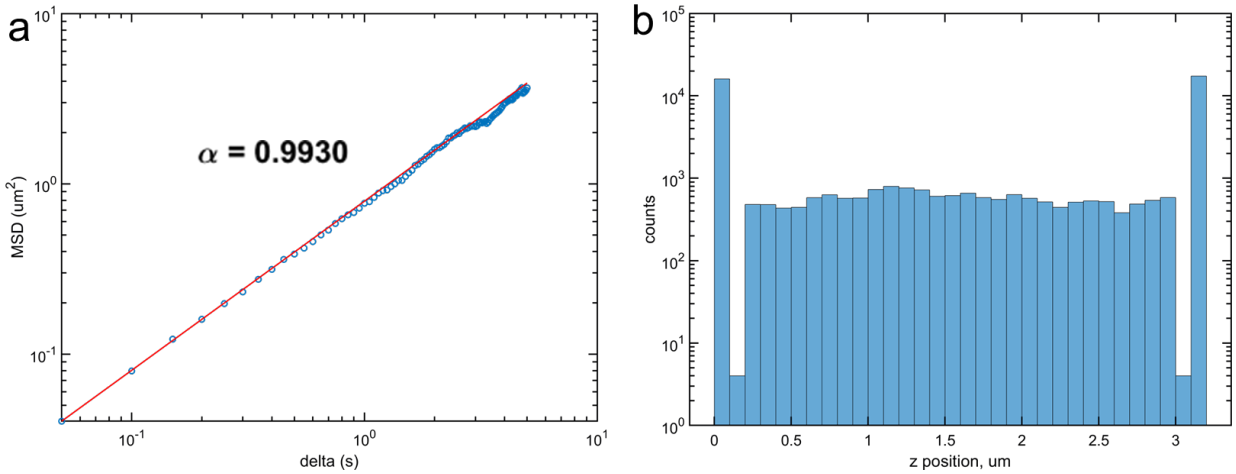

Figure 5.13: **Dynamics and localization analysis of diffusing beads.** (a) Ensemble-averaged MSD of diffusing beads from Figure 5.12. 19340 displacements averaged over 897 recorded trajectories. The slope of the log-linear fit (red line) $\alpha \approx 1$ is the diffusion scaling, which is signature of Brownian motion. (b) Histogram of the z position of each recorded localization. The distribution of the z localization is heavily biased to the extremes of the measurement range. These extremes were omitted from the MSD analysis as the axial motion is clearly distorted there.

Both Figure 5.4b and Figure 5.13b show some ripple structure (small deviations from a uniform distribution) that are greater than Poisson counting noise. The ripples also appear to be periodic. This might be associated with the precision of localization due to the Fisher information criterion, which gives more precision between the focal planes in MFM. We tested whether there is a non-uniform distribution of localizations by constructing a "meta-pixel" that can detect pixel locking error[6, 7]. The analysis approach is schematically represented in Figure 5.14a and results of this analysis are shown in Figure 5.14b-c. The same data are represented in 2 ways. Figure 5.14b shows the localizations from all the bead data along a range of z that is equal to the 418 nm focal shift (the data collapsed onto a single such range to construct the meta-pixel) and spread out horizontally to allow visualization by shifting each localization horizontally by a random value chosen from a uniform distribution. The distribution of points looks uniform by eye. Figure 5.13b represents the meta-pixel data along z quantitatively by counts in bins. Again, the distribution is nearly uniform with some random noise. If the ripples observed in Figure 5.4b and Figure 5.13b where related to

the Fisher information precision or some other periodic error, this would show up in the meta-pixel as a bias away from a uniform distribution [6, 7].

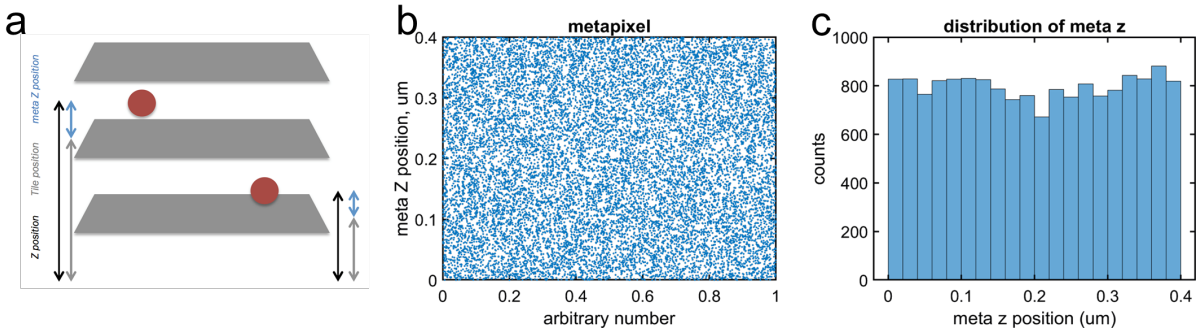

Figure 5.14: **Analysis to ascertain localization bias from a possible pixel locking effect.** (a) Schematic of 1D 'meta-pixel' calculation. The position in the meta-pixel (blue arrows) of the localized particle (red dots) is calculated as the difference between the actual z position (black arrows) and the nearest lower tile position (gray arrows). The gray tiles represent three focal planes measured by MFM. (b) 1D 'meta-pixel' construction from the z positions obtained from particle localization. The meta Z position, that is the position in the meta pixel, is mapped into 2D for visualization by assigning each meta z position a random number from a uniform distribution. We observe that meta-pixel mapping is random and uniform; visually there is no indication of 'pixel-locking'. (c) Histogram of meta Z positions. Distribution of the meta Z position is nearly uniform with a slight dip in probability near the center (~0.2nm) of the z axial meta-pixel.

Figure 5.15a shows a localization bias to the top and bottom of the analysis range as was noted in Figure 5.13. The cause for this was already discussed. The meta-pixel approach was repeated in segments to test localization bias in each analysis window. The meta-pixel analysis of 8 segments, i.e., each focal plane-to-focal plane interval, in Figure 5.15b shows a 'ripple' pattern of the z localization distribution. The dotted vertical lines are the locations of each MFM focal plane. The observed match between the small peaks in the distribution and the position of the focal plane suggests that the ripple structure occurs because there is a greater probability of localization at the focal planes.

This modulation of the axial localization probability is not consistent with the modulation of precision that is described by Fisher information theory. We believe the error arises from the image reconstruction approach, which we are investigating further. Nevertheless, the consistency of the results of 3D particle tracking by MFM with two DOEs designed with different focal lengths

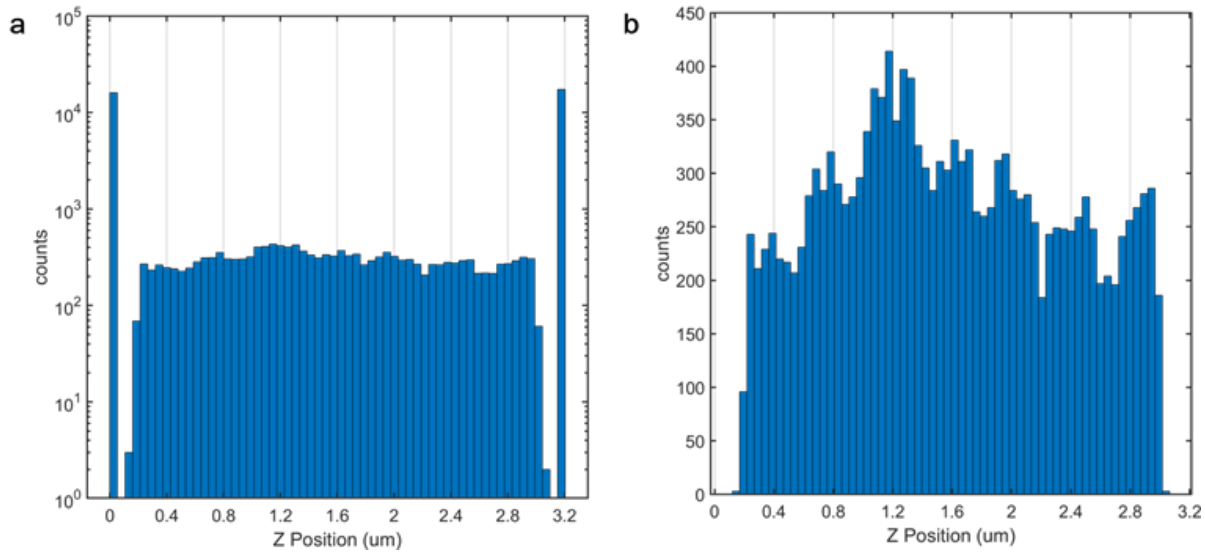

Figure 5.15: **Meta-pixel analysis indicating periodic localization bias.** (a) Log-linear plot of the full distribution of z information shown from Figure 5.13b with vertical lines denoting the location of the focal planes. (b) The same distribution omitting localizations that occur at the extremes of the axial range of the MFM. Vertical lines denote the locations of the MFM focal planes.

demonstrates that Nyquist sampling is not an issue the with particle tracking and localization approach that we have developed and report here.

REFERENCES

[1] Sara Abrahamsson, Jiji Chen, Bassam Hajj, Sjoerd Stallinga, Alexander Y Katsov, Jan Wisniewski, Gaku Mizuguchi, Pierre Soule, Florian Mueller, Claire Dugast Darzacq, et al. Fast multicolor 3d imaging using aberration-corrected multifocus microscopy. *Nature methods*, 10(1):60–63, 2013.

[2] Xiaolei Wang, Xiang Huang, Itay Gdor, Matthew Daddysman, Hannah Yi, Alan Selewa, Theresa Haunold, Mark Hereld, and Norbert F Scherer. Snapshot 3d tracking of insulin granules in live cells. In *Three-Dimensional and Multidimensional Microscopy: Image Acquisition and Processing XXV*, volume 10499, pages 33–39. SPIE, 2018.

[3] Toan Huynh, Matthew K Daddysman, Ying Bao, Alan Selewa, Andrey Kuznetsov, Louis H Philipson, and Norbert F Scherer. Correlative imaging across microscopy platforms using the fast and accurate relocation of microscopic experimental regions (farmer) method. *Review of Scientific Instruments*, 88(5):053702, 2017.

[4] Kuan He, Zihao Wang, Xiang Huang, Xiaolei Wang, Seunghwan Yoo, Pablo Ruiz, Itay Gdor, Alan Selewa, Nicola J Ferrier, Norbert Scherer, et al. Computational multifocal microscopy. *Biomedical Optics Express*, 9(12):6477–6496, 2018.

[5] James Pawley. *Handbook of biological confocal microscopy*, volume 236. Springer Science & Business Media, 2006.

[6] Yuval Yifat, Nishant Sule, Yihan Lin, and Norbert F Scherer. Analysis and correction of errors in nanoscale particle tracking using the single-pixel interior filling function (spiff) algorithm. *Scientific reports*, 7(1):1–10, 2017.

[7] Stanislav Burov, Patrick Figliozzi, Binhua Lin, Stuart A Rice, Norbert F Scherer, and Aaron R Dinner. Single-pixel interior filling function approach for detecting and correcting errors in particle tracking. *Proceedings of the National Academy of Sciences*, 114(2):221–226, 2017.

CHAPTER 6

FUTURE DIRECTIONS

6.1 Native pseudoislet growth and transport

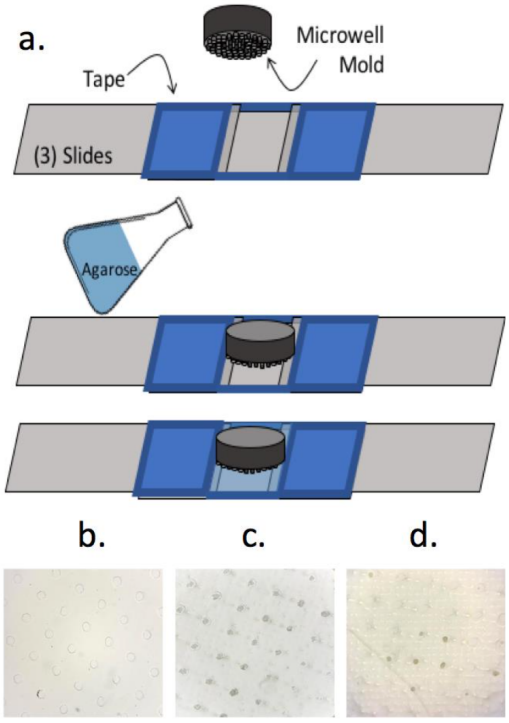

Figure 6.1: **Fabrication of microwells for controlled pseudoislet growth.** (a) Preparation of microwell chip from agarose using a 3D printed mold. (b) Clean microwell chip obtained from a (c) Microwell chip with cells added. (d) Result after 5-7 days, showing pseudoislets in wells.

In the pancreas, critical endocrine secreting cells are located in dense, highly vascularized clusters called islets of Langerhans. The islet of Langerhans are sphere-shaped clusters comprised of specialized cells that are critical for blood sugar regulation. One of the subunits is the insulin-containing β-cell. Surprisingly, the size of islets of Langerhans ($\sim$150 microns in diameter, $\sim$25 cells) is conserved across species[1]. Larger animals have an increased number of islets, not larger islets, in proportion to body mass [1, 2]. Islets larger than 200 microns are rare and exhibit impaired insulin secretion [3]. Size and geometry requirements are constrained by the optimal formation of

stable synchronization of β-cells through electrical gap-junction coupling [3]. In islets of up to ~200 microns, weak pair-wise correlations between β-cell calcium activity extend throughout the whole cell cluster [4]. These results suggest beta-cell clustering and islet size are critical for normal glucose regulation.

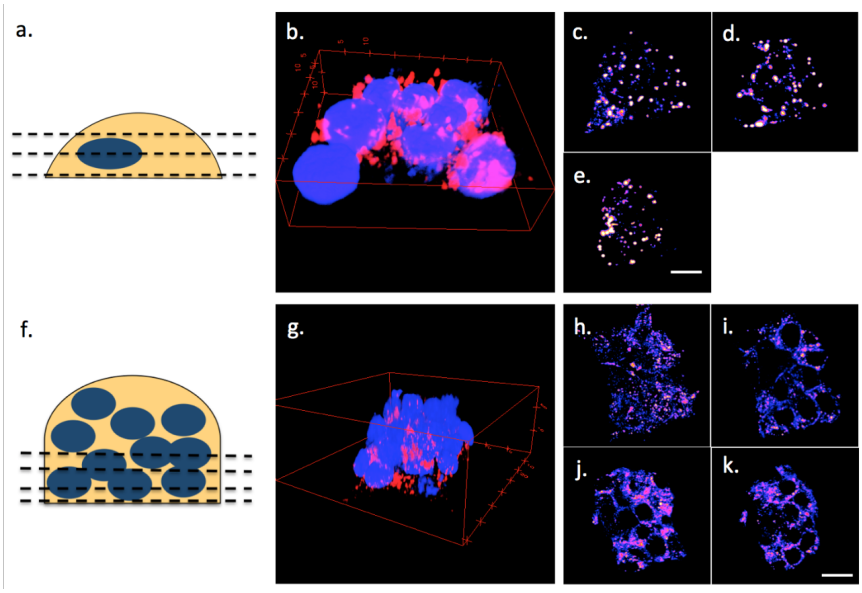

Figure 6.2: **Schematic and 3D rendering of a monolayer and pseudoislet.** (a) Schematic of a monolayer (b) 3D rendering of a monolayer with nuclei (blue) and insulin granules (red) (c-e) bottom, middle, and top images of insulin granules with mCherry recorded based on schematic a. (f) Schematic of pseudoislet (g) 3D rendering of a pseudoislet (h-k) the bottom to top images recorded based on schematic f. Scale 10 um

The transport results in the monolayer grown MIN6 β-cells presented thesis work is limited in physiological understanding and does not consider the importance of cooperative electrochemical signalling. MIN6 cells grown flat as monolayers in culture show much lower functional resemblance to β-cells *in vivo*, such as GSIS and gene expression [5]. This is largely considered to be a result of loss of cell-to-cell contacts [6]. 3D culture growth into "pseudoislets" restores MIN6 β-cell response to glucose, yet β-cell activity such as insulin secretion is highly dependent on cell number or cluster size [7].

We developed a method to control the growth of 3D growth β-cells for reproducible pseudoislet sizes (Fig 6.1). A microwell array is made from agarose from a 3D printed microwell mold (Fig

6.1a. After adding a suspension of cells into the microwell array, pseudoislets can be formed with uniform cluster size in less than a week (Fig 6.1b-d).

We are interested in extending the analysis in this thesis work to cells growth in 3D clusters to achieve gap junction geometries that are closer to native islets of Langerhans. Transport of insulin granules grown in monolayers (Fig 6.2a-e) is compared to granule transport in pseudoislet configurations (Fig 6.2f-k). In both cases, the axial dependence of transport is studied by monitoring transport at two focal planes. Near the coverslip is termed the bottom imaging plane and selectively measures the actin rich region, while the middle imaging plane is ~5 μm above the bottom plane and primarily probes the microtubule only cross-section. Further analysis could extend the axial sampling in pseudoislet grown cell clusters to probe deeper insulin granule transport and whether there are new transport mechanisms present in deeper cell locations.

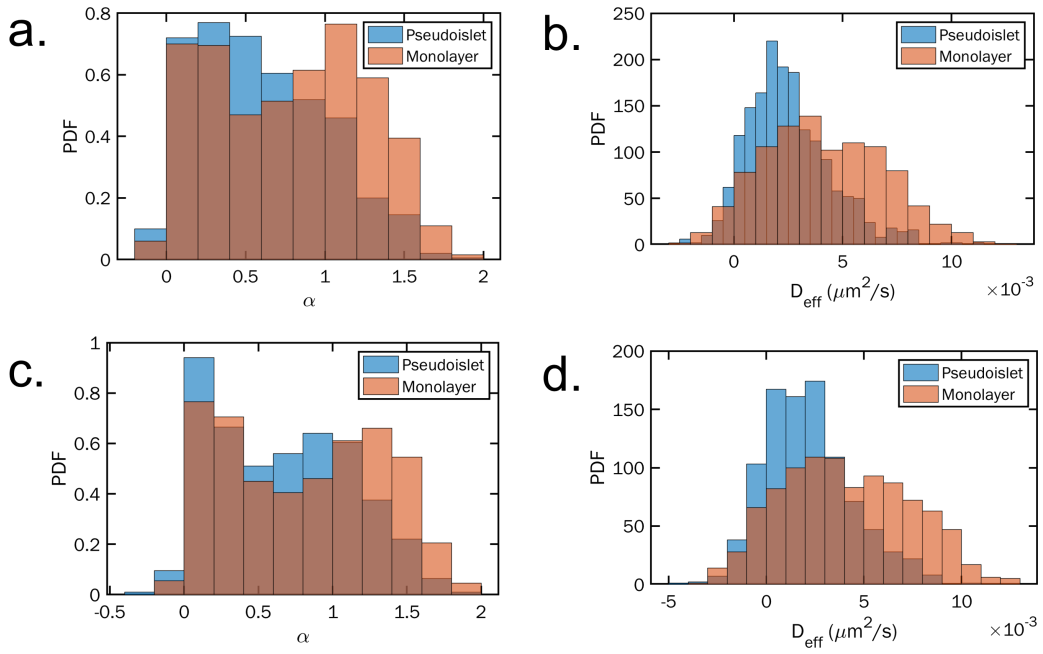

Figure 6.3: **Distribution of transport parameters α and D_{eff} for insulin granules of β-cells grown in monolayers and pseudoislets.** (a) α distribution of insulin granule transport at the middle imaging plane of cells grown as monolayers (orange) and pseudoislets (blue), ~5 μm above the coverslip. (b) D_{eff} of the trajectories shown in a. (c) α distribution of insulin granule transport at the bottom imaging plane of cells grown as monolayers (orange) and pseudoislets (blue), ~1 μm above the coverslip. (d)D_{eff} of the trajectories shown in c.

Preliminary measurements in insulin granule transport show slower and more confined overall behavior. Interestingly, the diffusive nature of insulin transport by way of α is comparable for both monolayer and pseudoislet grown cells.

6.2 Three dimensional tracking and analysis

We imaged the 3D motion of insulin granules in MIN6 cells within a 5 μm depth of the cell for 100s at 10 frames per second. Since MFM obtains 3D and 2D information simultaneously, trajectories of single insulin granules in 2D are also obtained for each of the 9 different focal planes. 3D trajectories were obtained for each insulin granule with MFM image reconstruction as described above. Imaris (Oxford Instruments) was used for single particle tracking (see SI for details). Figure 6.4a shows 341 trajectories of insulin granules in a single MIN6 cell whose duration are longer than 10s (100 frames). The distribution of axial (z-axis) positions of these insulin granules accumulate over the total measurement time (100s, 1000 frames) is shown as Fig 6.4b. The distribution is remarkable, revealing that most of the insulin granules are located and moving close to the bottom of cell or in other layers as opposed to a uniform or slowly varying with axial position. We verified that this axial position probability distribution is not a result of a systematic imaging error associated with MFM imaging or particle tracking by using fluorescence beads diffusing deep in solution or near a coverslip. The resultant axial position probability distribution (with >100,000 samples) 50 μm deep in solution is nearly uniform with a periodic modulation that is due to the modulation of the axial measurement precision that can be derived from Fisher information theory. The axial distribution near the coverslip surface shows a gradual variation with the same superimposed mild modulation. Both distributions are completely different than that obtained for granules in live cells (Fig 6.4b).

The ensemble MSD serves as a basic analysis of motion and provides a starting point to evaluate transport representative of the whole cell and for 2D and 3D motion. However, since the transport may be non-ergordic on our measurement timescale, only trajectories with qualitatively

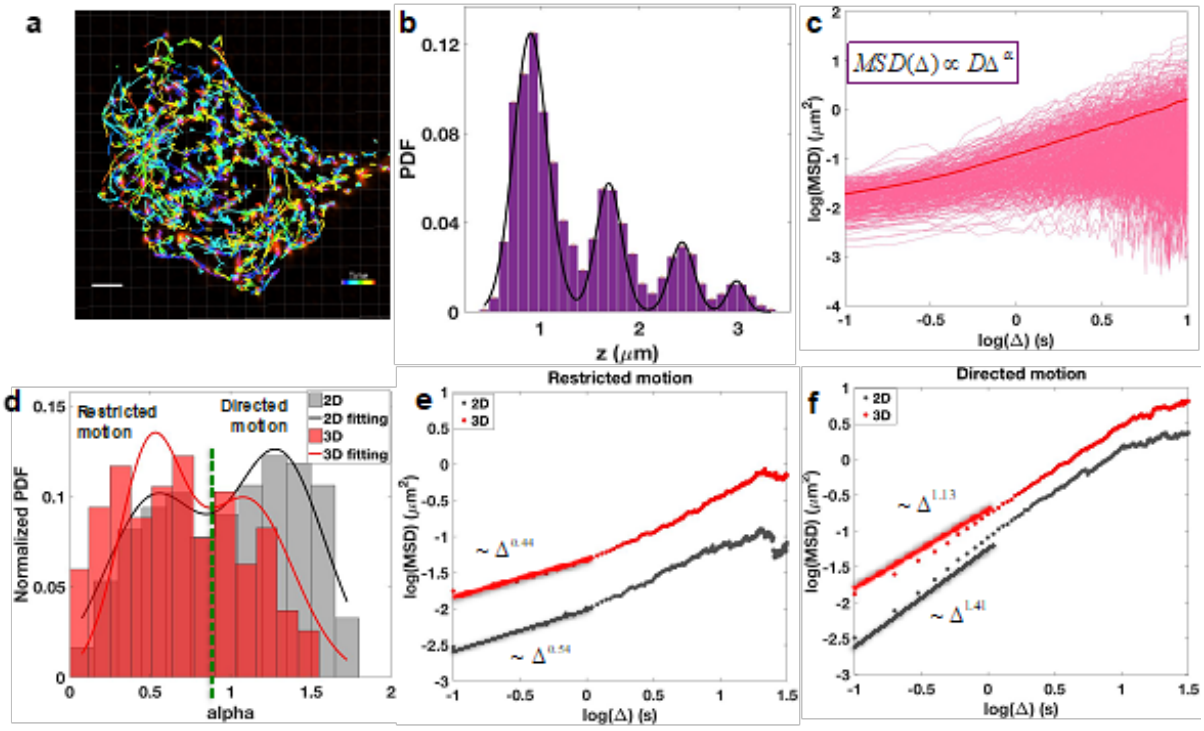

Figure 6.4: **3D dynamics of single insulin granules in live MIN 6 cell with MFM.** (a) 3D color-coded trajectories (341 total) of insulin granules in the MIN6 cell shown in Fig. 1c. Scale bar is 3μm. The color bar denotes time, in seconds; the total time is 100s. (b) The z position distribution of these 341 insulin granules for the 100s total measurement time (with >78,000 samples and bin size of 0.1μm). The black curve is a fit to Gaussian functions. The distances between peaks are 0.77μm, 0.76μm and 0.55μm respectively from first to the forth peaks. (c) The 3D mean square displacement (MSD) of insulin granules in the MIN6 cell shown in Fig. 1c. The pink curves are the MSDs for each individual insulin granule, and the red curve is the ensemble MSD from insulin granules in the cell. (d) PDF of the transport exponent α for 3D trajectories (red histogram) and 2D trajectories (grey histogram). The latter is obtained from the center tile of the MFM image (the fifth tile). The green dashed line denotes a separation of the bimodal distribution of α at α =0.8. (e) 2D (black) and 3D (red) MSD for restricted motion. The linear fitting of ensemble MSD α = 0.54 for 2D, and α=0.44 for 3D motion. (f) 2D (black) and 3D (red) MSD for directed motion. The linear fitting of the initial portion of the ensemble MSDs yields α=1.41 for 2D, and α=1.13 for 3D motion.

and quantitatively comparable MSDs should be combined in the ensemble. Figure 6.4c shows the individual (pink curves) and ensemble (red curve) MSDs of all single insulin granules from 3D trajectories longer than 100 frames (10s) as a function of log lag time. The slope of each curve yields α, and the intercept gives the diffusion coefficient of that granule. The MSD's of the individual granules exhibit two types of behaviors; some are straight, while others curve upwards. The

ensemble MSD only curves upward, and is, therefore, not a good measure of the heterogeneous dynamics. Moreover, the PDF of the transport exponent α calculated for each trajectory in 2D (from the center tile) and 3D is bimodal, as shown in Fig. 6.4d, which demonstrates two kinds of motion for single insulin granules in 2D and 3D. Bimodal Gaussian fitting suggests separating the granule populations into two groups at about $\alpha = 0.8$. Trajectories with α less than 0.8 exhibit restricted motion, while those greater than 0.8 are termed directed motion. Directed motion trajectories exhibit much greater displacement than those with restricted motion. The distributions of z positions of insulin granules for the two types of motion are very similar; both are highly modulated and most insulin granules are located near the bottom of the cell.

Table 6.1: **Transport exponents for restricted and directed motion for 2D dynamics in different planes (3rd, 5th and 8th tiles) and 3D dynamics**

	3rd tile	5th tile	8th tile	3D
α_r	0.49	0.54	0.60	0.44
α_d	1.30	1.41	1.31	1.13

As shown in Fig. 6.4e-f, we calculated the ensemble 2D and 3D MSDs for the restricted and directed types of motion. We find that the ensemble MSDs for 2D motion have larger values of α than motion in 3D for both restricted and directed motion. The difference is more pronounced for directed than restricted motion. The 2D data in Fig. 6.4 are obtained from the center tile. We also calculated the ensemble 2D MSD from the third, the eighth tile with the results in Table 6.1. All the ensemble 2D MSDs from the different 2D focal planes have larger α than that obtained from 3D trajectories.

6.3 Alternate Insulin therapies

Diabetes mellitus, commonly known as diabetes, is actually a family of diseases that affect your body's ability to produce and/or properly regulate blood sugar. Type 2 Diabetes (T2D) accounts for >90% of cases. In the United States alone, there are an estimated 30 million people affected

(nearly 10% of the U.S. population) [8], and this statistic is increasing rapidly. Unmanaged T2D cascades into an assortment of secondary afflictions; including high blood pressure, heart diseases, muscle necrosis, and obesity. There are even strong correlations with mental health issues and psychological well-being.

T2D is the most prevalent disease affecting the U.S. socially and economically, yet cures remain elusive and advances in treatment plans is stagnant. Therapeutic plans focus on increasing insulin delivered into the bloodstream by injections. This therapy is life critical for many affected individuals. Meanwhile, the average cost of human insulin is skyrocketing - rising 54% in the past 5 years and more than 1000% in the past 10 years[9]. Clearly, the cost of insulin is becoming prohibitively expensive, which exacerbates the public health crisis.

Insulin is naturally produced protein that is stored and then secreted from specialized β-cells in the pancreas. Simulated insulin secretion is part of a concerted mechanism that involves several regulatory proteins that rely on electrical and chemical signaling. A key electrochemical signaling agent in cells is calcium, Ca^{2+}. Increases in intracellular calcium concentration in beta-cells is necessary for natural insulin secretion [10]. While drug-based stimulation is known, we wish to explore new directions. In particular, new technologies in bioelectrical stimulation are being applied to other electrically active cells, - e.g., heart and brain - to control Ca^{2+} levels [11]. However, it is not known whether bioelectrical stimulation can be applied to beta-cells to increase insulin production. Success of the research proposed here will open the possibility of a new type of insulin therapy that uses naturally produced insulin that is intrinsic to the patient, thereby removing the costs associated with extrinsic manufactured and administered therapies.

We propose a new approach to insulin therapy that circumvents the pharmaceutical industry to manufacture insulin. Defects that lead to T2D (mainly) stem from ineffective insulin secretion not the amount of insulin produced in beta-cells [12]. Beta-cells naturally store large insulin reserves; less than 10% of stored insulin is released for a given meal in a healthy person. So, insulin is still produced in patients with T2D, but their beta-cells are not able to properly release it into the

bloodstream. We propose that bioelectrical stimulation could allow diabetic patients to use their own insulin rather than rely on injections.

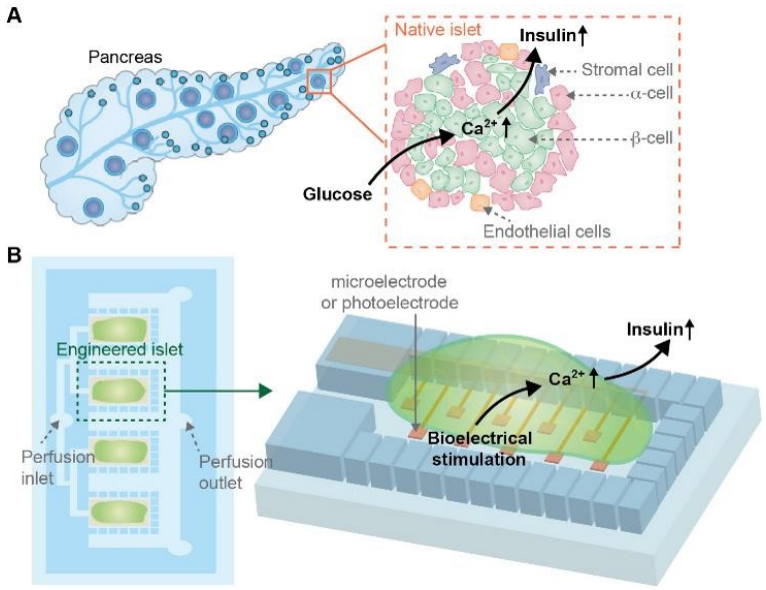

Figure 6.5: **Organ-inspired bioelectrical stimulation of insulin secretion.** Insulin secretion follows Ca2+ elevation triggered by glucose in pancreas (A) or bioelectrical stimulation in a device chip (B).

Figure 6.5 shows the native, organ-inspired principle for two readily available methods to elevate Ca2+ levels by bioelectrical stimulation: microelectrode stimulation and photoelectrochemical stimulation. Microelectrode stimulation uses wired electrodes to apply a voltage to the cells, similar to how transistors in our electronic devices work. By contrast, photoelectrochemical stimulation facilitates cellular electrical activity through light activation of nanoscale semiconductor materials (e.g., like with solar cells). These techniques - proven to work for heart and brain cells in the Tian Lab - will be used to test the principle of controllable insulin release in pancreatic cells.

REFERENCES

[1] Marko Gosak, Andraž Stožer, Rene Markovič, Jurij Dolenšek, Marko Marhl, Marjan Slak Rupnik, and Matjaž Perc. The relationship between node degree and dissipation rate in networks of diffusively coupled oscillators and its significance for pancreatic beta cells. *Chaos: An Interdisciplinary Journal of Nonlinear Science*, 25(7):073115, 2015.

[2] Kinsei Kou, Yoshifumi Saisho, Seiji Sato, Taketo Yamada, and Hiroshi Itoh. Islet number rather than islet size is a major determinant of β-and α-cell mass in humans. *The Journal of Clinical Endocrinology & Metabolism*, 99(5):1733–1740, 2014.

[3] Junghyo Jo, Moo Young Choi, and Duk-Su Koh. Size distribution of mouse langerhans islets. *Biophysical journal*, 93(8):2655–2666, 2007.

[4] Dean Korošak and Marjan Slak Rupnik. Collective sensing of β-cells generates the metabolic code. *Frontiers in physiology*, 9:31, 2018.

[5] Martha (Mattie) Renn. Investigating the cellular manifestations of diabetes: biophysical and transcript-level of min6 sublines. unpublished thesis, 2016.

[6] A Chowdhury, Oleg Dyachok, Anders Tengholm, Stellan Sandler, and Peter Bergsten. Functional differences between aggregated and dispersed insulin-producing cells. *Diabetologia*, 56(7):1557–1568, 2013.

[7] N Kojima, S Takeuchi, and Y Sakai. Engineering of pseudoislets: effect on insulin secretion activity by cell number, cell population, and microchannel networks. In *Transplantation proceedings*, volume 46, pages 1161–1165. Elsevier, 2014.

[8] American Diabetes Association. Economic costs of diabetes in the us in 2017. *Diabetes care*, 41(5):917–928, 2018.

[9] S Vincent Rajkumar. The high cost of insulin in the united states: an urgent call to action. In *Mayo Clinic Proceedings*, volume 95, pages 22–28. Elsevier, 2020.

[10] Patrik Rorsman and Erik Renström. Insulin granule dynamics in pancreatic beta cells. *Diabetologia*, 46(8):1029–1045, 2003.

[11] Eleanor Ostroff, Kavita Parekh, Aleksander Prominski, and Bozhi Tian. Biocompatible and nanoenabled technologies for biological modulation. *Advanced Materials Technologies*, 7(2):2100216, 2022.

[12] June Chunqiu Hou, Le Min, and Jeffrey E Pessin. Insulin granule biogenesis, trafficking and exocytosis. *Vitamins & Hormones*, 80:473–506, 2009.

APPENDIX A

RELATED CODE AND ANALYSIS SCRIPTS

A.1 Single Particle Tracking and Scrum Size Exclusion

A.1.1 Trajectory curation and relinking granule and scrum localization sets

```
%Tracking using new method adapted from Matt Daddysman. Find all srum positions first,
% and then filter the trajectories to remove false positives. After, use these new scrum
%positions to exclude out of the 'all' positions data set.

% Functions:
%   SPIFF_sort.m
%   track.m
%   filtertraj.m
%   export_fig.m

% Important outputs:
% ids made while making MSD matrix that correlates traj and msd
% trackedlarge/small are the trajectories BEFORE applying a min length
% largetraj/smalltraj is the traj information separated as gran and scrum
% traj is the x/y/t/scrumID/ID information
% T and Tfull tables has inforamtion like alpha and Diff coeff.
% msd is the MSD for each individual trajectory

%==============================
% Give Initial Information about EXPT
%==============================
clearvars;
exptno = 'HY1071';
plane = 'top';
```

```
25
26 %==============================
27 % Import the CSVs from Mosic
28 %==============================
29
30 d = csvread(['Tracking Input/' exptno '_' plane  '_s_Results.csv']);
31 d = d(:,3:12);
32 d(:,1) = d(:,1)+1;
33 alldata = d;
34
35 d = csvread(['Tracking Input/' exptno '_' plane  '_l_Results.csv']);
36 d = d(:,3:12);
37 d(:,1) = d(:,1)+1;
38 largedata = d;
39
40 %==============================
41 % SPIFF correct the particle positions
42 %==============================
43
44 data_l = largedata(:,2:3);
45 data_a = alldata(:,2:3);
46
47 mp_totx = data_l(:,1)-floor(data_l(:,1));
48 mp_toty = data_l(:,2)-floor(data_l(:,2));
49 SPIFF_l = fun_SPIFF_sort(data_l,mp_totx,mp_toty);
50 largedata(:,2:3) = SPIFF_l;
51
52 mp_totx = data_a(:,1)-floor(data_a(:,1));
53 mp_toty = data_a(:,2)-floor(data_a(:,2));
54 SPIFF_a = fun_SPIFF_sort(data_a,mp_totx,mp_toty);
55 alldata(:,2:3) = SPIFF_a;
```

```
56
57 %==============================
58 % Link Scrum Trajectories Together & Plot
59 %==============================
60
61 linkrange = 40;
62
63 largepos = sortrows(largedata(:,[2:3 1]),3);
64 trackedlarge = fun_track(largepos,linkrange);
65
66 for n = 1
67 figure,
68 subplot(1,3,1)
69 fun_filtertraj(trackedlarge,1,1,0,0);
70 xlim([0 512])
71 ylim([0 512])
72 ax = gca;
73 ax.Box = 'on';
74 ax.XTickLabel = [];
75 ax.YTickLabel = [];
76 ax.LineWidth = 1.5;
77
78 subplot(1,3,2)
79 fun_filtertraj(trackedlarge,500,1,0,0);
80 xlim([0 512])
81 ylim([0 512])
82 ax = gca;
83 ax.Box = 'on';
84 ax.XTickLabel = [];
85 ax.YTickLabel = [];
86 ax.LineWidth = 1.5;
```

```
87
88  subplot(1,3,3)
89  fun_filtertraj(trackedlarge,800,1,0,0);
90  xlim([0 512])
91  ylim([0 512])
92  ax = gca;
93  ax.Box = 'on';
94  ax.XTickLabel = [];
95  ax.YTickLabel = [];
96  ax.LineWidth = 1.5;
97  end % plots
98
99  %%
100
101 %================================
102 % Double Check the chosen filter for traj
103 %================================
104
105 % (1) xpos (2) ypos (3) timeframe (4) trajID
106
107 largetraj_patch = fun_filtertraj(trackedlarge,500,1,1,1);
108 trackedlarge = largetraj_patch;
109 trackedlarge(any(isnan(trackedlarge), 2), :) = [];
110
111 %================================
112 % Separate Granule and Scrum Positions
113 %================================
114
115 %From the uploaded position information, filter the small and large radius
116 %data sets so that 'small' particles are excluded from the big one
117
```

```
118 radius = 8;
119
120 nframes = max(alldata(:,1));
121
122 wh = waitbar(0,['Processing frame 0 of ' num2str(nframes)]);
123
124 for m=1:nframes %for each frame
125     waitbar(m/nframes,wh,['Processing frame ' num2str(m) ' of ' num2str(nframes)]);
126     bigcenters = largetraj_patch(m == largetraj_patch(:,3),1:2); %pull out the centers
    ↪  of the 'scrum' positions in each frame
127     smallidx = find(alldata(:,1) == m);
128     falsepts = alldata(smallidx,2:3);
129     exclude = false(length(smallidx),1); %keep track if the point is inside one of the
    ↪  circles
130     for n=1:size(bigcenters,1) %now go through all of the big centers in the frame
131         dist = sqrt((falsepts(:,1) - bigcenters(n,1)).^2   +   (falsepts(:,2) -
    ↪  bigcenters(n,2)).^2);
132         insr = dist<radius;
133         exclude = exclude | insr;
134     end
135
136     alldata(smallidx,4) = exclude;
137
138 end
139
140 smalldata = alldata(alldata(:,4) == 0,:);
141
142 close(wh);
143
144
145 %%
```

```
146
147 %==============================
148 % Link small trajectories together
149 %==============================
150
151 linkrange = 8;
152
153 smallpos = sortrows(smalldata(:,[2:3 1]),3);
154 trackedsmall = fun_track(smallpos,linkrange);
155
156 for n = 1
157 % figure(2),
158 % subplot(1,3,1)
159 % filtertraj(trackedsmall,1,1,0,0);
160 % xlim([0 512])
161 % ylim([0 512])
162 %
163 % subplot(1,3,2)
164 % filtertraj(trackedsmall,500,1,0,0);
165 % xlim([0 512])
166 % ylim([0 512])
167 %
168 % figure(2),
169 % subplot(1,3,3)
170 % filtertraj(trackedsmall,700,1,0,0);
171 % xlim([0 512])
172 % ylim([0 512])
173 end %commented plots to check linkrange param
174
175
176 %%
```

```
177
178 %==============================
179 % Double Check the chosen filter for traj
180 %==============================
181 % (1) xpos (2) ypos (3) timeframe (4) trajID
182 figure,
183 smalltraj_patch = fun_filtertraj(trackedsmall,50,1,0,0);
184 trackedsmall = smalltraj_patch;
185 trackedsmall(any(isnan(trackedsmall), 2), :) = [];
186
187 save(['Working/' exptno '_' plane
    ↪  '_trajectories.mat'],'smalltraj_patch','largetraj_patch','trackedsmall','trackedlarge','exptno','pl
188
189 % Tracking is done!! yay! now organize the data into matrixes and make an ID
190 % matrix
191 %%
192 %==============================
193 % Make Matrix for tracked Data & Fix Traj ID
194 %==============================
195
196 %clearvars -except exptno plane;
197 load(['Working/' exptno '_' plane '_trajectories.mat']);
198
199 %expand the matrix and to add more information as needed
200 trackedsmall(:,5:9) = zeros([size(trackedsmall,1) 5]);
201 trackedlarge(:,5:9) = zeros([size(trackedlarge,1) 5]);
202
203 %Set column 5 to the Gran(1)/Scrum(2) ID
204 trackedsmall(:,5) = ones([size(trackedsmall,1) 1]);
205 trackedlarge(:,5) = 2.*ones([size(trackedlarge,1) 1]);
206
```

```
%order traj matrix based on ID numbers
trackedsmall = sortrows(trackedsmall,4);
trackedlarge = sortrows(trackedlarge,4);

%Redo the Traj IDs (col4) for trackedlarge so IDs don't duplicate with
%trackedsmall
IDsmall = unique(trackedsmall(:,4));

for n = 1:length(IDsmall)
    idx = trackedsmall(:,4)==IDsmall(n);
    sum(idx)
    trackedsmall(idx,4) = n;
end
clear IDsmall

IDlarge = unique(trackedlarge(:,4));
IDsmall = max(trackedsmall(:,4));

for n = 1:length(IDlarge)
    idx = trackedlarge(:,4)==IDlarge(n);
    sum(idx)
    trackedlarge(idx,4) = n+IDsmall;
end

% oldID = unique(trackedsmall(:,4));
% ID = zeros(length(trackedsmall),1);
%
%
% for n = 1:length(oldID)
%     if n == 1
%     A = n.*(ones( sum(trackedsmall(:,4)==oldID(n)), 1));
```

```
%    ID = A;
%     else
%     A = n.*(ones( sum(trackedsmall(:,4)==oldID(n)), 1));
%     ID = [ID;A];
%     end
% end
%
% trackedsmall(:,4) = ID;

%%%%%%%%%%%%%%%%%%%%%%%%%%%%%%%%%%%%%%%%
%combine the trajectory information
traj= [trackedsmall; trackedlarge];
% (1) xpos (2) ypos (3) timeframe (4) trajID (5) Gran/Scrum
%%%%%%%%%%%%%%%%%%%%%%%%%%%%%%%%%%%%%%%%

save(['Working/' exptno '_' plane '_trajectories.mat'],'traj','-append'); %phew!

clearvars -except traj smalltraj largetraj plane exptno
```

SPIFF_sort.m

```
function corrected_p = SPIFF_sort(p_in,SPIFF_x,SPIFF_y)

%%%%%%%%%%%%SPIFF correction %%%%%%%%%%%%%%%%%%
%%%Step 1 - check SPIFF data

%%%% R = 2   %%%%%
inds = find(p_in(:,1)>0);

```

```
9
10  %Now calculate the positive and negative probability density distributions
11  %(P(x_e) in the manuscript - eq. (7));
12  SPIFF_x_plus = SPIFF_x(SPIFF_x>=0.5);
13  SPIFF_y_plus = SPIFF_y(SPIFF_y>=0.5);
14  SPIFF_x_minus = SPIFF_x(SPIFF_x<0.5);
15  SPIFF_y_minus = SPIFF_y(SPIFF_y<0.5);
16
17  p_x_plus = sort(SPIFF_x_plus);
18  p_x_minus = sort(SPIFF_x_minus);
19  p_y_plus = sort(SPIFF_y_plus);
20  p_y_minus = sort(SPIFF_y_minus);
21
22  %The SPIFF corrected positions go here:
23  corrected_p = zeros(size(p_in));
24
25  %Seperates the positive and negative parts of the SPIFF in both x and y.
26  % for each one of the biased points, calculates the amount of points
27  % below its value.
28
29
30  for ww = 1:length(p_in)
31      %Treat position list for particle 1
32      if p_in(ww,1) == 0
33          continue
34      end
35      x1_curr = p_in(ww,1);
36      y1_curr = p_in(ww,2);
37      SPIFF_x_curr = x1_curr - floor(x1_curr);
38      SPIFF_y_curr = y1_curr - floor(y1_curr);
39      if SPIFF_x_curr>=0.5
```

```
        %a. Get percentile value:
        tmp_x = sum(p_x_plus<=SPIFF_x_curr)/length(p_x_plus);
        %b. Bring back to unmodolu'ed position:
        new_SPIFF_x = tmp_x/2; %if the position is positive (above the floor) it stays.
        corrected_p(ww,1) = ceil(x1_curr) + new_SPIFF_x;
    else
         %a. Get percentile value (how many particles are closer to center):
        tmp_x = sum((p_x_minus)>=(SPIFF_x_curr))/length(p_x_minus);
        %b. Bring back to unmodolu'ed position:
        new_SPIFF_x = tmp_x/2;   %If the position is negative (below the floor) it is
↪   moved by 1.
        corrected_p(ww,1) = ceil(x1_curr) - new_SPIFF_x;
    end
    if SPIFF_y_curr>=0.5
        %a. Get percentile value:
        tmp_y = sum(p_y_plus<=SPIFF_y_curr)/length(p_y_plus);
        %b. Bring back to unmodolu'ed position:
        new_SPIFF_y = tmp_y/2; %if the position is positive (above the floor) it stays.
        corrected_p(ww,2) = ceil(y1_curr) + new_SPIFF_y;
    else
         %a. Get percentile value (how many particles are closer to center):
        tmp_y = sum((p_y_minus)>=(SPIFF_y_curr))/length(p_y_minus);
        %b. Bring back to unmodolu'ed position:
        new_SPIFF_y = tmp_y/2;   %If the position is negative (below the floor) it is
↪   moved by 1.
        corrected_p(ww,2) = ceil(y1_curr) - new_SPIFF_y;
    end
end
```

```
%%%%%%%%%%%%%%%%%%%%%%%%%%%%%%%%%%%%%%%%%%%%%%%%%%%%%%%%%%%%%%%%%%%%%%%%%%%%%%%%
```

filtertraj.m

```
function xycoord = filtertraj(trajinfo,cutoff,plotdiffcolors, plottimetraj,plotposition)

%assuming that trajinfo is col1(xpos) col2(ypos) col3(time in frame)
%col4(id)



for m = 1:max(trajinfo(:,4)); %go though every trajectory
  a = find(trajinfo(:,4)==m); %pickout the trajjectory
  if length(a)>= cutoff %check that its larger than cutoff
      smallid(m) = true; %store information in a logical
  else
      smallid(m) = false;
  end
end

lastrow = [NaN NaN NaN NaN];%last row needs to be NaN for patch()  to create line
 ↪  instead of polygon
xycoord = [NaN NaN NaN NaN];%initialize xycoord matrix
for n = 1:max(trajinfo(:,4))
if smallid(n)==1
id = find(trajinfo(:,4)==n);
xysegment = vertcat(trajinfo(min(id):max(id),1:4),lastrow);
xycoord = vertcat(xycoord,xysegment);
cellxycoord{n}=vertcat(trajinfo(min(id):max(id),1:4),lastrow);
end
```

```
end




if plotdiffcolors == 1,
    hold on
for n = 1:max(trajinfo(:,4))
    if smallid(n) ==1
    plot(cellxycoord{1,n}(:,1),cellxycoord{1,n}(:,2),...
        'LineWidth',3);
    end
end
hold off
set(gca, 'color','none')
end

if plottimetraj == 1,
colormap(jet);
colorbar;
hold on
for n = 1:max(trajinfo(:,4))
    if smallid(n) ==1
    patch(cellxycoord{1,n}(:,1),cellxycoord{1,n}(:,2),cellxycoord{1,n}(:,3),...
        'EdgeColor','interp',...
        'Marker','o',...
        'MarkerSize',3,...
        'MarkerFaceColor','flat',...
        'LineWidth',1);
    end
end
```

```
hold off
set(gca,'color','none')

if plotposition == 1,
colormap(gray);
colorbar;
hold on
for n = 1:max(trajinfo(:,4))
    a = find(trajinfo(:,4)==n); %pickout the trajjectory
    x = trajinfo(min(a):max(a),1);
    x = cat(1,x,NaN);
    y = trajinfo(min(a):max(a),2);
    y = cat(1,y,NaN);
    t = trajinfo(min(a):max(a),3);
    t = cat(1,t,NaN);
    patch(x,y,t,...
        'LineStyle','none',...
        'Marker','o',...
        'MarkerSize',7,...
        'MarkerFaceColor','none',...
        'MarkerEdgeColor','flat');
    end
end
hold off
set(gca, 'color','none')
end

end
```

A.1.2 Mean squared displacement for trajectories of non-uniform length

```
%Calculate MSD for all trajectories from tracked.

% Functions:
%   overlapping_MSD.m
%
%
%


% Important outputs:
% ids made while making MSD matrix that corellates traj and msd
% trackedlarge/small are the trajectories BEFORE applying a min length
% largetraj/smalltraj is the traj information separated as gran and scrum
% traj is the x/y/t/scrumID/ID information
% T and Tfull tables has inforamtion like alpha and Diff coeff.
% msd is the MSD for each individual trajectory


%==============================
% Give Initial Information about EXPT
%==============================
clearvars;

exptno = 'HY1071';
plane = 'bottom';

load(['Working/' exptno '_' plane '_trajectories.mat'])

%==============================
```

```
% Calculate MSDs and ID matrix
%================================

%ids give the trajectory number, large or small, length
%msd matches the index of ids col 1 is the time displacement in frame #
%therefore col 1 in ids is NaN

[ids,msd] = fun_overlapping_MSD(traj);

save(['Working/' exptno '_' plane '_overlappingMSD.mat'],'ids','msd');

%%

%================================
% Organize everything into a table
%================================

idinput = ids;
inputtracked = traj;


minlength = 49;
fitlength = 10;
pixelsize = 71; %nm from microscope
sperframe = 0.1; %s per frame usually 0.1s (10 Hz)

%filter the trajectories for the required size
idxs = find(idinput(3,:) >= minlength);
ntraj = length(idxs);
nsmall = sum(idinput(2,idxs) == 1);
nlarge = sum(idinput(2,idxs) == 2);
```

```
61
62
63  %create variables to go into a table to export to R
64  ID = idinput(1,idxs)'; %done
65  sizetype = char(zeros(ntraj,1)); %edit in loop
66  D = zeros(ntraj,1);
67  alpha = zeros(ntraj,1);
68  tlength = idinput(3,idxs)'; %done
69  t = sperframe.*(1:fitlength);
70  logt = log10(t);
71  opt = optimset('Display','none','TolFun',10^-8,'TolX',10^-8);
72  lfit = @(x,t)x(1).*t+x(2);
73  %
74  wh = waitbar(0,'Starting...');
75  tic;
76  ud = 100;
77
78  for m=1:ntraj
79      %calc the other variables for the table first
80      if idinput(2,idxs(m)) == 1
81          sizetype(m) = 'S';
82      else
83          sizetype(m) = 'L';
84      end
85
86      % Net Displacement
87      looptraj = traj(traj(:,3)==idxs(m),[1 2]);
88      R_i = looptraj(1,:);
89      R_f = looptraj(end,:);
90      R_px = pdist([R_i;R_f],'euclidean'); % get the distance
91      R_net(m) = R_px.*(pixelsize/1000);
```

```
92
93      %now fit the msd
94      cmsd = msd(1:fitlength,idxs(m))';
95      logmsd = log10(cmsd);
96      result = lsqcurvefit(lfit,[1,1],logt,logmsd,[],[],opt);
97      alpha(m) = result(1);
98      D(m) = result(2); %in units of log10(pixel2/s)
99      if ud == m
100         ctime = toc;
101         tperitr = ctime/m;
102         tleft = round(tperitr*(ntraj-m));
103         hr = floor(tleft/3600);
104         mins = floor((tleft-hr*3600)/60);
105         sec = round(tleft-hr*3600-mins*60);
106         waitbar(m/ntraj,wh,{['Fitting Trajectory: ' num2str(m) ' of ' num2str(ntraj)];
    ↪  ...
107             ['Time Remaining: ' num2str(hr,'%02i') ':' num2str(mins,'%02i') ':'
    ↪  num2str(sec,'%02i')]});
108         ud = ud + 100;
109     end
110
111
112 end
113
114
115 %convert D to real units
116 D2 = 10.^D; %units of pixel^2/s
117 D2 = D2.*pixelsize^2*(1/1000)^2/4; %now um^2/s + divide by 4 for 2-D system
118
119 T = table(ID,sizetype,D2,alpha,tlength,R_net', ...
120     'VariableNames',{'ID','Size','D','Alpha','Length','NetDisp'});
```

```
121
122
123
124 save(['Working/' exptno '_' plane '_overlappingmsd.mat'], ...
125     'T','traj','msd','ids','fitlength','-append');
126
127 close(wh); clear ud ctime tperitr tleft hr mins sec wh
128
129
130
131 %% Ensemble avg
132
133 fitlength = 10; %number of points to fit for MSD,
134 minlength = 49; %min MSD to be included
135 maxlength = 2000; %max MSD to be included
136
137 pixelsize = 71; %nm from microscope
138 sperframe = .1; %s per frame usually 0.1s (10 Hz)
139 %xlimit = [0 10];
140
141
142
143 trajgran = ids(2,:) == 1;
144 trajscrum = ids(2,:) == 2;
145 trajlength = (ids(3,:) >= minlength) & (ids(3,:) <= maxlength); %select the proper
    ↪  length range
146
147 idxgran = find(trajgran & trajlength);
148 idxscrum = find(trajscrum & trajlength);
149
150
```

```
msdgran = msd(:,idxgran);
msdscrum = msd(:,idxscrum);

cpixel = pixelsize^2*(1/1000)^2; %pixel conversion to um^2

avgmsdgran = sum(msdgran,2) ./ sum(msdgran>0,2) .* cpixel;
avgmsdscrum = sum(msdscrum,2) ./ sum(msdscrum>0,2) .* cpixel;



t = 1:size(msd,1)/2;
t = sperframe.*t; %convert from frames to s

%fit the MSD
logt = log10(t(1:fitlength));
opt = optimset('Display','none','TolFun',10^-8,'TolX',10^-8);
lfit = @(x,t)x(1).*t+x(2);
logmsd = log10(avgmsdgran(1:fitlength));
[resultgran,~,res,~,~,~,J] = lsqcurvefit(lfit,[1,1],logt,logmsd',[],[],opt);
ci = nlparci(resultgran,res,'jacobian',J);
plusminusgran(1,:) = ci(1,:) - resultgran(1);
plusminusgran(2,:) = ci(2,:) - resultgran(2);

result = resultgran;
temp(1) = result(1);
temp(2) = ci(1,1);
temp(3) = ci(1,2);
temp(4) = result(2);
temp(5) = ci(2,1);
temp(6) = ci(2,2);
grancol = temp; clear temp

```

```
logmsd = log10(avgmsdscrum(1:fitlength));
[resultscrum,~,res,~,~,~,J] = lsqcurvefit(lfit,[1,1],logt,logmsd',[],[],opt);
ci = nlparci(resultscrum,res,'jacobian',J);
plusminusscrum(1,:) = ci(1,:) - resultscrum(1);
plusminusscrum(2,:) = ci(2,:) - resultscrum(2);

result = resultscrum;
temp(1) = result(1);
temp(2) = ci(1,1);
temp(3) = ci(1,2);
temp(4) = result(2);
temp(5) = ci(2,1);
temp(6) = ci(2,2);
scrumcol = temp; clear temp

fitgran = 10^resultgran(2).*t.^resultgran(1);
fitscrum = 10^resultscrum(2).*t.^resultscrum(1);

save(['Working/' exptno '_' plane '_ensemblemsd.mat'], ...
 ↪  'avgmsdgran','avgmsdscrum','plusminusgran','plusminusscrum','fitgran','fitscrum','resultgran','resu



figure
clf
subplot(2,1,1)
plot(t,avgmsdgran(1:length(t)),'o',t,fitgran,'-')
title(['Granules: ' num2str(minlength) '-' num2str(maxlength) ...
```

```
    ' \alpha = ' num2str(resultgran(1),'%1.2f') ' +/- ' num2str(plusminusgran(1,2),'%1.2f')])
%xlim(xlimit)
xlabel('delta (s)')
ylabel('MSD (um^2)')
set(gca,'FontSize',16,'XScale','log','YScale','log')
subplot(2,1,2)
plot(t,avgmsdscrum(1:length(t)),'o',t,fitscrum,'-')
title(['Scrum: ' num2str(minlength) '-' num2str(maxlength)...
    ' \alpha = ' num2str(resultscrum(1),'%1.2f') ' +/- ' num2str(plusminusscrum(1,2),'%1.2f')])
%xlim(xlimit)
xlabel('delta (s)')
ylabel('MSD (um^2)')
set(gca,'FontSize',16,'XScale','log','YScale','log')
```

A.2 Scrum Flux Determination

```
LOOPRADIUS = 15;

clearvars -except LOOPRADIUS;

% namestr = 'HY1071_bottom';
namestr = 'cell1_prestim_middle2';

g_validitylength = 8; %how many frames must the granule last to be included in the analysis
s_validitylength = 500; %how many frames must the scrum last to be included in the analysis
```

```
radius = LOOPRADIUS; %how many pixels must the granule be in to be considered
 ↪  interacting

load(['Working/' namestr '_trajectories.mat']);

%analyze granules
granules = traj(traj(:,5) == 1,1:4);
ct = 1; newgrans = []; granids = [];

for n = 1:max(granules(:,4))

    temp = granules(granules(:,4)==n,:);

    if length(temp) > g_validitylength

        granids = [granids; n];
        newgrans = [newgrans; temp];

    end

end

gran.ids = granids; gran.traj = newgrans;


%analyze scrums
scrums = traj(traj(:,5) == 2,1:4);
ct = 1; newscrums = []; scrumids = [];

for n = 1:max(scrums(:,4))

```

```
    temp = scrums(scrums(:,4)==n,:);

    if length(temp) > s_validitylength

        scrumids = [scrumids; n];
        newscrums = [newscrums; temp];

    end

end

scrum.ids = scrumids; scrum.traj = newscrums;


 save(['Working/' namestr 'trajecories_scrumfilter' num2str(s_validitylength) '.mat'],
 ↪  's_validitylength', 'gran', 'scrum')


% namestr = 'HY1071_bottom'; s_validitylength = 50;
clearvars -except s_validitylength namestr

load(['Working/' namestr 'trajecories_scrumfilter' num2str(s_validitylength) '.mat'])
ct1 =1;


for LOOPRADIUS = [12 13 14 15 16 17 18 19 20]
potinter = [];

% for each time frame

for frame = 1:max(scrum.traj(:,3))
```

```
70
71          %find the scrum positions of interest
72          scruminframe = scrum.traj(scrum.traj(:,3) == frame,:);
73          graninframe = gran.traj(gran.traj(:,3) == frame,:);
74
75          % itentify potential granules of interaction
76          for n = 1: size(scruminframe,1)
77              log_x = scruminframe(n,1) - LOOPRADIUS-5  <= graninframe(:,1) &
    ↪  graninframe(:,1) <= scruminframe(n,1) + LOOPRADIUS+5;
78              log_y = scruminframe(n,2) - LOOPRADIUS-5  <= graninframe(:,2) &
    ↪  graninframe(:,2) <= scruminframe(n,2) + LOOPRADIUS+5;
79              log_xy = log_x & log_y;
80
81              if sum(log_xy) > 0 %convert good granules to r distance
82                  scrumpos = scruminframe(n,[1 2]);
83                  potgrans = graninframe(log_xy,:);
84                  r = sqrt((scrumpos(1) - potgrans(:,1)).^2 + (scrumpos(2) -
    ↪  potgrans(:,2)).^2);
85                  IDg = potgrans(:,4);
86                  IDs = ones(size(IDg)).*scruminframe(n,4);
87                  t = ones(size(IDg)).*frame;
88
89                  potinter = [potinter; IDg IDs r t];
90              end
91          end
92
93
94  end
95  %
96
97  potinter2 = potinter(potinter(:,3) > LOOPRADIUS-1 & potinter(:,3) < LOOPRADIUS+1,:);
```

```
98
99  % look at every granule trajectory
100
101 granids = unique(potinter2(:,1));
102 interaction = [];
103
104 for n = 1:length(granids)
105     subtraj = potinter2(potinter2(:,1)==granids(n),:);
106     tavg = mean(subtraj(:,4));
107     rdir = subtraj(end,3) - subtraj(1,3);
108     log_in = rdir < 0; %in is 1 | out is 0
109
110     % if there is only one point in analysis annulus, use the neighboring
111     % timesteps to identify direction of flux
112     if rdir == 0
113         bwd = gran.traj(:,4) == granids(n) & gran.traj(:,3) == tavg-1;
114         ctr = gran.traj(:,4) == granids(n) & gran.traj(:,3) == tavg;
115         fwd = gran.traj(:,4) == granids(n) & gran.traj(:,3) == tavg+1;
116         comb = bwd+ctr+fwd;
117         granpos = gran.traj(find(comb),[1 2]);
118         scrumpos = scrum.traj(scrum.traj(:,4) == subtraj(:,2) & scrum.traj(:,3) ==
    ↪  tavg,[1 2]);
119
120         r = sqrt((scrumpos(1) - granpos(:,1)).^2 + (scrumpos(2) - granpos(:,2)).^2);
121         rdir = r(end) - r(1);
122         log_in = rdir < 0; %in is 1 | out is 0
123     end
124
125
126     IDg = subtraj(1,1);
127     IDs = subtraj(1,2);
```

```
128
129     interaction = [interaction; IDg IDs tavg log_in];
130
131 end
132
133 %
134
135 inevents = interaction(interaction(:,4)==1,:);
136
137 nscrums = unique(inevents(:,2));
138 in_waittime = [];
139 in_trajlen = [];
140
141 for n = 1:length(nscrums)
142    subevents = inevents(inevents(:,2)==nscrums(n),:);
143    if size(subevents,1)>1
144
145    subevents = sortrows(subevents,3);
146    subtimes = diff(subevents(:,3));
147    in_waittime = [in_waittime; subtimes];
148 %
149 %    for nn = 1:size(subevents,1)
150 %      tlen = sum(gran.traj(:,4)==subevents(nn,1));
151 %      in_trajlen = [in_trajlen; tlen];
152 %    end
153    end
154 end
155
156 outevents = interaction(interaction(:,4)==0,:);
157
158 nscrums = unique(outevents(:,2));
```

```
out_waittime = [];

for n = 1:length(nscrums)
   subevents = outevents(outevents(:,2)==nscrums(n),:);
   if size(subevents,1)>1

   subevents = sortrows(subevents,3);
   subtimes = diff(subevents(:,3));
   out_waittime = [out_waittime; subtimes];
   end
end

nscrums = unique(inevents(:,2));

inout_waittime = [];

for n = 1:length(nscrums)
 id_pairs = [];
    in_subevents = inevents(inevents(:,2)==nscrums(n),:);
    out_subevents = outevents(outevents(:,2)==nscrums(n),:);

    if size(in_subevents,1) > 0 & size(out_subevents,1) > 0

        for m  = 1:size(in_subevents,1) %find all the pairs for enter-exit
            in = in_subevents(m,3);
           pot_inout = out_subevents(:,3) - in;
           good_inout = pot_inout(pot_inout>0); good_inout = min(good_inout);



           if ~isempty(good_inout)
```

```
%             inout_waittime(ct) = good_inout; ct = ct+1;
             in_id = m; out_id = find(pot_inout == good_inout);
            id_pairs = [id_pairs; in_id out_id(1)];
            end

        end

        % if multiple enters coresspond to an exit, use closest pair only
        new_idpairs = [];
        if ~isempty(id_pairs)
        if length(id_pairs(:,2)) > length(unique(id_pairs(:,2)))
            s_ids = unique(id_pairs(:,2));
            for k = 1:length(s_ids)
               if sum(id_pairs(:,2)==s_ids(k)) > 1
                  g_ids = id_pairs(id_pairs(:,2) ==s_ids(k),1);

                  g_id = max(g_ids); s_id = s_ids(k);
                  id_pair = [g_id s_id];
               else
                   id_pair = id_pairs(id_pairs(:,2)==s_ids(k),:);
               end

               new_idpairs = [new_idpairs; id_pair];
            end
        else
            new_idpairs = id_pairs;
        end

        waittimes = out_subevents(new_idpairs(:,2),3) -
↪  in_subevents(new_idpairs(:,1),3);
        inout_waittime = [inout_waittime;waittimes];
```

```
220         end
221     end
222 end
223
224
225 %
226
227 spf = 0.1;
228 exittime = histogram2pts(out_waittime.*spf,'Normalization','pdf','BinMethod','auto');
229 entertime = histogram2pts(in_waittime.*spf,'Normalization','pdf','BinMethod','auto');
230 enextime = histogram2pts(inout_waittime.*spf,'Normalization','pdf','BinMethod','auto');
231 t1 = 0:max(max(entertime(:,1)),max(exittime(:,1)));
232
233 entercdf =
    ↪ histogram2pts(in_waittime.*spf,'FaceColor',parula(1),'Normalization','cdf','BinMethod','auto');
234 exitcdf =
    ↪ histogram2pts(out_waittime.*spf,'FaceColor','r','Normalization','cdf','BinMethod','auto');
235 enter2exitcdf =
    ↪ histogram2pts(inout_waittime.*spf,'FaceColor','k','Normalization','cdf','BinMethod','auto');
236
237 % disp(length(out_waittime))
238
239 % efit2 = @(x,t)x(1).*exp(-x(2).*t)+x(3).*exp(-x(4).*t);
240 % opt = optimset('Display','none','TolFun',10^-8,'TolX',10^-8);
241 % [r,~,res,~,~,~,J] =
    ↪ lsqcurvefit(efit2,[0.5,0.2,0.5,0.02],entercdf(:,1),1-entercdf(:,2),[],[],opt);
242 % resultcdf2(1,1:4) = r;
243 % ci = nlparci(r,res,'jacobian',J);
244 % resultcdf2(1,5) = ci(2,2) - r(2);
245 % resultcdf2(1,6) = ci(4,2) - r(4);
246 %
```

```
% [r,~,res,~,~,~,J] =
 ↪  lsqcurvefit(efit2,[0.5,0.2,0.5,0.02],exitcdf(:,1),1-exitcdf(:,2),[],[],opt);
% resultcdf2(2,1:4) = r;
% ci = nlparci(r,res,'jacobian',J);
% resultcdf2(2,5) = ci(2,2) - r(2);
% resultcdf2(2,6) = ci(4,2) - r(4);
%
% [r,~,res,~,~,~,J] =
 ↪  lsqcurvefit(efit2,[0.5,0.2,0.5,0.02],enter2exitcdf(:,1),1-enter2exitcdf(:,2),[],[],opt);
% resultcdf2(3,1:4) = r;
% ci = nlparci(r,res,'jacobian',J);
% resultcdf2(3,5) = ci(2,2) - r(2);
% resultcdf2(3,6) = ci(4,2) - r(4);
%
% efit = @(x,t)x(1).*exp(-x(2).*t);
% opt = optimset('Display','none','TolFun',10^-8,'TolX',10^-8);
% [r,~,res,~,~,~,J] =
 ↪  lsqcurvefit(efit,[0.5,0.2],entertime(:,1),entertime(:,2),[],[],opt);
% resultpdf2(1,1:2) = r;
% ci = nlparci(r,res,'jacobian',J);
% resultpdf2(1,3) = ci(2,2) - r(2);
%
% [r,~,res,~,~,~,J] = lsqcurvefit(efit,[0.5,0.2],exittime(:,1),exittime(:,2),[],[],opt);
% resultpdf2(2,1:2) = r;
% ci = nlparci(r,res,'jacobian',J);
% resultpdf2(2,3) = ci(2,2) - r(2);
%
% [r,~,res,~,~,~,J] = lsqcurvefit(efit,[0.5,0.2],enextime(:,1),enextime(:,2),[],[],opt);
% resultpdf2(3,1:2) = r;
% ci = nlparci(r,res,'jacobian',J);
% resultpdf2(3,3) = ci(2,2) - r(2);
```

```
275
276
277 % figure(7),
278 % subplot(3, 3, LOOPRADIUS-11)
279 % semilogy(entertime(:,1),entertime(:,2),'o',exittime(:,1),exittime(:,2),'or', ...
280 %     enextime(:,1),enextime(:,2),'ok', ...
281 %     t1,efit(resultpdf2(1,1:2),t1),'-b',t1,efit(resultpdf2(2,1:2),t1),'-r',...
282 %     t1,efit(resultpdf2(3,1:2),t1),'-k',...
283 %     'LineWidth',2.5,'MarkerSize',8);
284 % % lh = legend(['Enter: \tau_1 = ' num2str(1/resultcdf2(1,2),'%1.2f') ' s, \tau_2 = '
    ↪ num2str(1/resultcdf2(1,4),'%1.2f') ' s, A_1/A_2 = '
    ↪ num2str(resultcdf2(1,1)/resultcdf2(1,3),'%1.3f')], ...
285 % %     ['Exit: \tau_1 = ' num2str(1/resultcdf2(2,2),'%1.2f') ' s, \tau_2 = '
    ↪ num2str(1/resultcdf2(2,4),'%1.2f') ' s, A_1/A_2 = '
    ↪ num2str(resultcdf2(2,1)/resultcdf2(2,3),'%1.3f')], ...
286 % %     ['Enter -> Exit: \tau_1 = ' num2str(1/resultcdf2(3,2),'%1.2f') ' s, \tau_2 = '
    ↪ num2str(1/resultcdf2(3,4),'%1.2f') ' s, A_1/A_2 = '
    ↪ num2str(resultcdf2(3,1)/resultcdf2(3,3),'%1.3f')]);
287 %     lh.Color = 'none';
288 % xlabel('time until next event (s)')
289 % ylabel('pdf')
290 % title(['time until next event: radius ' num2str(LOOPRADIUS)])
291 % ylim([10^-5 10^0])
292 % xlim([0 100])
293 % set(gca,'FontSize',16);
294
295
296 % figure(8),
297 % subplot(3, 3, LOOPRADIUS-11)
298 % semilogy(entercdf(:,1),1-entercdf(:,2),'o',exitcdf(:,1),1-exitcdf(:,2),'or', ...
299 %     enter2exitcdf(:,1),1-enter2exitcdf(:,2),'ok', ...
```

```
%     t1,efit2(resultcdf2(1,1:4),t1),'-b',t1,efit2(resultcdf2(2,1:4),t1),'-r',...
%     t1,efit2(resultcdf2(3,1:4),t1),'-k',...
%     'LineWidth',2.5,'MarkerSize',8);
% lh = legend(['Enter: \tau_1 = ' num2str(1/resultcdf2(1,2),'%1.2f') ' s, \tau_2 = '
 ↪  num2str(1/resultcdf2(1,4),'%1.2f') ' s, A_1/A_2 = '
 ↪  num2str(resultcdf2(1,1)/resultcdf2(1,3),'%1.3f')], ...
%     ['Exit: \tau_1 = ' num2str(1/resultcdf2(2,2),'%1.2f') ' s, \tau_2 = '
 ↪  num2str(1/resultcdf2(2,4),'%1.2f') ' s, A_1/A_2 = '
 ↪  num2str(resultcdf2(2,1)/resultcdf2(2,3),'%1.3f')], ...
%     ['Enter -> Exit: \tau_1 = ' num2str(1/resultcdf2(3,2),'%1.2f') ' s, \tau_2 = '
 ↪  num2str(1/resultcdf2(3,4),'%1.2f') ' s, A_1/A_2 = '
 ↪  num2str(resultcdf2(3,1)/resultcdf2(3,3),'%1.3f')]);
%     lh.Color = 'none';
% xlabel('time until next event (s)')
% ylabel('1-cdf')
% title(['time until next event: radius ' num2str(LOOPRADIUS)])
% ylim([10^-2.7 10^0])
% xlim([0 100])
% set(gca,'FontSize',16);

% calcuate the trajecotry length bias

for n = 1:length(scrum.ids)
   trajlens(n) = sum(scrum.traj(:,4)==scrum.ids(n));
end

%
% cdf_fits{ct1} = resultcdf2;
% cdf{ct1}.enter = entercdf;
% cdf{ct1}.exit = exitcdf;
% cdf{ct1}.enex = enter2exitcdf;
```

```
%
%
% pdf_fits{ct1} = resultpdf2;
% pdf{ct1}.enter = entertime;
% pdf{ct1}.exit = exittime;
% pdf{ct1}.enex = enextime;


events{ct1}.enter = in_waittime;
events{ct1}.exit = out_waittime;
events{ct1}.enex = inout_waittime;
events{ct1}.trajlen = trajlens;
interactions{ct1} = interaction;

ct1 = ct1+1;

%  export_fig(['ctrldata_filter' num2str(validitylength) '_radius' num2str(LOOPRADIUS)
 ↪  '_annulusmethod.png'],'-r500','-transparent')
end


% uncomment this one
 save(['Working/' namestr '_waittimes.mat'],'events','s_validitylength','interactions')
```